THEORETICAL INVESTIGATION OF PHOTONIC CRYSTAL AND METAL CLADDING FOR WAVEGUIDES AND LASERS

A Thesis
Presented to
The Academic Faculty

by

Vivek Krishnamurthy

In Partial Fulfillment
of the Requirements for the Degree
Doctor of Philosophy in the
School of Electrical and Computer Engineering

Georgia Institute of Technology
May 2009

THEORETICAL INVESTIGATION OF PHOTONIC CRYSTAL AND METAL CLADDING FOR WAVEGUIDES AND LASERS

Approved by:

Professor Benjamin Klein, Advisor, Committee Chair
School of Electrical and Computer Engineering
Georgia Institute of Technology

Professor Kambi Alavi, Associate Chairman
Department of Electrical Engineering
University of Texas at Arlington

Professor Douglas Yoder
School of Electrical and Computer Engineering
Georgia Institute of Technology

Professor Janet K. Allen
G. W. Woodruff School of Mechanical Engineering
Georgia Institute of Technology

Professor John Buck
School of Electrical and Computer Engineering
Georgia Institute of Technology

Professor Thomas Gaylord
School of Electrical and Computer Engineering
Georgia Institute of Technology

Date Approved: 6 January 2009

To my Teachers

ACKNOWLEDGEMENTS

I thought, I like school because of my aptitude for solving problems. Graduate studies proved me that it is only half-true. The people around me are subtly compelementing my liking for academics. The aptitude for problems comes because I have been guided towards the satisfaction of solving challenging and growing problems. I now believe that my lateral and longitudinal growth of aptitude is directly proportional to the guidance I received from my teachers. If we assume that guidance cannot be accidental, then certainly it springs from the patience of my teachers. So this thesis work is dedicated to my teachers and their patience.

This formal letter of acknowledgement is not enough to thank the informal love and support of my parents, for teaching me from holding my first pencil to writing the first letter, for giving a memorable childhood that cannot be any better, for defining my inherent personality. Those lessons from home would always be the beacon of my life.

My middle-school and high-school math teachers, especially Mr. Lakshmeesh, Ms. Seethalakshmi complemented the efforts of science teachers, Mr. Dasharathi and Mr. Vishwanathaiah to ensure my path towards Engineering Sciences. The undergraduate project work under the guidance of Mr. Nataraj, for the first time gave me the satisfaction of independent problem solving and it also instigated towards graduate studies.

All the projects and homeworks given by Professors though graduate courses, I think pushed me towards research, especially Dr. Michael Vasilyev for guiding me through the exciting surface plasmon project. I am grateful to my Masters thesis advisor, Dr. Kambiz Alavi for walking to library to get books for me. Those books, I

think strengthened my interest in Optical electronics and defined my research interests. It is his mentoring and encouragement that really made me to enroll for PhD program.

I was fortunate to have a perfectionist like Dr. Alexey Maslov as a constructive critique of my entire PhD thesis work. Those precious hours that he spent in understanding my work and his suggestions for refinement were invaluable for showing the uniqueness of this work. Thanks to Dr. Janet K. Allen and System Realization group for rigorous review of my entire thesis. The thesis looks lot better than I imagined. Thanks to Matthias Messer and Chenjie Wang from System Realization group for showing the importance of robust design concepts. I am grateful to friend and collegue, Sriraaman for spending his time in reviewing my proposal defense and doctoral defense exam slides, to Dr. Fransesco Fedele's for treating me when I was suffering from various mathematical problems and especially when I had matrix inversion problem and to Dr. Yoder for being supportive to our group and providing guidance whenever I needed. I absolutely enjoyed various discussions on both theoretical and practical aspects of electroabsorption modulators and photodetectors with Dr. Yoder.

Above all, the support of the most important person responsible for this research work is Dr. Benjamin Klein. An excellent advisor, mentor, teacher, researcher, friend and above all a great human being. He will always be my role model and I will always strive to become as cool, as logical, as approachable and as unbiased as him throughout my life. I owe a huge debt of gratitude to Dr. Klein for his guidance, his belief in me, for giving sufficient freedom in exploring the research topic and for subtly re-proving that life at school is the best.

The research work was well complemented by our non-research activities in the form of colloquium and IEEE activities. It wouldnot have been possible without the support of Mrs. Julie Klein and my fellow graduate students for volunteering

in starting the colloquium and IEEE group, especially Matthias, Aditya, Anusha, Mashhour and Kemal.

My sincere acknowledgements to all funding sources, Georgia Tech. for supporting me as a GRA and GTA, to Canon Inc., to National Institute of Standards and Technology (NIST), Boulder and to System realization laboratory (SRL) from G. W. W. School of Mechanical Engineering.

Last but not the least, special thanks to my dear friends Aditya, Fahad, Jitin and Deepak for addicting me to all good and bad habits. Never missed food and fun!

TABLE OF CONTENTS

LIST OF TABLES

LIST OF FIGURES

SUMMARY

An efficient numerical analysis method for wavelength-scale and sub-wavelength-scale photonic structures is developed. It is applied to metal-clad nano-lasers and photonic crystal-based DBRs to calculate intrinsic losses (from open boundaries), and to photonic crystal-based waveguides to calculate intrinsic and extrinsic losses (due to fabrication errors).

Our results show that a metal-clad surface plasmon-based laser in a cylindrical configuration requires more gain to lase than is available from a semiconductor gain region. However, the lowest order TE and HE guided modes exhibit less loss than the other modes, and hold the most promise for lasing. For photonic crystal-based structures, our matrix-free implementation of the planewave expansion method for calculating layer modes combined with mode-matching between layers using a few lower order modes is shown to be a computationally efficient and reliable method. This method is then used to introduce robust design concepts for designing photonic crystal-based structures in the presence of fabrication uncertainties. Accounting for fabrication uncertainties is shown to be particularly important in the regions of the device where the light exhibits very low group velocity ('slow light'). Finally, the modal discrimination properties of photonic crystal-based DBRs (Distributed Bragg Reflectors) are compared with the properties of conventional oxide-DBR combinations to analyze the contribution of out-of-plane diffraction losses to modal discrimination.

CHAPTER I

INTRODUCTION

The ability to tailor the dispersion, confinement and extraction properties of light has sparked intense interest in periodic media (photonic crystals) within the photonics community. Photonic crystals have drawn the attention of scores of researchers from the perspective of inherent physics as well as applications. The periodicity of the medium modulates the optical wavefunction, resulting in the constructive or destructive interference of wavefunctions of various frequencies. As a consequence, only light in certain wavelengths ranges can propagate through the medium, while other wavelength ranges can't penetrate the medium due to destructive interference. The range of wavelengths that can't penetrate the periodic medium is known as the band gap [147, 58, 148, 48, 149] of the medium. Intentional defects can be created in photonic crystals by breaking the periodicity. These defects are used to generate localized electromagnetic states in the wavelength range of the bandgap of a defect-free bulk crystal. These localized states may have a small effective group velocity, which is referred to as slow light. The slow light obtained [43, 53] by using defects in a periodic medium provides a possible platform for all-optical processing of signals. Also, the structural properties of the periodic medium can be adjusted to observe negative refraction, even though the material does not possess a negative effective refractive index [86].

Some applications of bulk photonic crystals include distributed feedback (DFB) lasers, superlenses [68], superprisms [85], photonic crystal waveguides [140], couplers [63], splitters [9], high-Q small volume microcavities [101, 133], photonic crystal-based surface emitting lasers [150], and photonic crystal fibers [16], amongst others.

Another type of medium which is of immense interest to photonics researchers is the metallic medium [120]. Metal surfaces are known to guide light in surface plasmon modes, and therefore have the potential to provide a basis for sub-wavelength-scale nanophotonic devices. With the advancement of novel fabrication techniques, various nanophotonic applications based on thin metallic films have been explored. Though metallic surfaces give rise to surface plasmons, they also exhibit significant optical absorption and loss. For this reason, it has not been possible to successfully lase a device using surface plasmon modes coupled to a semiconductor gain medium at infra-red (IR) and visible wavelengths.

In this thesis, photonic crystal-clad waveguides and cavities and metal-clad cylindrical waveguides and cavities have been theoretically investigated using mode-matching methods.

The organization of the dissertation is as follows: the next two sections of this chapter provide motivation for the thesis work and a brief review of past work. In the next chapter, metal cladding for cylindrical nano-lasers is investigated using traditional cylindrical waveguide theory. The theory behind the out-of-plane mode-matching using vectorial planewave expansion-based scattering matrix analysis is presented in chapter 3. The theory developed in Chapter 3 is used to calculate the effect of extrinsic losses due to fabrication errors in photonic crystal couplers in chapter 4, and to calculate the modal discrimination in photonic crystal-based distributed Bragg reflectors (DBRs) in chapter 5. Finally in chapter 6, the summary and possible future directions of the research are presented.

Throughout this thesis, the z-direction is known as the out-of-plane direction, and the (x,y) or (ρ,ϕ) directions are referred to as in-plane directions.

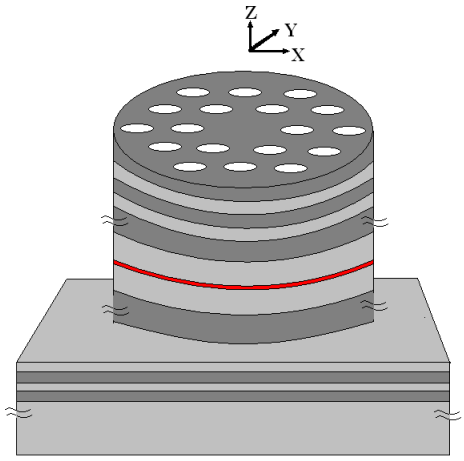

Figure 1: Photonic crystal defect-based VCSEL.

1.1 Motivation and brief review

1.1.1 Metal cladding for waveguides and lasers

For nanophotonic applications, thin metals are used to confine light in sub-wavelength-scale domains in the form of surface plasmons [138, 124, 144]. Several investigations of planar surface plasmon-based lasers exist [144, 10, 124]. Cylindrical structures such as nanowire [60] and micropost [112] -based lasers have been shown to possess good lasing properties in the absence of metals, but there has been little experimental or theoretical investigation of nanowires or microposts clad with metal for use as surface plasmon-based lasers. One exception is ref.[91], where the nanowire laser is treated as having infinite thickness metal cladding, but no investigation of finite thickness metal cladding is performed. In this thesis, the impact of metal cladding on the loss and lasing properties of micropost and nanowire lasers is isolated by neglecting the presence of mirrors in the out-of-plane direction. Three-layer in-plane mode-matching through classical cylindrical waveguide theory is then used to study the loss properties of cylindrical laser structures with finite thickness metal cladding.

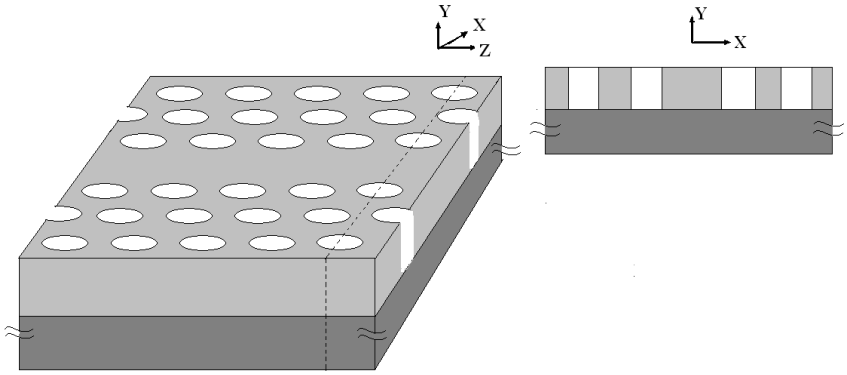

Figure 2: A line defect in a photonic crystal slab.

1.1.2 Photonic crystal cladding for waveguides and lasers

Consider the wavelength-scale optical devices shown in Figs. 1 and 2. The optical power propagation occurs primarily along the z-direction in both devices. However, the device depicted in Fig. 1 is a layered device along the z-direction, while the device depicted in Fig. 2 has a continuously varying (periodically modulated) refractive index along the z-direction. One way to find the electromagnetic field distribution throughout these structures is by meshing the entire device using a 3D grid and then solving Maxwell's equations in real space using finite-difference or finite-element methods. Though real-space approaches are robust and straightforward, the problem size can be impractically large for complex structures. One alternative approach is to solve the problem using a reciprocal domain technique combined with mode-matching. First, the structure is split into many 2D slices, each of which is uniform along the z-direction. For the device in Fig. 1, each layer forms a 2D slice, and for the device in Fig. 2, the structure is approximated by slicing it into thin 2D slices. Then, using planewaves as a basis set, the modes of each 2D slice are calculated in reciprocal space. Finally, these modes are matched across interfaces between slices via scattering matrix analysis [143, 79, 109, 137] to calculate field propagation throughout the device.

Theoretically [60], planewaves with the periodicity of the lattice form a natural

basis for the calculation of modes in photonic crystals because they satisfy the Bloch condition. With planewave expansion in the directions of periodicity, Helmholtz's equation can be reduced to an eigenvalue problem in reciprocal space with either the frequency squared ($(\frac{\omega}{c})^2$) [60, 128, 44] or the z-component of the wavevector squared (k_z^2) [47, 77, 29] as the eigenvalue. For the problems we consider, the frequency and the angle of incidence in one layer are known, and the problem is to find all of the resultant propagating and evanescent fields in all layers. For this reason, k_z^2 is used as the eigenvalue in this thesis. There are various methods to calculate the coupling between Bloch layer modes, including coupled mode theory [40], the Fourier modal approach [40, 77], the admittance method [29], the method of lines [47], eigenmode expansion [14], finite elements [99], finite differences [151], and the multi-pole approach [142]. All of these methods are well known and have been well documented in the literature.

In [79, 14, 109], the reciprocal domain mode-matching approach has been shown to be computationally efficient. By using vectorial layer modes (guided, leaky and perfectly matched layer (PML) modes) as basis sets [79, 109, 14], scattering matrix analysis along the z-direction was carried out to calculate the amplitudes of the layer modes in each layer. The mode amplitudes, along with the layer modes themselves, are then used to find the total field distribution throughout the device. However, in [14], the layer modes were found using analytical formulations. No analytical formulations exist for the layer modes of the devices shown in Figs. 1 and 2. Therefore, a numerical method has to be adopted to calculate the basis modes in each layer. Again, finite differences or finite elements can be used to solve for vectorial modes in each 2D layer. However, these methods are still cumbersome because of the requirements of problem-dependent gridding, slow speed, and large memory usage. Another solution is to use numerical planewave expansion with an explicit Helmholtz matrix to find layer modes, as in ref. [79] and ref. [109]. In this approach the spatial Fourier

transform of the permittivity has to be analytically derived to build the convolution operator for the explicit Helmholtz equation matrix. This method is suitable for dielectric structures for which the analytical Fourier transform can be calculated. The Helmholtz equation matrix obtained is not sparse and has a size of $2N \times 2N$, where N is the number of grids. If 128×128 grids are used for the structure in Fig. 1, this technique would require more than $16,000$ planewaves. Therefore, if the method in [79] or [109] is followed, the Helmholtz matrix would be a non-sparse matrix of size 32000×32000, which is highly impractical and inefficient to solve. Ultimately, the planewave expansion approach is efficient for large structures only if:

1. It can be generalized and made applicable to arbitrary structures.
2. It can be made faster than real space approaches.
3. It can be made memory efficient.
4. It does not rely on analytical calculations (it can be completely automated).

In this work, a planewave expansion technique is used along with a numerical Fourier operator to increase generality, automation, and speed compared to previous formulations. This leads to a matrix-free Helmholtz equation, which also increases memory efficiency [74, 73]. Planewave expansion using a numerical Fourier operator offers various advantages, such as:

1. Simple grids: uniform grids are used. There is no need for complex gridding.
2. Memory efficiency: it is shown in the next chapter that the problem is matrix free. For a problem with N grids, the storage requirement of the Helmholtz equation is only $2N$.
3. Speed: there is no time-consuming computation for building an explicit Helmholtz equation matrix. The numerical Fourier operator used in the Helmholtz equation requires only $\mathrm{O}(N \log N)$ computations for a problem with N grids.

Compared to previous work [79, 109, 14, 29], the planewave expansion method presented in this thesis offers a more efficient and faster way to calculate modes in arbitrary wavelength-scale devices using simple grids in the x-y plane to calculate all propagating and evanescent layer modes. Mode-matching analysis via scattering matrices is then carried out along the z-direction. Therefore, the z-direction will have very few grids for a wide range of problems of interest. The combination of planewave expansion for calculating all layer basis modes, along with out-of-plane mode-matching analysis to find the final electromagnetic distribution of fields throughout the device, is known as the Fourier modal approach [79, 109].

The Fourier modal approach is applicable to arbitrary dielectric media. This allows one to model fabrication uncertainties in the problem. A significant problem confronting the design of sub-micron scale photonic crystal-based devices is the extrinsic optical loss caused by fabrication errors. This problem is often neglected, despite experimental and theoretical evidence that fabrication errors [145, 49, 67, 35, 105] lead to uncontrolled scattering of light in photonic crystal structures. In this thesis, a robust design concept which provides criteria for selecting device design parameters to obtain the best combination of high device performance and low performance uncertainty in the presence of fabrication uncertainties is developed. Using slow light couplers as an example, the robust designs are compared with the optimum design (obtained without fabrication uncertainties) to show the impact of uncertainties in these structures. Some of the results can be generalized to arbitrary photonic crystal-based devices.

Finally, the Fourier modal approach is applied to another significant problem: the electromagnetic design of photonic crystal-based distributed Bragg reflectors (DBRs) used in high-power single-mode surface emitting lasers. Conventional vertical cavity surface emitting lasers (VCSELs) are known to be versatile sources for optical communications. Since their inception [130] and development [51], various theoretical

[66, 8, 23, 14] and experimental models of VCSELs [51, 41, 56, 21, 154] have been investigated. Although multi-mode oxide-confined VCSELs are known for strong lateral confinement of modes, high output power, and good current confinement properties, they also have the disadvantage of producing broader spectral output. To reduce the spectral width, single-mode operation is necessary. For obtaining single-mode operation, mode-selective optical losses are usually introduced in the VCSEL structure. Although these mode-selective losses increase the loss of higher-order modes, they also increase the loss of the fundamental mode, which is undesirable. Therefore, designing an efficient high-power single-mode VCSEL is a challenging task. Reducing the size of the oxide aperture for single-mode operation would increase the resistance of the device and result in early thermal rollover, limiting high-power operation. Increasing the aperture diameter allows higher output powers but also results in a decrease in modal discrimination. It is shown in [150, 38] that the use of a photonic crystal defect cavity for the lateral confinement of modes makes it possible to achieve high-power single-mode VCSEL operation. This problem is well-suited for the Fourier modal appraoch, which is used to investigate the modal discrimination properties of photonic crystal DBRs.

CHAPTER II

THEORETICAL INVESTIGATION OF METAL CLADDING FOR NANOWIRE LASERS AND CYLINDRICAL MICROPOST CAVITIES

In this chapter, an investigation of the transverse modal properties of cylindrical subwavelength metal-clad nanowire and micropost lasers via in-plane mode-matching analysis is carried. In this method, the effect of finite metal cladding thickness and gain in the core is considered. This chapter closely follows our published journal article[72].

2.1 Introduction

Recently there has been considerable interest in surface plasmon-based lasers [138, 124, 144] for nanophotonic applications. These devices attempt to achieve lasing with metal-dielectric surface plasmon modes, for which subwavelength-scale cavity confinement is possible. A surface plasmon-based laser has been successfully demonstrated at long wavelengths [138]. Also, there has been an investigation of lossless transmission of surface plasmon modes when a metal surface is adjacent to a gain medium [98]. The coupling of stimulated emission into short range and long range surface plasmon modes was also calculated in [144]. A proposal to exploit the stimulated emission in the active region to coherently strengthen the electric field of a surface plasmon mode has been made in [10, 124]. However, all the above investigations have been restricted to planar waveguides.

There has been an investigation of metallic cylindrical waveguides in the long wavelength range for low loss transmission of various modes in the core guided mode

regime [88, 95, 55]. Surface plasmon modes and their loss properties in cylindrical waveguides [3, 91] were also calculated, but the analysis was restricted to purely TM modes in [3], and the cladding layer was assumed to have an infinite width in [91]. There has also been interest in various nanoscale vertically emitting sources, such as nanowire lasers [60] and micropost-based cavities [112]. The objective of the present work is to quantitatively investigate the effect of metal cladding with finite thickness on the confinement, loss and coupling of modes in cylindrical nanowire and micropost lasers.

The chapter is organized as follows. First, a description of the laser waveguide structure, and the mode calculation technique is presented. This is followed by results for various core guided modes and dielectric-metal surface guided modes (surface plasmon modes). Finally, conclusions are drawn based on the results.

2.2 Structure

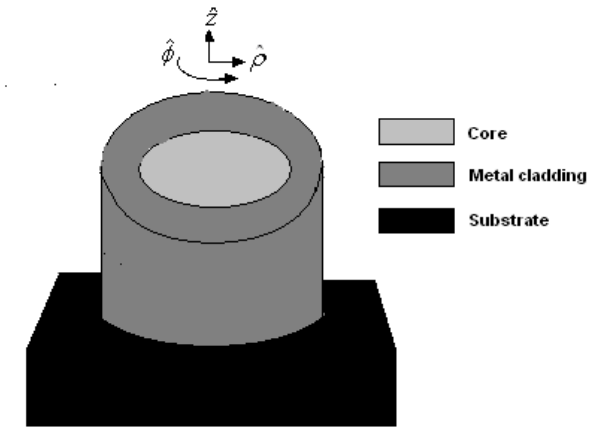

Figure 3: Metal-clad laser structure.

The structure under consideration is shown in Fig. 3. It is a cylindrical waveguide with metal cladding. The core semiconductor is considered to be $In_{0.2}Ga_{0.8}As$ [100, 65], with a refractive index of 3.6. The metal used in the calculation is gold, with a refractive index of $0.22 - j6.71$ [108]. The entire waveguide is surrounded by air.

The mirrors capping the laser cavity above and below are not considered for the purposes of this paper; the reflectivity of the endcaps can be made arbitrarily large using dielectric or metallic mirrors. Therefore, for our purposes the cylindrical laser waveguide is considered to be of infinite length. All calculations are done for a fixed wavelength of 1 μm.

The gain in the active semiconductor cavity will depend on the detailed internal structure of the nanowire and the method of pumping. The majority of experimentally realized nanowire and micropost lasers are optically pumped [124, 144, 60, 112] in the visible and UV range. In many nanowire structures, electrical pumping is not possible because of the absence of pn junction and controlled doping [114]. However, this difficulty can be overcome with advancements in materials science. For the purposes of this work, it is not necessary to restrict our analysis to a particular pumping method. In our simulations with gain included, we assume a reasonable value for the material gain of the $In_{0.2}Ga_{0.8}As$ active region, 1000 cm^{-1}.

2.3 Theory

The theory behind the infinite cylindrical waveguide is well known [3, 17]. By assuming a particular functional form with unknown coefficients for the coupled E_z and H_z field components in each region, all the other components of fields can be calculated.

In layer I,

$$E_z = A^I \frac{I_\nu(k_t^I \rho)}{I_\nu(k_t^I a)} \cos\nu\phi e^{-ik_z z} \tag{1}$$

$$H_z = B^I \frac{I_\nu(k_t^I \rho)}{I_\nu(k_t^I a)} \sin\nu\phi e^{-ik_z z} \tag{2}$$

In layer II,

$$E_z = (A_1^{II} \frac{I_\nu(k_t^{II} \rho)}{I_\nu(k_t^{II} a)} + A_2^{II} \frac{K_\nu(k_t^{II} \rho)}{K_\nu(k_t^{II} a)}) \cos\nu\phi e^{-ik_z z} \tag{3}$$

$$H_z = (B_1^{II} \frac{I_\nu(k_t^{II} \rho)}{I_\nu(k_t^{II} a)} + B_2^{II} \frac{K_\nu(k_t^{II} \rho)}{K_\nu(k_t^{II} a)}) \sin\nu\phi e^{-ik_z z} \tag{4}$$

In layer III,

$$E_z = A^{III} \frac{K_\nu(k_t^{III}\rho)}{K_\nu(k_t^{III}(a+t))} \cos\nu\phi e^{-ik_z z} \tag{5}$$

$$H_z = B^{III} \frac{K_\nu(k_t^{III}\rho)}{K_\nu(k_t^{III}(a+t))} \sin\nu\phi e^{-ik_z z} \tag{6}$$

In the above equations A^I, B^I, A_1^{II}, A_2^{II}, B_1^{II}, B_2^{II}, A^{III} and B^{III} are the unknown coefficients. $k_t = \sqrt{k_z^2 - k^2}$ is the transverse component of the wavevector, k_z is the out-of-plane component of the wavevector, k is the wavevector in a dielectric medium, k_0 is the wavevector in air, η is the intrinsic impedance of vaccum, a is the radius of the cylinder and t is the thickness of the metal cladding. $I_\nu()$ and $K_\nu()$ are the modified Bessel and modified Neumann functions, respectively. The modified Bessel and Neumann functions can be replaced by ordinary Bessel and Neumann functions by changing the in-plane wavevector definition to $\sqrt{k^2 - k_z^2}$. From the above formulations, fields E_ϕ and H_ϕ are calculated in each region using Maxwell's equations. The unknown coefficients are obtained by matching the tangential field components at the cylindrical boundaries between each region. This results in an 8×8 matrix as shown in (7). The dispersion equation is obtained by setting the determinant of the matrix in (7), equal to zero. In our implementation, Newton's method is used to solve the dispersion equation.

To examine the effects of metal cladding, the parameters of interest are:

1. The modal gain or attenuation constant, α which indicates the spatial rate of growth or spatial rate of decay of modes.

2. The confinement factor (gain overlap factor), Γ which indicates the amount of modal power in the gain region.

3. The coupling factor, ξ which indicates the amount of modal power present outside the waveguide region (modal spreadout).

$$
\begin{bmatrix}
1 & 0 & -1 \\
0 & 1 & 0 \\
-\frac{k_z}{k_t^{I^2}}\frac{\nu}{a} & -\frac{k_0\eta}{k_t^I}\left(\frac{\nu}{k_t^I a}+\frac{I_{\nu+1}(k_t^I a)}{I_\nu(k_t^I a)}\right) & \frac{k_z}{k_t^{II^2}}\frac{\nu}{a} \\
\frac{k^{I^2}}{k_0 k_t^I \eta}\left(\frac{\nu}{k_t^I a}+\frac{I_{\nu+1}(k_t^I a)}{I_\nu(k_t^I a)}\right) & \frac{k_z}{k_t^{I^2}}\frac{\nu}{a} & -\frac{k^{II^2}}{k_0 k_t^{II}\eta}\left(\frac{\nu}{k_t^{II}a}+\frac{I_{\nu+1}(k_t^{II}a)}{I_\nu(k_t^{II}a)}\right) \\
0 & 0 & \frac{I_\nu(k_t^{II}(a+t))}{I_\nu(k_t^{II}a)} \\
0 & 0 & 0 \\
0 & 0 & -\frac{k_z}{k_t^{I^2}}\frac{\nu}{(a+t)}\frac{I_\nu(k_t^{II}(a+t))}{I_\nu(k_t^{II}a)} \\
0 & 0 & \frac{k^{II^2}}{k_0 k_t^{II}\eta}\left(\frac{\nu}{k_t^{II}(a+t)}\frac{I_\nu(k_t^{II}(a+t))}{I_\nu(k_t^{II}(a))}+\frac{I_{\nu+1}(k_t^{II}(a+t))}{I_\nu(k_t^{II}(a))}\right)
\end{bmatrix}
$$

$$
\begin{bmatrix}
-1 & 0 \\
0 & -1 \\
\frac{k_z}{k_t^{II^2}}\frac{\nu}{a} & \frac{k_0\eta}{k_t^{II}}\left(\frac{\nu}{k_t^{II}a}+\frac{I_{\nu+1}(k_t^{II}a)}{I_\nu(k_t^{II}a)}\right) \\
-\frac{k^{II^2}}{k_0 k_t^{II}\eta}\left(\frac{\nu}{k_t^{II}a}-\frac{K_{\nu+1}(k_t^{II}a)}{K_\nu(k_t^{II}a)}\right) & -\frac{k_z}{k_t^{II^2}}\frac{\nu}{a} \\
\frac{K_\nu(k_t^{II}(a+t))}{K_\nu(k_t^{II}a)} & 0 \\
0 & \frac{I_\nu(k_t^{II}(a+t))}{I_\nu(k_t^{II}a)} \\
-\frac{k_z}{k_t^{II^2}}\frac{\nu}{(a+t)}\frac{K_\nu(k_t^{II}(a+t))}{K_\nu(k_t^{II}a)} & -\frac{k_0\eta}{k_t^{II}}\left(\frac{\nu}{k_t^{II}a}\frac{I_\nu(k_t^{II}(a+t))}{I_\nu(k_t^{II}a)}+\frac{I_{\nu+1}(k_t^{II}(a+t))}{I_\nu(k_t^{II}a)}\right) \\
\frac{k^{II^2}}{k_0 k_t^{II}\eta}\left(\frac{\nu}{k_t^{II}(a+t)}\frac{K_\nu(k_t^{II}(a+t))}{K_\nu(k_t^{II}(a))}-\frac{K_{\nu+1}(k_t^{II}(a+t))}{K_\nu(k_t^{II}(a))}\right) & \frac{k_z}{k_t^{II^2}}\frac{\nu}{(a+t)}\frac{I_\nu(k_t^{II}(a+t))}{I_\nu(k_t^{II}a)}
\end{bmatrix}
$$

$$
\begin{bmatrix}
0 & 0 \\
-1 & 0 \\
\frac{k_0\eta}{k_t^{II}}\left(\frac{\nu}{k_t^{II}a}-\frac{K_{\nu+1}(k_t^{II}a)}{K_\nu(k_t^{II}a)}\right) & 0 \\
-\frac{k_z}{k_t^{II^2}}\frac{\nu}{a} & 0 \\
0 & -1 \\
\frac{K_\nu(k_t^{II}(a+t))}{K_\nu(k_t^{II}a)} & 0 \\
-\frac{k_0\eta}{k_t^{II}}\left(\frac{\nu}{k_t^{II}a}\frac{I_\nu(k_t^{II}(a+t))}{I_\nu(k_t^{II}a)}+\frac{I_{\nu+1}(k_t^{II}(a+t))}{I_\nu(k_t^{II}a)}\right) & -\frac{k_0 k_z}{k_t^{III^2}}\frac{\nu}{(a+t)} \\
\frac{k_z}{k_t^{II^2}}\frac{\nu}{(a+t)}\frac{K_\nu(k_t^{II}(a+t))}{K_\nu(k_t^{II}a)} & -\frac{k^{III^2}}{k_0 k_t^{III}\eta}\left(\frac{\nu}{k_t^{III}(a+t)}-\frac{K_{\nu+1}(k_t^{III}(a+t))}{K_\nu(k_t^{III}(a+t))}\right)
\end{bmatrix}
$$

$$
\begin{bmatrix}
0 \\ 0 \\ 0 \\ 0 \\ 0 \\ -1 \\ -\frac{k_0\eta}{k_t^{III}}\left(\frac{\nu}{k_t^{III}(a+t)}-\frac{K_{\nu+1}(k_t^{III}(a+t))}{K_\nu(k_t^{III}(a+t))}\right) \\ -\frac{k_z}{k_0 k_t^{III^2}}\frac{\nu}{(a+t)}
\end{bmatrix}
\begin{bmatrix}
A^I \\ B^I \\ A_1^{II} \\ A_2^{II} \\ B_1^{II} \\ B_2^{II} \\ A^{III} \\ B^{III}
\end{bmatrix}
=
\begin{bmatrix}
0 \\ 0 \\ 0 \\ 0 \\ 0 \\ 0 \\ 0 \\ 0
\end{bmatrix}
\tag{7}
$$

In this work, modes are calculated for both passive and active core dielectrics. For the active core case, the core dielectric is given a material gain of 1000 cm^{-1}.

Assuming that the modal patterns do not change significantly with the inclusion of optical gain in the core dielectric, the confinement factor Γ is defined using the following relation.

$$\alpha_{with\ gain} = \Gamma\alpha_{bulk} + \alpha_{without\ gain} \tag{8}$$

Thus,

$$\Gamma = \frac{\alpha_{with\ gain} - \alpha_{without\ gain}}{\alpha_{bulk}} \tag{9}$$

where the out-of-plane component of the wavevector $k_z = \beta + j\alpha$, in which β is the phase constant and α is the the attenuation constant (negative for attenuation and positive for amplification). The gain overlap factor, Γ represents the ratio of the modal gain to bulk gain. $\alpha_{without\ gain}$ represents the attenuation constant of metal-clad passive cylindrical waveguide modes, which is equal to the loss of the active waveguide modes.

One potential advantage of metal-clad optical micro and nanostructures is reduced cross-coupling between closely spaced devices on a photonic integrated circuit. In order to evaluate the cross-coupling properties of the metal-clad waveguide, a coupling parameter ξ is defined as the ratio of the modal power outside the waveguide to the total power of the mode.

$$\xi = \frac{\int_{outside\ waveguide} \Re\{\bar{E} \times \bar{H}^*\}.\hat{z}\, dS}{\int \Re\{\bar{E} \times \bar{H}^*\}.\hat{z}\, dS} \tag{10}$$

2.4 Verification

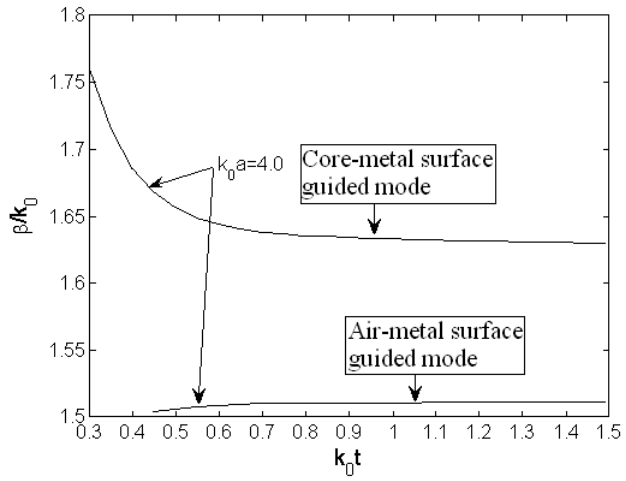

Figure 4: Normalized phase constant as a function of metal cladding thickness for the normalized waveguide radius $k_0a = 4$ for verification of the developed Helmholtz equation solver with a result in [3].

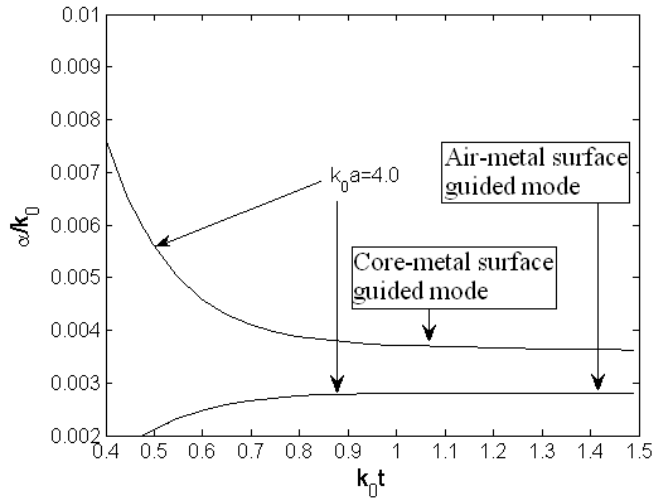

Figure 5: Normalized attenuation constant as a function of metal cladding thickness for the normalized waveguide radius $k_0a = 4$ for verification of the developed Helmholtz equation solver with a result in [3].

The results in [3] for $k_0 a = 4$ in Figs. 1(a) and 1(b) are re-produced for verification purposes in Figs. 4 and 5. The wavelength of operation, $\lambda = 0.633\mu m$, the inner and outer refractive indices are equal to 1.5, and silver with a relative permittivity of $-19 + i0.53$ serves as metal cladding.

2.5 Results

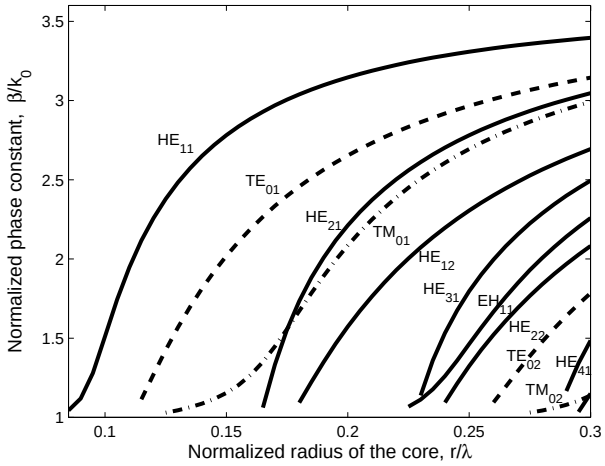

Figure 6: Normalized phase constant as a function of core radius for a nanowire waveguide with no metal cladding.

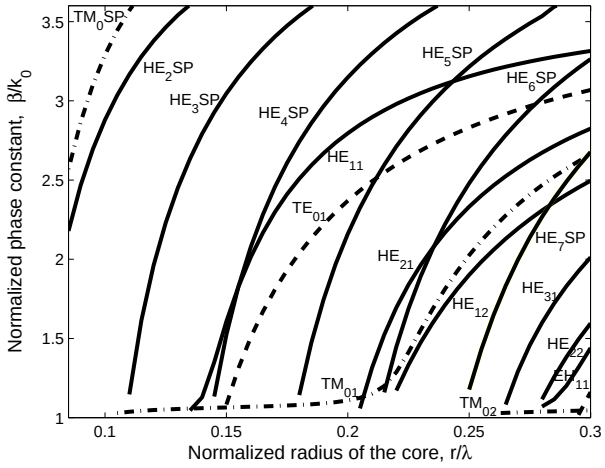

Figure 7: Normalized phase constant as a function of core radius for a nanowire waveguide with metal cladding of thickness 20 nm.

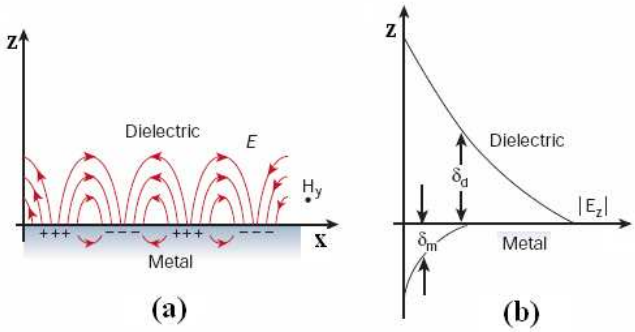

Figure 8: A surface plasmon mode at a metal-dielectric interface [7]. (a) Oscillating charges and field profile of a surface plasmon mode. (b) The absolute value of the longitudinal field as a function of distance from the interface. Note that it is high at the interface.

Fig. 6 and Fig. 7 are the plots of normalized phase constant β vs. the radius of the passive cylindrical dielectric waveguide, with and without metal cladding respectively. As shown in the figures, the metal cladding has two effects. The first effect is that, it gives rise to surface plasmon modes, whose Poynting vector is largest at the dielectric-metal surface. (The other modes, which exist in both, unclad and clad waveguides,

shall be referred to as core guided modes.) The second effect is that the radius at which the core guided modes are cut off is increased in the metal-clad waveguide. This is due to tighter confinement of the mode patterns of the core guided modes in the metal-clad waveguide, which leads to a smaller value of β for a particular radius. The first effect is not observed in the TE modes, because TE polarized surface plasmon modes do not exist [120]. The existence of surface plasmon modes depend on the field pattern. TE modes have only one electric field vector component, which is perpendicular to the plane of incidence. From Fig .8, it can be seen that the surface plasmon modes require two electric field components, parallel to the plane of incidence. One field component (E_x in Fig. 8), being continuous and the other field component (E_z in Fig. 8), being discontinuous at the interface to cause oscillating charges (surface plasmon mode propagation) at the interface. Such field pattern can only be excited by TM and hybrid modes.

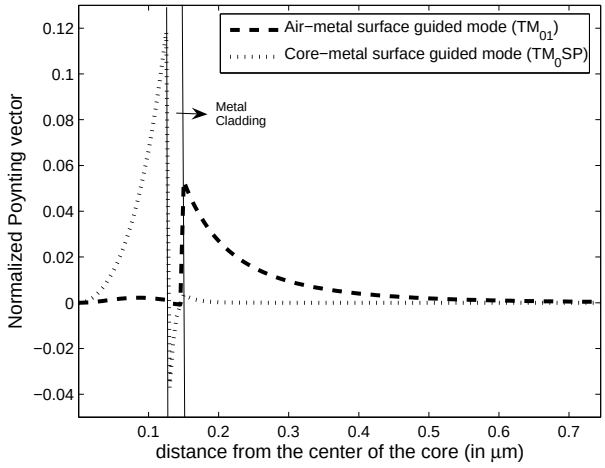

Figure 9: Normalized Poynting vector of air-metal surface guided (symmetric surface plasmon) and core-metal surface guided (asymmetric surface plasmon) TM modes for a fixed core radius of 130 nm and a cladding thickness of 20 nm.

Two types of TM and hybrid surface plasmon modes exist. The first type is guided by the core-metal surface. They are asymmetric surface plasmon modes [18, 3] because

the transverse electric fields do not become equal to zero in the metal cladding. The second type is guided by the air-metal surface. They are also known as symmetric surface plasmon modes [18, 3] because the transverse electric fields do not become equal to zero in the metal cladding. Typical intensity patterns of these two types of modes are plotted in Fig. 9 for a core radius of 130 nm and a cladding thickness of 20 nm.

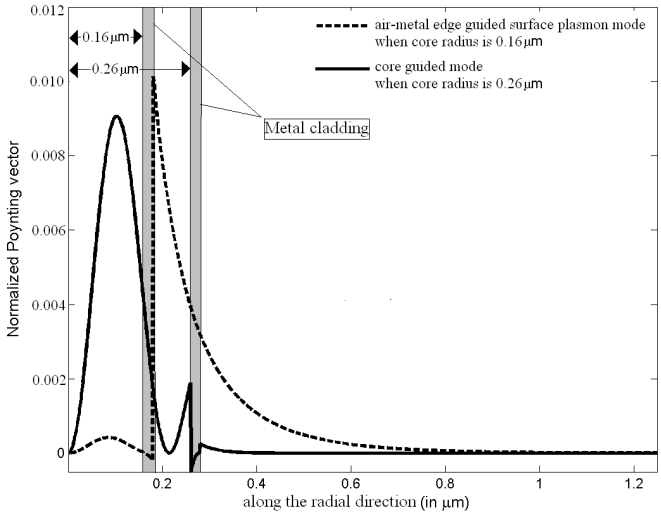

[H]

Figure 10: Normalized Poynting vector of TM_{01} mode for two different core radii. The air-metal surface guided mode for small radius ($0.16\mu m$) transforms into a core guided mode for larger radius ($0.26\mu m$).

For small values of the waveguide core radius, only surface plasmon modes are supported. The modes guided at the air-metal surface have relatively low loss and hence are known as long range surface plasmon modes [18]. These modes are of practical interest in nanophotonics. With an increase in radius, the air-metal surface guided modes become core guided modes as shown in Fig. 10. By contrast, the modes guided by the core-metal surface are very lossy.

For values of the waveguide core radius less than 85 nm in the considered structure, only core-metal surface guided modes exist, and therefore these radii are not of much

practical interest for lasers. All TM and hybrid core-metal surface guided modes are represented with an affix 'SP' and the corresponding azimuthal mode number as in Fig. 7.

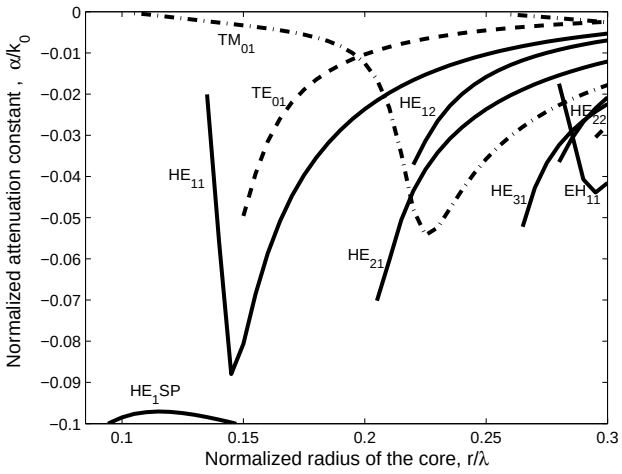

Figure 11: Normalized attenuation constant as a function of core radius for a nanowire waveguide with metal cladding of thickness 20 nm. HE_{11} and TM_{01} modes show a transformation from high-loss (air-metal) surface guided modes to low-loss core guided modes.

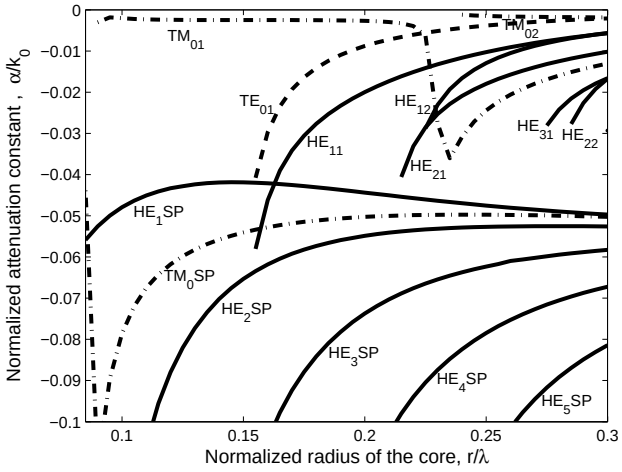

Figure 12: Normalized attenuation constant as a function of core radius for a nanowire waveguide with metal cladding of thickness 50 nm. The losses of the core-metal surface guided modes are reduced relative to the 20 nm thick cladding.

We consider a reasonable minimum metal thickness of 20 nm [144], and regard it as thin metal coating. As will be seen later, we observed that for thicknesses greater than 50 nm, the attenuation is almost independent of thickness. Therefore 50 nm is referred to as a thick metal coating. Fig. 11 and Fig. 12 are plots of normalized attenuation constant as a function of waveguide core radius for thin (20 nm) and thick (50 nm) metal-clad cylindrical passive waveguides respectively. As stated earlier, the core-metal surface guided modes suffer heavy losses, as compared to core guided and air-metal surface guided modes. It is interesting to note the loss vs. radius behavior of TM_{01} and TM_{02} modes. These modes have relatively small loss for small radii, and the loss increases with radius. After attaining a peak, the loss decreases with radius until it asymptotically approaches a constant value. The HE_{11} mode also shows similar behavior. To explain this, we must examine the mode intensity patterns of a single-mode at different radii. Fig. 10 is a plot of the Poynting vector of a TM_{01} mode formed in a thin metal-clad waveguide at a radius of 160 nm and 260 nm. As seen in Fig. 10, it is an air-metal surface guided mode (symmetric surface plasmon

mode) for small radii, with relatively small loss. The loss of this mode increases as the radius is increased. However, the mode gradually transforms into a core guided mode, as seen in the same figure. Following this transformation, the loss decreases with increasing radius, as the core becomes large enough to accomodate the mode without much overlap with the metal.

However all TE modes and higher-order HE_{pq} modes exist as core guided modes. This causes losses to decrease, and asymptotically approach a constant value with increase in radius.

The introduction of thicker metal cladding reduces the losses of all core-metal surface guided modes, but does not strongly affect the loss of air-metal surface guided modes. Thicker metal cladding also increases the radius for which air-metal surface guided modes transform into core guided modes. In order to understand the decrease in the losses as the metal cladding thickness increases, a factor representing the normalized electric field overlap with the metal, Δ_m is defined and it is similar to the confinement factor in [139],

$$\Delta_m = \frac{\beta}{\eta k_0} \frac{\int_{inside\ metal} |\bar{E}|^2 \, dS}{\int \Re\{\bar{E} \times \bar{H}^*\}.\hat{z} \, dS} \tag{11}$$

As the factor, Δ_m decreases, the modal loss decreases as well [139]. Fig. 13 illustrates this with a plot of normalized attenuation constant and normalized metal overlap vs. metal thickness for both, core-metal surface guided modes and air-metal surface guided modes.

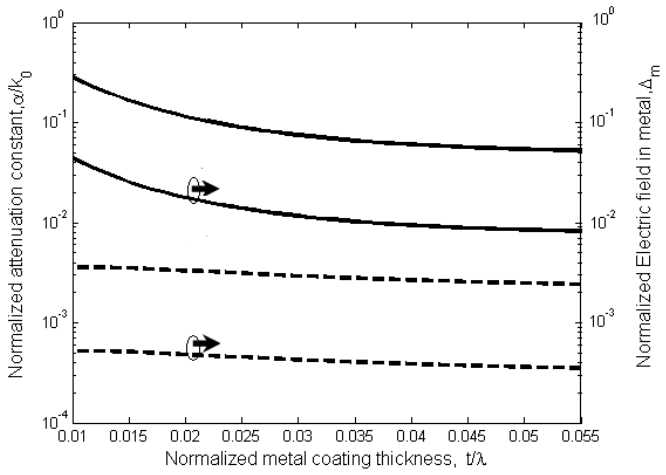

Figure 13: Normalized attenuation constant and normalized electric field in the metal for both core-metal surface guided modes (solid lines) and air-metal surface guided modes (broken lines) as a function of metal coating thickness for a fixed radius of 150 nm. This confirms the proportionality of total normalized electric field in the metal to the attenuation constant.

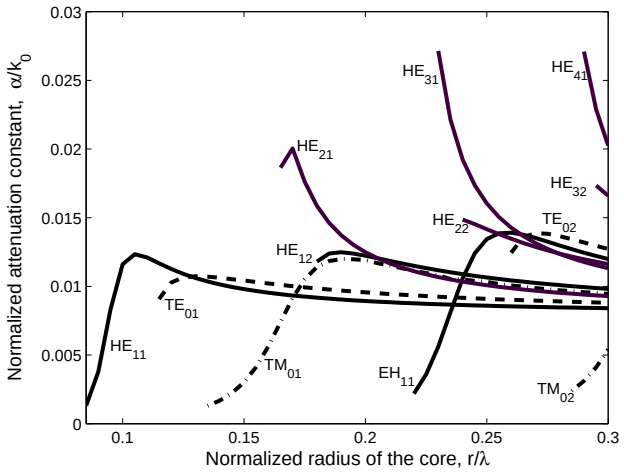

[H]

Figure 14: Normalized attenuation constant as a function of core radius for an active nanowire waveguide with no metal cladding. Gain is seen in all modes.

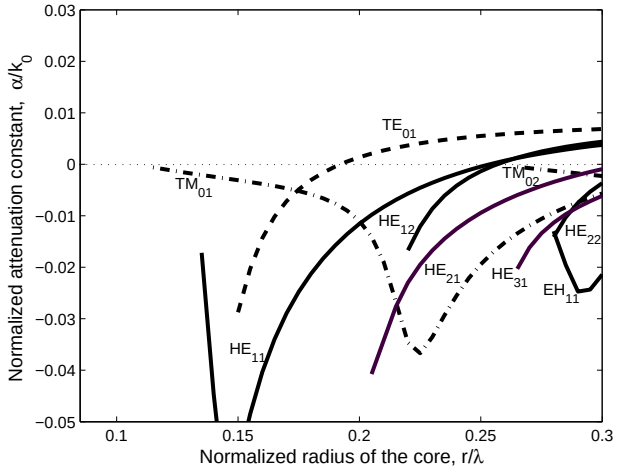

[H]

Figure 15: Normalized attenuation constant as a function of core radius for an active nanowire waveguide with metal cladding of thickness 20 nm.

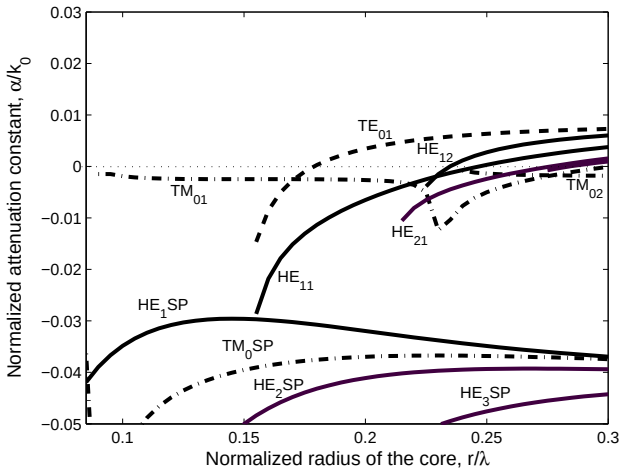

[H]

Figure 16: Normalized attenuation constant as a function of core radius for an active nanowire waveguide with metal cladding of thickness 50 nm. The losses of the surface guided modes and TM modes are reduced relative to the 20 nm thick cladding.

In order to examine the amplification properties of metal-clad waveguides with gain, a material gain of 1000 cm^{-1} was introduced in the core. As expected, the loss properties of the modes change significantly after this change. Fig. 14 is a plot of

normalized attenuation constant as a function of the radius of the active waveguide without metal cladding. Fig. 15 and Fig. 16 are the plots of normalized attenuation constant of the active waveguide with thin and thick metal cladding, respectively. Both, TM and hybrid core and air surface guided modes appear in the waveguide, even without metal cladding because the core is now active. The modal gain depends on the normalized strength of the electric field inside the waveguide (gain overlap factor) [139, 90], and therefore the core-air surface guided modes show small gain for small waveguide radii. As the radius increases, these modes gradually become core guided modes resulting in increased gain, due to improved power overlap with the gain region.

As seen above, in the metal-clad waveguide, the core-metal surface guided modes are very lossy; however, the losses are reduced in the waveguide with thicker metal cladding, allowing a net gain and the possibility of lasing in core-metal surface guided mode. The air-metal surface guided modes exhibit little normalized electric field in the core. So, they show little change in gain, with thin or thick metal cladding.

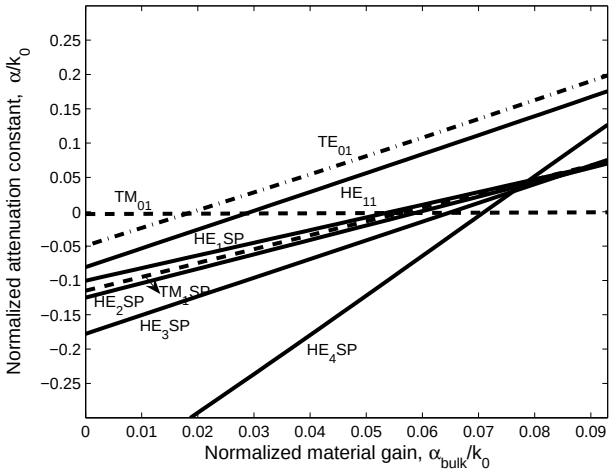

Figure 17: Normalized attenuation constant as a function of normalized material gain for an active nanowire waveguide with core radius of 150 nm and a metal cladding of thickness, 20 nm. The TE_{01} and HE_{11} modes show potential for lasing, but the surface plasmon modes do not.

Another observation is, for some intermediate values of radii, TE_{01} [88] modes showed a gain with thin and thick metal cladding and it can be seen in Fig. 15 and Fig. 16. When modal gain was plotted against material gain for a radius of 150 nm, and a metal cladding thickness of 20 nm as in Fig. 17, TE_{01} and HE_{11} showed an increased gain. So, even for smaller material gain compared to other modes, TE_{01} and HE_{11} showed some potential for lasing. Since both modes have a small fraction of their modal field in the metal cladding, they are less affected by loss due to the metal. Thus one advantage of the metal cladding is a reduction in the number of transverse modes besides the TE_{01} and HE_{11} modes competing to lase. However, it appears that the surface plasmon modes are not attractive candidates for lasing in this geometry.

The confinement factor, Γ and loss ($\alpha_{without\ gain}$) of various waveguide modes are tabulated in the following page. The calculations were done for an optimum radius of 220 nm, where TE_{01} mode gain has an increased separation from other modes.

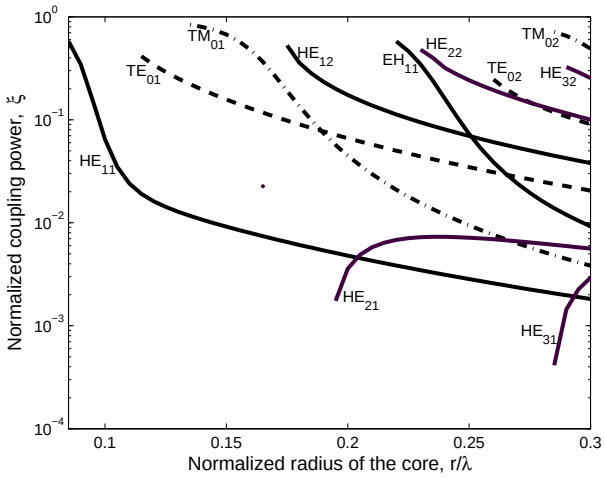

Figure 18: Normalized coupling power as a function of core radius for an active nanowire waveguide with no metal cladding.

Using the bulk material gain, the net gain of the waveguide can be obtained from the parameters in the table.

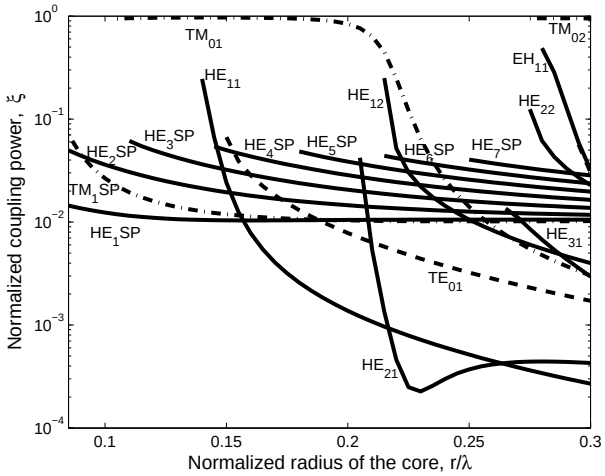

Figure 19: Normalized coupling power as a function of core radius for an active nanowire waveguide with metal cladding of thickness 20 nm. The coupling is reduced for most modes relative to the waveguide with no metal cladding.

Table 1: Confinement factor and attenuation constant associated with various modes

	TM_{01}		TE_{01}		HE_{11}		TM_1SP		HE_1SP	
	Γ	α (in $1/\mu$m)	Γ	α (in $1/\mu$m)	Γ	α (in $1/\mu$m)	Γ	α (in $1/\mu$m)	Γ	α (in $1/\mu$m)
no metal	1.0588	0	1.1675	0	1.0956	0	-	-	-	-
thin metal	1.6750	-0.3016	1.3625	-0.0452	1.3635	-0.1043	1.9250	-0.1100	1.9000	-0.6817
thick metal	0.0375	-0.0245	1.3875	-0.0377	1.4875	-0.0949	1.6375	-0.3135	1.5625	-0.2871

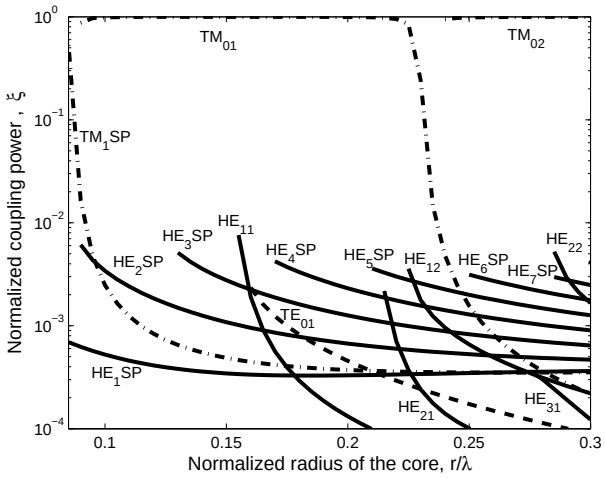

Figure 20: Normalized coupling power as a function of core radius for an active nanowire waveguide with metal cladding of thickness 50 nm. The coupling is reduced for most modes relative to the 20 nm thick cladding.

In order to assess the intercavity coupling properties of the cylindrical waveguide, with and without metal cladding, the parameter ξ, which gives the normalized power outside the waveguide was calculated. As expected, the cylindrical waveguide with metal cladding shows reduced coupling relative to the waveguide without metal cladding for core-guided and core-metal surface guided modes. Fig. 18, Fig. 19 and Fig. 20 show the plots of ξ without metal cladding, with thin metal cladding and with thick metal cladding respectively. The power confined within the core increases with the thickness of the metal cladding for core guided and core-metal surface guided modes, and hence reduces coupling to adjacent regions. Therefore a metal cladding can be useful to help reduce the coupling between closely-spaced arrays of lasers. Though air-metal surface guided modes have small loss, they carry a large fraction of their power outside the waveguide, and therefore will exhibit increased coupling. Also, increasing the metal layer thickness will have little effect on coupling of air-metal surface guided modes.

2.6 Conclusions

The effects of metal cladding on a subwavelength active dielectric cylindrical waveguide for nanowire lasers and micropost cavities have been calculated. The metal cladding give rise to two classes of surface plasmon modes, the core-metal surface guided modes and air-metal surface guided modes. The latter is less lossy compared to the former, and they gradually become core guided modes with an increase in the radius of the waveguide. Although air-metal surface guided modes exhibit less loss compared to core-metal surface guided modes, the gain overlap factor of these modes is also small. By contrast, the power concentrated in the core by core-metal surface modes is high, but their losses are also high. Thus, both surface guided modes (or surface plasmon modes) would require considerable pumping in order to lase, and may not be useful in practice for this geometry.

With or without metal cladding, guided modes have maximum power concentrated in the core. As seen from the results presented in Figs. 11, 12, 15, 16 and 17, TE_{01} and HE_{11} modes are less affected by the metal cladding, compared to other modes. By using metal cladding with suitable thickness, the modal losses of other modes can be increased, resulting in improved modal discrimination.

Finally, the metal cladding reduces the coupling of core-guided modes between two or more adjacent laser elements as shown in Figs. 19 and 20.

CHAPTER III

COMPREHENSIVE THEORY OF PLANEWAVE EXPANSION-BASED EIGENMODE METHOD FOR SCATTERING-MATRIX ANALYSIS OF PHOTONIC STRUCTURES

This chapter closely follows our journal article that has been submitted and is under review [73].

3.1 Introduction

Historically, real space approaches based on finite difference and finite element techniques have been attractive candidates for designing photonic structures. This is because of their robust and straightforward computation schemes. However, they are generally memory-intensive and processor-intensive. On the other hand, approaches based on modal expansion methods, such as coupled mode theory [40, 143, 79, 29, 52] and eigenmode expansions [134, 152, 11] are faster for many problems. They [143, 79, 11] are based on discretizing the dielectric structure into a set of 1D or 2D layers along the out-of-plane direction. Each layer is invariant in the out-of-plane direction. First, 1D/2D vectorial layer modes in each layer are calculated. Using the layer modes as basis functions, a mode-matching analysis is carried out along the out-of-plane direction using scattering matrices to calculate the coupling coefficients. The expansion coefficients and the in-plane vectorial modes are then used to propagate an incident wave throughout the device, and calculate the field distribution.

One type of modal method is the planewave expansion method, which has been extensively used to calculate scattering from diffraction gratings. A good review on

the usage of planewave expansion for 1D gratings can be found in [40] and references therein. The planewave expansion was extended to finite sized waveguides [79] with lateral PML boundary conditions, and the Gibbs phenomenon was mitigated in [84, 78]. Another modal approach commonly used is the eigenmode expansion [152, 14]. A PML coating on lateral boundaries [14] reduces the lateral reflection, and hence artificially creates a lateral open boundary condition.

The eigenmode expansion in [14] relies on numerically calculating modes from analytically derived dispersion relations for each 2D slice in the device. This limits the type of devices for which the method is applicable. It cannot be applied for a problem such as designing 3D photonic crystal line defects or photonic crystal cavities. The planewave-based modal expansion in [143, 79] is applicable for a broader range of devices, compared to the structures with simpler (analytically solvable dispersion relation) in-plane layers [14]. It is because, the planewave-based modal method uses a planewave basis for numerically calculating vectorial modes in each 2D slice. This method is also fast since the number of planewaves required is much less than the number of grids required in real space approaches [79, 29]. One disadvantage of planewave expansion method is it results in a non-sparse Helmholtz equation matrix, and therefore operating with them becomes inefficient especially for large structures like photonic crystal defect cavities. It requires large memory allocations and time consuming operation to store, and operate on the non-sparse Helmholtz equation matrix. For this reason, real space methods may become more attractive for large structures.

On the other hand, the planewave expansion method for finding layer modes can be made matrix-free in both uniform and non-uniform co-ordinates [115, 111]. This is especially useful for finding photonic crystal defect modes, as the number of planewaves can be increased with just $O(N)$ memory requirement and $O(N \log(N))$ time requirement. This leads to a question: is the matrix-free planewave expansion

method efficient for calculating layer basis modes for use in the scattering matrix analysis of reflection and transmission from layers containing photonic crystal defect cavities? If large number of layer eigenmodes are required to match modes at the interfaces between 2D layers, then planewave expansion may become very inefficient, especially for large photonic crystal defects. However, for some modes, only a limited number of planewaves of lower orders carry most of the power in the mode, which reduces the number of planewaves that must be used to represent the mode when mode-matching is carried out at interfaces between layers. To help determine the efficiency of this method, in this work photonic crystal structures both without and with defects are considered.

In the next section, we present a theory integrating planewave expansion, eigenmode matching, scattering matrix theory, and round-trip operators for analyzing photonic structures. The derivation of each of these has been carried out previously in [143, 79, 29, 11, 52, 137, 125], but here we demonstrate their efficient integration. First, a theory of planewave expansion that uses a numerical Fourier operator [115, 111, 60] in order to introduce automation, memory efficiency and speed efficiency in the calculation of vectorial layer modes is presented. The matrix-free planewave expansion method is then used in conjunction with mode-matching analysis for multilayered structures. Then a derivation of a round-trip operator is presented for the calculation of 3D modes. Unlike in previous references [29, 12], the round-trip operator is used in phase space to find guided modes in photonic crystal and single mode photonic crystal defect structures. The phase space analysis of round trip operator gives the $3D$ modes in a more straightforward and easier way, than magnitude analysis [29]. The theory section is followed by a verification section, in which the method is used to reproduce the result of scattering from a photonic crystal slab, and of calculating guided modes in a photonic crystal slab. Then, a convergence analysis is applied for the calculation of scattering from a photonic crystal slab, a small photonic

crystal defect slab and a large photonic crystal defect slab for stability analysis of the method.

3.2 Theory

3.2.1 Planewave expansion of propagating, evanescent and complex modes of 2D layers

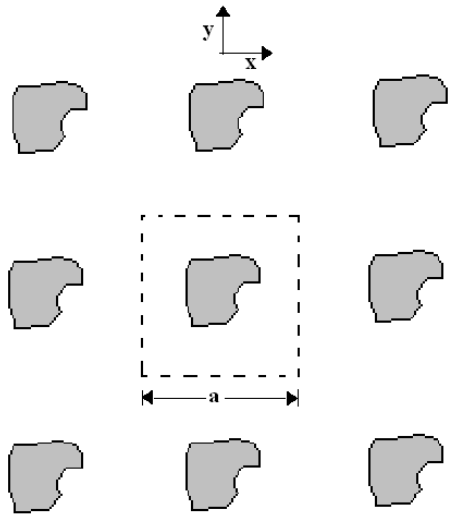

Figure 21: A periodic structure with arbitrary dielectric profile.

A similar matrix-free Helmholtz operator has already been presented in [115, 111] for photonic crystal fibers, which is a single-layer problem. In this work, the derived Helmholtz equation operator is not similar to that in [115, 111], and the modes calculated using the operator is used along with the mode-matching approach for multi-layered structures.

Consider a 2D periodic layer of arbitrary dielectric profile as shown in Fig. 21 with a periodicity of a, which is also the dimension of the computational domain in real space. The following analysis is used to calculate all the propagating, evanescent, and complex modes in the periodic structure. Even though the Fig. 21 is square lattice, the following theory is not restricted by lattice shape.

For aperiodic structures like photonic crystal defects, the periodicity is increased

such that the effect of periodicity is negligible, atleast for few lower order modes of interest. Since the in-plane boundary conditions are periodic without the use of PML [11], the method is not suitable for calculating in-plane losses. Periodic with PML lateral boundary conditions can overcome the shortcoming [77, 50, 69].

The two Maxwell curl equations for time-harmonic fields in a source-free medium are,

$$\nabla \times H = i\omega\epsilon E, \quad \nabla \times E = -i\omega\mu H \tag{12}$$

where $\epsilon = \epsilon_0\epsilon_r$, ϵ_0 is the permittivity of free space, ϵ_r is the relative permittivity of the medium under consideration, $\mu = \mu_0$ is the permeability of the medium and ω is the frequency (in radians/sec) of the electromagnetic wave.

Each 2D slice is uniform along $z-$direction. So, for the calculation of vectorial Bloch modes (basis modes), $\frac{\partial}{\partial z} = -ik_z$ is substituted, and then we arrive at the following form for the transverse fields [29],

$$-ik_z \begin{bmatrix} H_x \\ H_y \end{bmatrix} = \begin{bmatrix} \frac{\partial}{\partial x}\frac{i}{\omega\mu}\frac{\partial}{\partial x} + i\omega\epsilon & -\frac{\partial}{\partial x}\frac{i}{\omega\mu}\frac{\partial}{\partial y} \\ \frac{\partial}{\partial y}\frac{i}{\omega\mu}\frac{\partial}{\partial x} & -\frac{\partial}{\partial y}\frac{i}{\omega\mu}\frac{\partial}{\partial y} - i\omega\epsilon \end{bmatrix} \begin{bmatrix} E_y \\ E_x \end{bmatrix} \tag{13}$$

$$-ik_z \begin{bmatrix} E_x \\ E_y \end{bmatrix} = \begin{bmatrix} -\frac{\partial}{\partial x}\frac{i}{\omega\epsilon}\frac{\partial}{\partial x} - i\omega\mu & -\frac{\partial}{\partial x}\frac{i}{\omega\epsilon}\frac{\partial}{\partial y} \\ -\frac{\partial}{\partial y}\frac{i}{\omega\epsilon}\frac{\partial}{\partial x} & \frac{\partial}{\partial y}\frac{i}{\omega\epsilon}\frac{\partial}{\partial y} + i\omega\mu \end{bmatrix} \begin{bmatrix} H_y \\ H_x \end{bmatrix} \tag{14}$$

The above two equations can be combined and expressed only in terms of magnetic field as in (15).

$$\begin{bmatrix} \left(\left(\frac{\partial}{\partial x}\frac{i}{\omega\mu}\frac{\partial}{\partial x} + i\omega\epsilon\right)\left(\frac{\partial}{\partial y}\frac{i}{\omega\epsilon}\frac{\partial}{\partial y} + i\omega\mu\right) - \left(\frac{\partial}{\partial x}\frac{i}{\omega\mu}\frac{\partial}{\partial y}\right)\left(\frac{\partial}{\partial x}\frac{i}{\omega\epsilon}\frac{\partial}{\partial y}\right)\right) & \left(-\left(\frac{\partial}{\partial x}\frac{i}{\omega\mu}\frac{\partial}{\partial x} + i\omega\epsilon\right)\left(\frac{\partial}{\partial y}\frac{i}{\omega\epsilon}\frac{\partial}{\partial x}\right) + \left(\frac{\partial}{\partial x}\frac{i}{\omega\mu}\frac{\partial}{\partial y}\right)\left(\frac{\partial}{\partial x}\frac{i}{\omega\epsilon}\frac{\partial}{\partial x} + i\omega\mu\right)\right) \\ \left(\left(\frac{\partial}{\partial y}\frac{i}{\omega\mu}\frac{\partial}{\partial x}\right)\left(\frac{\partial}{\partial y}\frac{i}{\omega\epsilon}\frac{\partial}{\partial y} + i\omega\mu\right) - \left(\frac{\partial}{\partial y}\frac{i}{\omega\mu}\frac{\partial}{\partial y} + i\omega\epsilon\right)\left(\frac{\partial}{\partial x}\frac{i}{\omega\epsilon}\frac{\partial}{\partial y}\right)\right) & \left(-\left(\frac{\partial}{\partial x}\frac{i}{\omega\epsilon}\frac{\partial}{\partial y}\right)\left(\frac{\partial}{\partial y}\frac{i}{\omega\epsilon}\frac{\partial}{\partial y} + i\omega\mu\right) + \left(\frac{\partial}{\partial y}\frac{i}{\omega\mu}\frac{\partial}{\partial y} + i\omega\epsilon\right)\left(\frac{\partial}{\partial x}\frac{i}{\omega\epsilon}\frac{\partial}{\partial x} + i\omega\mu\right)\right) \end{bmatrix} \begin{bmatrix} H_x \\ H_y \end{bmatrix} = -k_z^2 \begin{bmatrix} H_x \\ H_y \end{bmatrix} \tag{15}$$

Let the magnetic field,

$$\vec{H}(\vec{r}) = \sum_G (H_{Gx}\hat{x} + H_{Gy}\hat{y} + H_{Gz}\hat{z})\psi_{k+G}(x, y)\exp(-ik_z z)$$

where ψ_G can be an arbitrary set of orthonormal functions, representing a complete basis [29] set. On substituting the above equation for $\vec{H}(\vec{r})$ in (15), multiplying by the conjugate of the basis function on both sides, and integrating throughout the real space, (15) becomes,

$$\begin{bmatrix} A_{11} & A_{12} \\ A_{21} & A_{22} \end{bmatrix} \begin{bmatrix} H_{Gx} \\ H_{Gy} \end{bmatrix} = k_z^2 B \begin{bmatrix} H_{Gx} \\ H_{Gy} \end{bmatrix} \tag{16}$$

where,

$$\begin{aligned}
A_{11} &= -\int_\Omega \psi^*_{k+G'} \left(\left(\frac{\partial}{\partial x} \frac{i}{\omega\mu} \frac{\partial}{\partial x} + i\omega\epsilon \right) \left(\frac{\partial}{\partial y} \frac{i}{\omega\epsilon} \frac{\partial}{\partial y} + i\omega\mu \right) - \right. \\
&\quad \left. \left(\frac{\partial}{\partial x} \frac{i}{\omega\mu} \frac{\partial}{\partial y} \right) \left(\frac{\partial}{\partial x} \frac{i}{\omega\epsilon} \frac{\partial}{\partial y} \right) \right) \psi_G \, d\Omega \\
A_{12} &= -\int_\Omega \psi^*_{k+G'} \left(- \left(\frac{\partial}{\partial x} \frac{i}{\omega\mu} \frac{\partial}{\partial x} + i\omega\epsilon \right) \left(\frac{\partial}{\partial y} \frac{i}{\omega\epsilon} \frac{\partial}{\partial x} \right) + \right. \\
&\quad \left. \left(\frac{\partial}{\partial x} \frac{i}{\omega\mu} \frac{\partial}{\partial y} \right) \left(\frac{\partial}{\partial x} \frac{i}{\omega\epsilon} \frac{\partial}{\partial x} + i\omega\mu \right) \right) \psi_G \, d\Omega \\
A_{21} &= -\int_\Omega \psi^*_{k+G'} \left(\left(\frac{\partial}{\partial y} \frac{i}{\omega\mu} \frac{\partial}{\partial x} \right) \left(\frac{\partial}{\partial y} \frac{i}{\omega\epsilon} \frac{\partial}{\partial y} + i\omega\mu \right) - \right. \\
&\quad \left. \left(\frac{\partial}{\partial y} \frac{i}{\omega\mu} \frac{\partial}{\partial y} + i\omega\epsilon \right) \left(\frac{\partial}{\partial x} \frac{i}{\omega\epsilon} \frac{\partial}{\partial y} \right) \right) \psi_G \, d\Omega \\
A_{22} &= -\int_\Omega \psi^*_{k+G'} \left(- \left(\frac{\partial}{\partial x} \frac{i}{\omega\epsilon} \frac{\partial}{\partial y} \right) \left(\frac{\partial}{\partial y} \frac{i}{\omega\epsilon} \frac{\partial}{\partial y} + i\omega\mu \right) + \right. \\
&\quad \left. \left(\frac{\partial}{\partial y} \frac{i}{\omega\mu} \frac{\partial}{\partial y} + i\omega\epsilon \right) \left(\frac{\partial}{\partial x} \frac{i}{\omega\epsilon} \frac{\partial}{\partial x} + i\omega\mu \right) \right) \psi_G \, d\Omega \\
B &= \int_\Omega \psi^*_{k+G'} \psi_{k+G} \, d\Omega
\end{aligned}$$

The values of $A_{11},\ A_{12},\ A_{21},\ A_{22}$ and B depend on the chosen basis function, ψ_G and the periodic domain area, Ω.

Let $\psi_G(\vec{r}_\parallel) = \exp(-i\vec{G}.\vec{r}_\parallel)$, where $\vec{G} = (\vec{G_1} + \vec{G_2})$ is the reciprocal lattice vectors of the periodic medium. If $\vec{u_1}$ and $\vec{u_2}$ represent the two in-plane real space lattice vectors of a 2D slice, then reciprocal lattice vectors are,

$$\vec{G_1} = 2\pi \frac{\vec{u_2} \times \hat{z}}{\vec{u_1}.(\vec{u_2} \times \hat{z})} \tag{17}$$

$$\vec{G_2} = 2\pi \frac{\hat{z} \times \vec{u_1}}{\vec{u_2}.(\hat{z} \times \vec{u_1})} \tag{18}$$

and $r_{\parallel}$ is the in-plane spatial co-ordinate. Then,

$$\vec{H}(\vec{r}) = \sum_{G} (H_{Gx}\hat{x} + H_{Gy}\hat{y} + H_{Gz}\hat{z}) \exp(-i\vec{G}.\vec{r}_{\parallel}) \exp(-i\vec{k}.\vec{r})$$

If $G_x = G_{1x} + G_{2x}$ and $G_y = G_{1y} + G_{2y}$. Then, by substituting $\frac{\partial}{\partial x} = -i(k_x + G_x)$ and $\frac{\partial}{\partial y} = -i(k_y + G_y)$, the components of A can be reduced using Fourier (FT) and inverse Fourier (IFT) transforms to the following form,

$$\begin{aligned}
A_{11} &= -(k_x + G_x)^2 - FT..\epsilon..IFT..(k_y + G_y)..FT..\frac{1}{\epsilon}.. \\
&\quad ..IFT..(k_y + G_y) + \omega^2\mu..FT..\epsilon..IFT.. \\
A_{12} &= -(k_x + G_x)(k_y + G_y) + \\
&\quad ..FT..\epsilon..IFT..(k_y + G_y)..FT..\frac{1}{\epsilon}..IFT..(k_x + G_x).. \\
A_{21} &= -(k_y + G_y)(k_x + G_x) + \\
&\quad ..FT..\epsilon..IFT..(k_x + G_x)..FT..\frac{1}{\epsilon}..IFT..(k_y + G_y).. \\
A_{22} &= -(k_y + G_y)^2 - FT..\epsilon..IFT..(k_x + G_x)..FT..\frac{1}{\epsilon}.. \\
&\quad ..IFT..(k_x + G_x) + \omega^2\mu..FT..\epsilon..IFT.. \\
B &= \delta_{G'G}
\end{aligned}$$

For a fixed frequency, the inputs for the operator A are the in-plane Bloch wavevectors, k_x and k_y, permittivity and permeablity profiles, which can be arbitrary, and frequency, ω. It has to be noted that because of the FT and IFT operators, A is matrix-free and is always stored in the form of operator-vector products. For a uniform medium, off-diagonal elements are zero and the other diagonal elements take the form, $\omega^2\epsilon\mu - (k_x + G_x)^2 - (k_y + G_y)^2 = k_z^2$.

For a non-absorbing linear medium, the eigensolution of the operator, A yields three kinds of modes depending on dimensions of the structure and the wavelength of operation. They are:

1. Propagating modes: modes with real value of out-of-plane wave-vector, k_z.

2. Evanescent modes: modes with imaginary value of k_z, and they do not carry power.

3. Complex modes: modes with complex value of k_z, and they always occur in complex conjugate pairs. Together, they also do not [113, 106, 107] carry power.

Though the above formulations solve for all propagating, evanescent and complex modes at a given frequency, they don't guarantee the satisfaction of divergence free condition [57], $\nabla.\vec{H} = 0$ (assuming μ to be constant). In order to ensure this, a different set of basis vectors are defined. Let $\vec{k}_{Gx} = \vec{k}_x + \vec{G}_x$, $\vec{k}_{Gy} = \vec{k}_y + \vec{G}_y$, $\vec{k}_{tG} = \vec{k}_{Gx} + \vec{k}_{Gy}$ and $\vec{k}_G = \vec{k}_{Gx} + \vec{k}_{Gy} + \vec{k}_z$, then the two polarization directions can be defined, such that they are perpendicular to the direction of propagation, and hence they satisfy divergence free condition similar to the analysis in [60],

$$\begin{aligned} e_{\vec{G}1} &= \vec{k}_G \times \hat{z} \\ &= (\vec{k}_{Gx} + \vec{k}_{Gy} + \vec{k}_z) \times \hat{z} \\ &= -\hat{y}k_{Gx} + \hat{x}k_{Gy} \qquad (19) \\ e_{\vec{G}2} &= \vec{k}_G \times \vec{k}_G \times \hat{z} \\ &= (\vec{k}_{Gx} + \vec{k}_{Gy} + \vec{k}_z) \times (-\hat{y}k_{Gx} + \hat{x}k_{Gy}) \times \hat{z} \\ &= \hat{x}k_{Gx}k_z + \hat{x}k_{Gy}k_z - \hat{z}(k_{Gx}^2 + k_{Gy}^2) \qquad (20) \end{aligned}$$

With the above polarization directions as the basis functions,

$$\begin{aligned} \vec{H}(\vec{r}) &= \sum_G (h_{G1}\vec{e}_{G1} + h_{G2}\vec{e}_{G2}) \exp(-(\vec{k} + \vec{G}).\vec{r}) \\ &= \sum_G (h_{G1}(-\hat{y}k_{Gx} + \hat{x}k_{Gy}) + h_{G2}(\hat{x}k_{Gx}k_z + \\ &\quad \hat{y}k_{Gy}k_z - \hat{z}(k_{Gx}^2 + k_{Gy}^2))) \exp(-(\vec{k} + \vec{G}).\vec{r}) \\ &= \sum_G ((h_{G1}k_{Gy} + h_{G2}k_{Gx}k_z)\hat{x} + (-h_{G1}k_{Gx} + \\ &\quad h_{G2}k_{Gy}k_z)\hat{y} - h_{G2}(k_{Gx}^2 + k_{Gy}^2)\hat{z}) \exp(-(\vec{k} + \vec{G}).\vec{r}) \qquad (21) \end{aligned}$$

Using equations (16) and (21), it is straight forward to translate the problem to the new basis vector. The new generalized eigenvalue problem will be,

$$\begin{bmatrix} A_{11}k_{Gy} - A_{12}k_{Gx} & A_{11}k_{Gx} + A_{12}k_{Gx} \\ A_{21}k_{Gy} - A_{22}k_{Gx} & A_{21}k_{Gx} + A_{22}k_{Gy} \end{bmatrix} \begin{bmatrix} h_{G1} \\ k_z h_{G2} \end{bmatrix} = k_z^2. \begin{bmatrix} k_{Gy} & k_{Gx} \\ -k_{Gx} & k_{Gy} \end{bmatrix} \begin{bmatrix} h_{G1} \\ k_z h_{G2} \end{bmatrix} \tag{22}$$

The above equation can be further simplified by noting the fact that for each value of $\vec{G}$, the relation (22) should be satisfied. Therefore, the 2×2 matrix on the RHS can be inverted to transform the problem into a standard eigenvalue problem, i.e.,

$$\begin{bmatrix} k_{Gy} & k_{Gx} \\ -k_{Gx} & k_{Gy} \end{bmatrix}^{-1} = \frac{1}{(k_{Gx}^2 + k_{Gy}^2)} \begin{bmatrix} k_{Gy} & -k_{Gx} \\ k_{Gx} & k_{Gy} \end{bmatrix} \tag{23}$$

If $k_{Gt}^2 = (k_{Gx}^2 + k_{Gy}^2)$, then the final standard eigenvalue problem is of the form,

$$\begin{bmatrix} A_{11}'' & A_{12}'' \\ A_{21}'' & A_{22}'' \end{bmatrix} \begin{bmatrix} h_{G1} \\ k_z h_{G2} \end{bmatrix} = k_z^2 \begin{bmatrix} h_{G1} \\ k_z h_{G2} \end{bmatrix} \tag{24}$$

where,

$$
\begin{aligned}
A_{11}^{''} &= \frac{k_{Gy}}{k_{Gt}^2}(k_0^2..FT..\epsilon..IFT..k_{Gy} - FT..\epsilon.. \\
&\quad IFT..k_{Gy}..FT..\frac{1}{\epsilon}..IFT..k_{Gt}^2) - \\
&\quad \frac{k_{Gx}}{k_{Gt}^2}(-k_0^2..FT..\epsilon..IFT..k_{Gx} + \\
&\quad FT..\epsilon..IFT..k_{Gx}..FT..\frac{1}{\epsilon}..IFT..k_{Gt}^2) \qquad (25) \\
A_{12}^{''} &= \frac{k_{Gy}}{k_{Gt}^2}k_0^2..FT..\epsilon..IFT..k_{Gx} - \\
&\quad \frac{k_{Gx}}{k_{Gt}^2}k_0^2..FT..\epsilon IFT..k_{Gy} \qquad (26) \\
A_{21}^{''} &= \frac{k_{Gx}}{k_{Gt}^2}(k_0^2..FT..\epsilon..IFT..k_{Gy} - FT..\epsilon.. \\
&\quad IFT..k_{Gy}..FT..\frac{1}{\epsilon}..IFT..k_{Gt}^2) + \\
&\quad \frac{k_{Gy}}{k_{Gt}^2}(-k_0^2..FT..\epsilon..IFT..k_{Gx} + \\
&\quad FT..\epsilon..IFT..k_{Gx}..FT..\frac{1}{\epsilon}..IFT..k_{Gt}^2) \qquad (27) \\
A_{22}^{''} &= \frac{k_{Gx}}{k_{Gt}^2}(k_0^2..FT..\epsilon..IFT..k_{Gx} - k_{Gx}k_{Gt}^2) + \\
&\quad \frac{k_{Gy}}{k_{Gt}^2}(k_0^2..FT..\epsilon..IFT..k_{Gy} - k_{Gy}k_{Gt}^2) \qquad (28)
\end{aligned}
$$

The developed eigenvalue problem is now divergence-free and matrix-free. To summarize, either operator, A or operator, $A^{''}$ is used to calculate the vectorial eigenmodes (propagating, evanescent and complex modes) in 1D/2D slices of arbitrary dielectric structures for a given frequency and in-plane wavevectors.

A freely available non-Hermitian matrix-free eigensolver, based on Jacobi-Davidson method [127, 36] or Arnoldi method from ARPACK [81] can be used to find the eigensolutions.

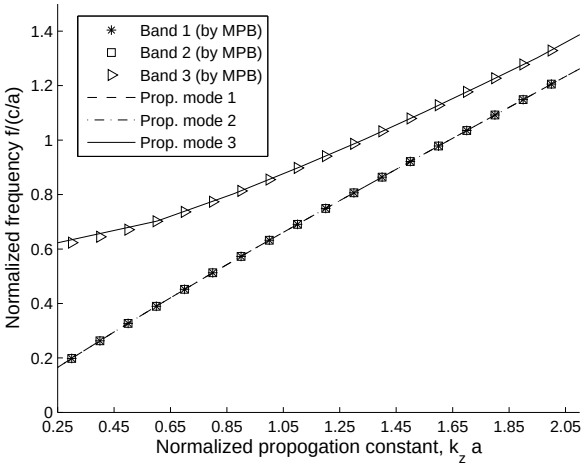

Figure 22: Comparison of dispersion of a square lattice photonic crystal with MPB package.

To verify the above formulations, the dispersion relation f Vs. k_z for square lattice holes in a dielectric was calculated, and compared with the dispersion relation by the MPB package in Fig. 22. Though the results match, confirmation of the validity of evanescent modes was not possible since MPB works only for propagating modes. However, further indirect validation of the calculation of all modes was done by matching the results of reflection and transmission with a previously published result [32], and is presented in the next section.

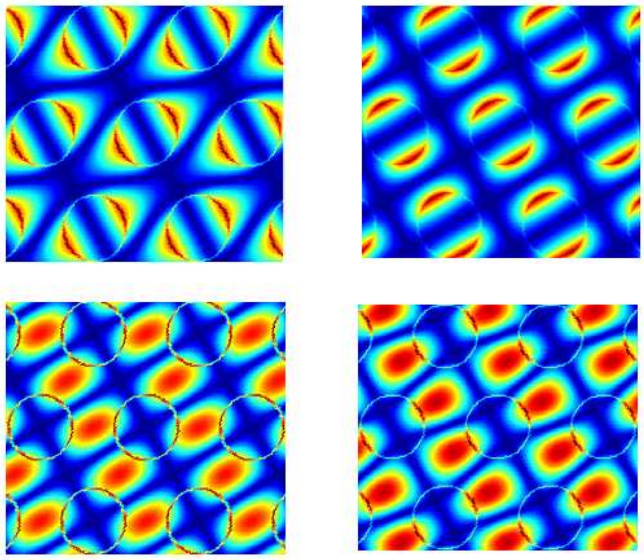

Figure 23: The spatial distribution of $|E_z|$ for first four modes at an arbitrary frequency and normal incidence. The top two modes are propagating and the bottom two are evanesecent.

The spatial distribution of $|E_z|$ for first four modes in a triangular photonic crystal formed by holes in a dielectric is shown in Fig. 23 for an arbitrary frequency and normal incidence. In the figure, only the first two modes are propagating and the other two are evanescent.

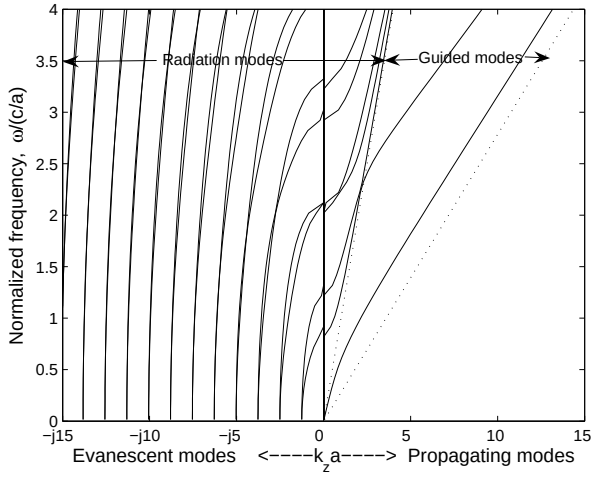

Figure 24: The dispersion of a slab waveguide using planewave expansion.

In Fig. 24, dispersion of an aperiodic slab waveguide is shown. Considering the slab to be a periodic medium with large periodicity (also known as a supercell), all propagating and a few evanescent modes are calculated. The slab is made of GaAs with a refractive index of 3.6 and is placed in air. The slab width is $0.4\mu m$ and is placed in a periodic cell of width $5\mu m$ and 256 planewaves were used for calculation. It gives a clear picture of the modal spectrum that would be further used as basis functions in mode-matching. Though the radiation mode spectrum is continuous, assuming that the coupling occurs to a few discrete radiation modes and all guided modes, the basis functions used for the mode-matching analysis are limited.

3.2.2 Scattering matrix analysis along the out-of-plane direction

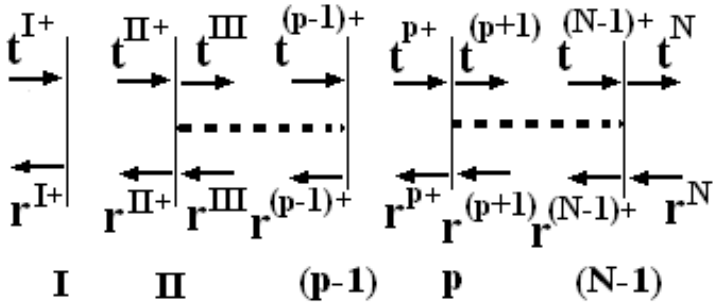

Figure 25: The layer-by-layer scheme of photonic structure for scattering matrix analysis.

The scattering matrix [83, 79, 14, 143, 137] method is a well-known stable method for calculating transmission and reflection at arbitary layer interfaces. The modes in each 2D slice, calculated as described in the previous section is built as a modal matrix composed of eigenvectors using a limited number of lower order planewave coefficients. For example, if N planewaves are used to calculate 2D slice modes, then only n ($<< N$) eigensolutions (modes) are calculated, and $n/2$ planewave coefficients

are used to build the modal matrix in each 2D slice. The modal matrix for a layer is represented as follows [143],

$$M = \begin{bmatrix} E_{Gx}^{(even)+} & E_{Gx}^{(odd)+} & E_{Gx}^{(even)-} & E_{Gx}^{(odd)-} \\ E_{Gy}^{(even)+} & E_{Gy}^{(odd)+} & E_{Gy}^{(even)-} & E_{Gy}^{(odd)-} \\ H_{Gx}^{(even)+} & H_{Gx}^{(odd)+} & H_{Gx}^{(even)-} & H_{Gx}^{(odd)-} \\ H_{Gy}^{(even)+} & H_{Gy}^{(odd)+} & H_{Gy}^{(even)-} & H_{Gy}^{(odd)-} \end{bmatrix} \tag{29}$$

The planewave coefficients of all, even and odd modes are listed along columns using a limited number of planewaves. The + and − superscripts indicate forward and backward propagating modes. The size of the modal matrix is $2n \times 2n$. At any $(p-1)^{th}$ interface, the modal matrix satisfies the following relations,

$$\begin{bmatrix} t^p \\ r^p \end{bmatrix} = M_p^{-1} M_{p-1} \begin{bmatrix} t^{(p-1)+} \\ r^{(p-1)+} \end{bmatrix} = \begin{bmatrix} T_{11}^{p,(p-1)} & T_{12}^{p,(p-1)} \\ T_{21}^{p,(p-1)} & T_{22}^{p,(p-1)} \end{bmatrix} \begin{bmatrix} t^{(p-1)+} \\ r^{(p-1)+} \end{bmatrix} \tag{30}$$

$$\begin{bmatrix} t^{(p-1)+} \\ r^{(p-1)+} \end{bmatrix} = M_{p-1}^{-1} M_p \begin{bmatrix} t^p \\ r^p \end{bmatrix} = \begin{bmatrix} T_{11}^{(p-1),p} & T_{12}^{(p-1),p} \\ T_{21}^{(p-1),p} & T_{22}^{(p-1),p} \end{bmatrix} \begin{bmatrix} t^p \\ r^p \end{bmatrix} \tag{31}$$

where r and t are the amplitudes of forward and backward propagating modes in each layer, as shown in Fig. 25.

It is not necessary to take inner products in real space as it is usually done in real-space based mode-matching methods [152, 11]. Due to orthonormality of planewave basis set, only a modal matrix inversion and multiplication suffices to enforce the mode-matching condition at the interface. However, since the modal matrix is an approximation of the exact modes (in non-uniform layers), it does not have a full rank. So for a stable inversion of the modal matrix, singular value decomposition (svd) was used. From equations 30 and 31, the following expressions can be derived,

$$t^p = (I - T_{12}^{p,(p-1)} T_{21}^{(p-1),p})^{-1} (T_{11}^{p,(p-1)} t^{(p-1)+} + T_{12}^{p,(p-1)} T_{22}^{(p-1),p} r^p) \tag{32}$$

$$r^{(p-1)+} = (I - T_{21}^{(p-1),p} T_{12}^{p,(p-1)})^{-1} (T_{21}^{(p-1),p} T_{11}^{p,(p-1)} t^{(p-1)+} + T_{22}^{(p-1),p} r^p) \tag{33}$$

Let P^p represent propagation matrix [143] in which its diagonal elements are exponential functions representing the propagation of modes. Then $t^{p+} = P^p t^p$ and $r^p = P^p r^{p+}$ and using equations (19), (20) and propagation matrix, the scattering matrix between p^{th} and $(p-1)^{th}$ layers, $S^{(p-1),p}$ is built as follows,

$$S_{11}^{(p-1),p} = P^p(I - T_{12}^{p,(p-1)}T_{21}^{(p-1),p})^{-1}T_{11}^{p,(p-1)} \quad (34)$$

$$S_{12}^{(p-1),p} = P^p(I - T_{12}^{p,(p-1)}T_{21}^{(p-1),p})^{-1}T_{12}^{p,(p-1)}T_{22}^{(p-1),p} \quad (35)$$

$$S_{21}^{(p-1),p} = (I - T_{21}^{(p-1),p}T_{12}^{p,(p-1)})^{-1}T_{21}^{(p-1),p}T_{11}^{p,(p-1)} \quad (36)$$

$$S_{22}^{(p-1),p} = (I - T_{21}^{(p-1),p}T_{12}^{p,(p-1)})^{-1}T_{22}^{(p-1),p} \quad (37)$$

Therefore if,

$$\begin{bmatrix} t^{p+} \\ r^{(p-1)+} \end{bmatrix} = \begin{bmatrix} S_{11}^{(p-1),p} & S_{12}^{(p-1),p} \\ S_{21}^{(p-1),p} & S_{22}^{(p-1),p} \end{bmatrix} \begin{bmatrix} t^{(p-1)+} \\ r^{p+} \end{bmatrix} \quad (38)$$

The scattering matrix representing all p layers can then be derived iteratively as shown in the following steps if the scattering matrix, $S^{1,(p-1)}$ between 1^{st} and $(p-1)^{th}$ layers is known. If,

$$\begin{bmatrix} t^{(p-1)+} \\ r^{I+} \end{bmatrix} = \begin{bmatrix} S_{11}^{1,(p-1)} & S_{12}^{1,(p-1)} \\ S_{21}^{1,(p-1)} & S_{22}^{1,(p-1)} \end{bmatrix} \begin{bmatrix} t^{I+} \\ r^{(p-1)+} \end{bmatrix} \quad (39)$$

then from equations 38 and 39,

$$t^{(p-1)+} = (I - S_{12}^{1,(p-1)}S_{21}^{(p-1),p})^{-1}(S_{11}^{1,(p-1)}t^{I+} + S_{12}^{1,(p-1)}S_{22}^{(p-1),p}r^{p+}) \quad (40)$$

$$r^{(p-1)+} = (I - S_{21}^{(p-1),p}S_{12}^{1,(p-1)})^{-1}(S_{11}^{1,(p-1)}t^{I+} + S_{22}^{(p-1),p}r^{p+}) \quad (41)$$

Using equation 38 and equation 39,

$$\begin{aligned} t^{p+} = {} & S_{11}^{(p-1),p}(I - S_{12}^{1,(p-1)}S_{21}^{(p-1),p})^{-1}S_{11}^{1,(p-1)}t^{I+} + \\ & (S_{11}^{(p-1),p}(I - S_{12}^{1,(p-1)}S_{21}^{(p-1),p})^{-1}S_{12}^{1,(p-1)}S_{22}^{(p-1),p} + S_{12}^{(p-1),p})r^{p+} \end{aligned} \quad (42)$$

$$\begin{aligned} r^{I+} = {} & (S_{21}^{1,(p-1)} + S_{22}^{1,(p-1)}(I - S_{21}^{(p-1),p}S_{12}^{1,(p-1)})^{-1}S_{11}^{1,(p-1)})t^{I+} + \\ & S_{22}^{(p-1),p}(I - S_{21}^{(p-1),p}S_{12}^{1,(p-1)})^{-1}S_{22}^{(p-1),p}r^{p+} \end{aligned} \quad (43)$$

Therefore, if the scattering matrix for $(p-1)$ layers, $S^{1,(p-1)}$ and between $(p-1)^{th}$ and p^{th} interface, $S^{(p-1),p}$ are known, then the scattering matrix for p layers, $S^{1,p}$ can be constructed as [143],

$$S_{11}^{1,p} = S_{11}^{(p-1),p}(I - S_{12}^{1,(p-1)}S_{21}^{(p-1),p})^{-1}S_{11}^{1,(p-1)} \quad (44)$$

$$S_{12}^{1,p} = S_{11}^{(p-1),p}(I - S_{12}^{1,(p-1)}S_{21}^{(p-1),p})^{-1}S_{12}^{1,(p-1)}S_{22}^{(p-1),p} + S_{12}^{(p-1),p} \quad (45)$$

$$S_{21}^{1,p} = S_{21}^{1,(p-1)} + S_{22}^{1,(p-1)}(I - S_{21}^{(p-1),p}S_{12}^{1,(p-1)})^{-1}S_{21}^{(p-1),p}S_{11}^{1,(p-1)} \quad (46)$$

$$S_{22}^{1,p} = S_{22}^{1,(p-1)}(I - S_{21}^{(p-1),p}S_{12}^{1,(p-1)})^{-1}S_{22}^{(p-1),p} \quad (47)$$

For calculating t^p and r^p co-efficients [11], if,

$$\begin{bmatrix} t^p \\ r^{I+} \end{bmatrix} = \begin{bmatrix} S_{11}^b & S_{12}^b \\ S_{21}^b & S_{22}^b \end{bmatrix} \begin{bmatrix} t^{I+} \\ r^p \end{bmatrix}, \qquad \begin{bmatrix} t^N \\ r^p \end{bmatrix} = \begin{bmatrix} S_{11}^f & S_{12}^f \\ S_{21}^f & S_{22}^f \end{bmatrix} \begin{bmatrix} t^p \\ r^N \end{bmatrix} \quad (48)$$

then,

$$t^p = (I - S_{12}^b S_{21}^f)^{-1} S_{11}^b t^I \quad (49)$$

$$r^p = S_{21}^f (I - S_{12}^b S_{21}^f)^{-1} S_{11}^b t^I \quad (50)$$

3.2.3 Round-trip operator

If guided modes formed in the p^{th} layer are to be calculated, then incoming fields, $t^{I+} = r^N = 0$. A round-trip operator representing the forward and backward propagation of mode in the p^{th} layer can be derived as follows,

$$r^p = S_{21}^f t^p \quad (51)$$

$$t^p = S_{12}^b r^p \quad (52)$$

$\Rightarrow$

$$r^p = S_{21}^f S_{12}^b r^p \quad (53)$$

Therefore round-trip operator, $R_{trip} = eig(S_{21}^f S_{12}^b)$. The eigenvalues equal to 1 denote guided mode and eigenvalues less than 1 correspond to leaky modes. It is

easier to search for guided and leaky modes in phase space than magnitude space as in [29]. More details regarding the calculation of $3D$ modes in phase space are presented in the next section.

3.3 Verification

To verify the results of our solver, a scattering problem and a confinement problem are considered. Both problems have already been solved in [32] and [125, 29]. We reproduce the results using our planewave expansion-based eigenmode method for verification purposes.

3.3.1 Scattering problem

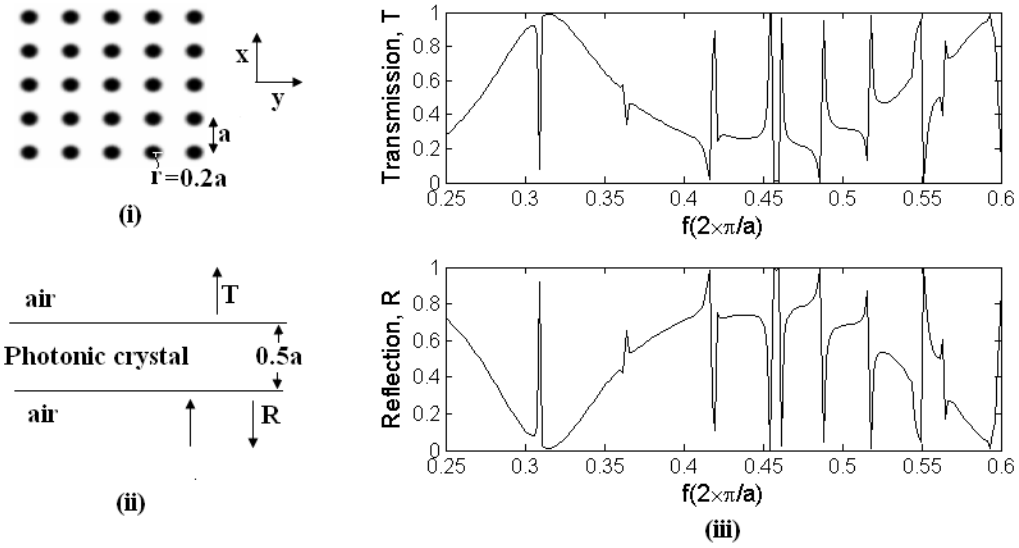

Figure 26: Scattering by a photonic crystal slab with a relative permittivity of 12 and with periodic air-holes arranged in square lattice. The periodicity of holes is a, thickness of the slab is $0.5a$, and the radius of the air holes is $0.2a$.

An s-polarized field in air is scattered by a photonic crystal slab, which has a relative permittivity of 12 with air holes etched in it. The holes have a periodicity of a and thickness of the slab is $0.5a$. The incident field has an in-plane wavevector,

$\vec{k_t} = \hat{x}(0.2 \times 2\pi/a)$.

¿From Fig. 26, the results match with Fig. 7 in [32]. In [32], finite difference method was used for the calculation. In our calculation, $N = 24 \times 24$ planewaves were used to find the eigenmodes and $n = 50$ eigensolutions were used to match modes between layers.

3.3.2 Confinement problem

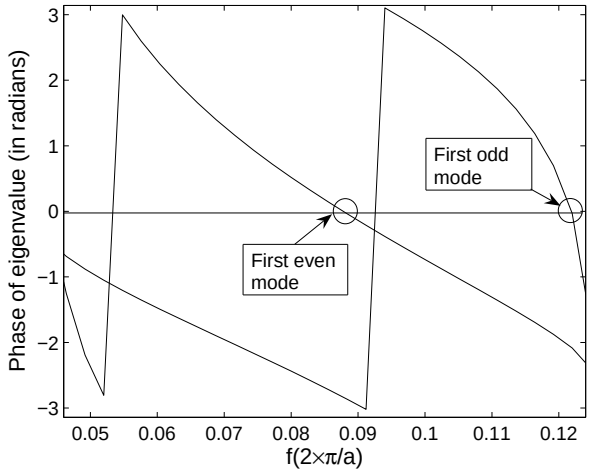

Figure 27: Phase variation of eigenvalues of lossless modes as a function of frequency for a fixed in-plane wavevector, $\vec{k_t} = \hat{x}(0.25 \times \pi/a)$.

The round-trip operator derived in previous section is used to calculate the guided modes in a photonic crystal slab. The results have been presented in [125] and [29]. Instead of magnitude analysis of the eigenvalues as in [29] for finding the modes in photonic crystal slab, a phase analysis of eigenmodes are used. For guided modes, the eigenvalue of the round-trip operator becomes equal to 1, and for leaky-modes, it is less than 1. However in either case the phase of eigenvalues of the round-trip operator corresponding to the photonic crystal slab mode becomes 0. Fig. 27 shows the variation of phase as a function of frequency for a fixed in-plane wavevector of $\vec{k_t} = \hat{x}(0.25 \times \pi/a)$. The phase of the eigenvalues has a smooth variation and, due to

which any root-finding algorithm can easily calculate the modes. However as shown in Fig. 2 of [29], magnitude variation is abrupt and hence frequency must be finely discretized for calculating modes.

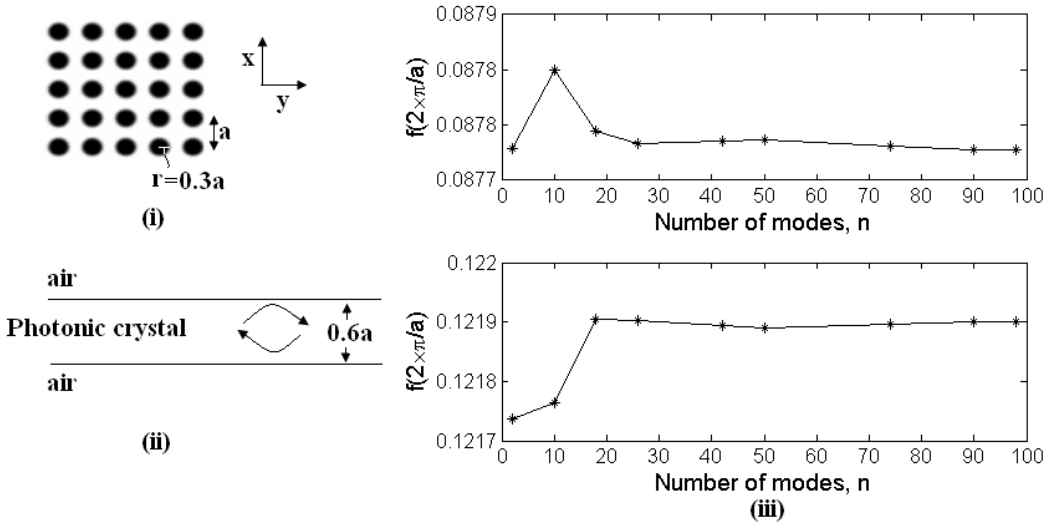

Figure 28: Convergence analysis of first two modes in a photonic crystal slab with refractive index, 3.5 with air holes in it. The air-holes are arranged in square lattice. The thickness of the slab is $0.6a$ with periodicity and radius of air-holes, a and $0.3a$ respectively.

The convergence analysis of first two guided modes as a function of number of modes is shown in Fig. 28. The number of planewaves was fixed at, $N = 24 \times 24$. In [125] and [29], convergence analysis of odd modes are provided and the result matches with that in Fig. 28. The considered photonic crystal slab has a refractive index of 3.5 with air holes etched in it. The periodicity and radius of air-holes are a and $r = 0.3a$ respectively.

3.4 Example problems

In this section, the applicability of planewave expansion for structures with extreme dimensions with respect to the wavelength is examined. Photonic crystals and small

photonic crystal defects have dimensions, comparable to the wavelength of operation. On the other hand, photonic crystal-based VCSELs or photonic crystal fibers are much larger than the wavelength of operation. So, using a photonic crystal slab, small photonic crystal defect slab and a large photonic crystal defect slab as examples, the dependance of mode-matching on the number of basis modes (and the number of planewaves) is shown through convergence analysis. Also, the photonic crystal defect slabs suspended in air may be considered as benchmark structures, because they match an infinitely extended mode in the uniform medium to confined mode in the slab and then again match confined mode to infinitely extended mode in the uniform medium. So if the method can solve for scattering by photonic crystal defect slabs, then it should theoretically be possible for extending it to arbitrary multi-layered photonic crystal structures.

3.4.1 Photonic crystal slab

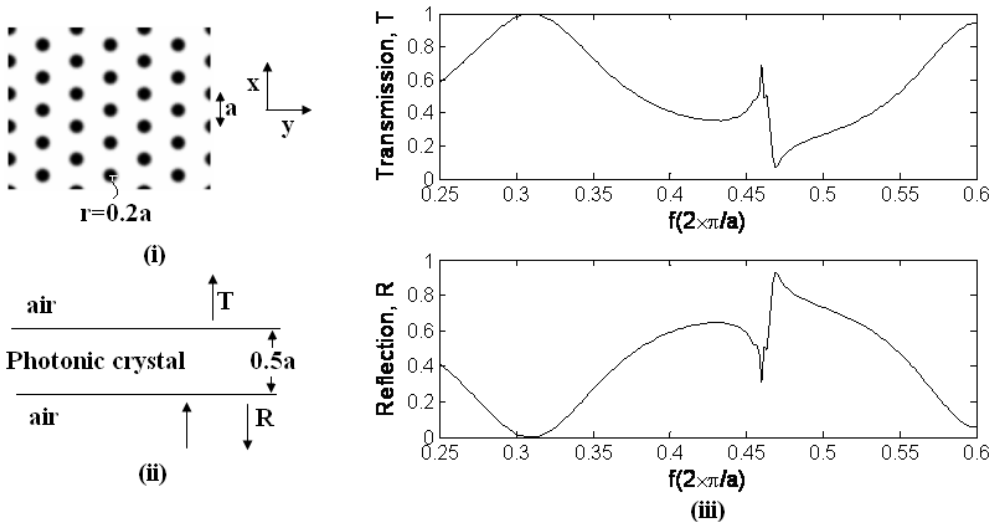

Figure 29: Scattering of s-polarized light by a photonic crystal slab with a relative permittivity of 12 with periodic air-holes arranged in triangle lattice. The periodicity of holes is a, thickness of the slab is $0.5a$ and the radius of the air holes is $0.2a$.

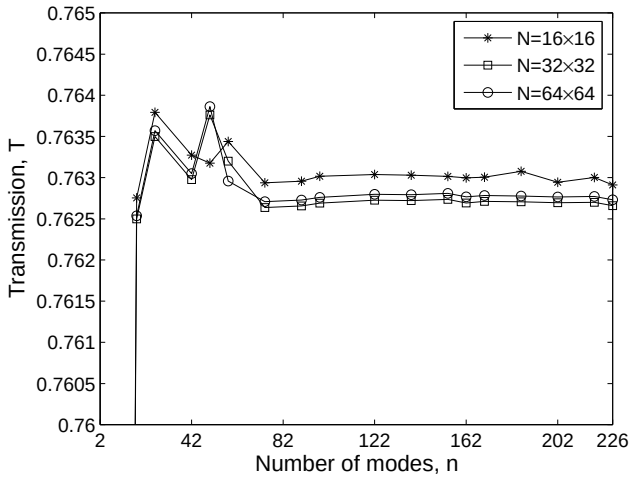

Figure 30: Convergence analysis of transmission of the photonic crystal slab for a normally incident s-polarized field, at a normalized frequency, 0.35. It can be seen that though the number of planewaves for eigenmode expansion is large, the number of modes required for mode-matching is much less.

The transmission spectrum of normally incident s-polarized planewave through a photonic crystal slab with relative permittivity, 12 having air holes arranged in triangular lattice was calculated. The periodicity and radius of air-holes are, a and $0.2a$ respectively, and the thickness of the layer is $0.5a$. As seen in Fig.29, a guided mode resonance can be observed. For the calculation, $N = 16 \times 32$ planewaves for eigenmode expansion and $n = 50$ modes for mode-matching were used. The convergence analysis at a normalized frequency of 0.35 as a function of both number of planewaves for eigenmode calculation and number of modes for mode-matching is presented in Fig. 30.

3.4.2 Small photonic crystal defect slab

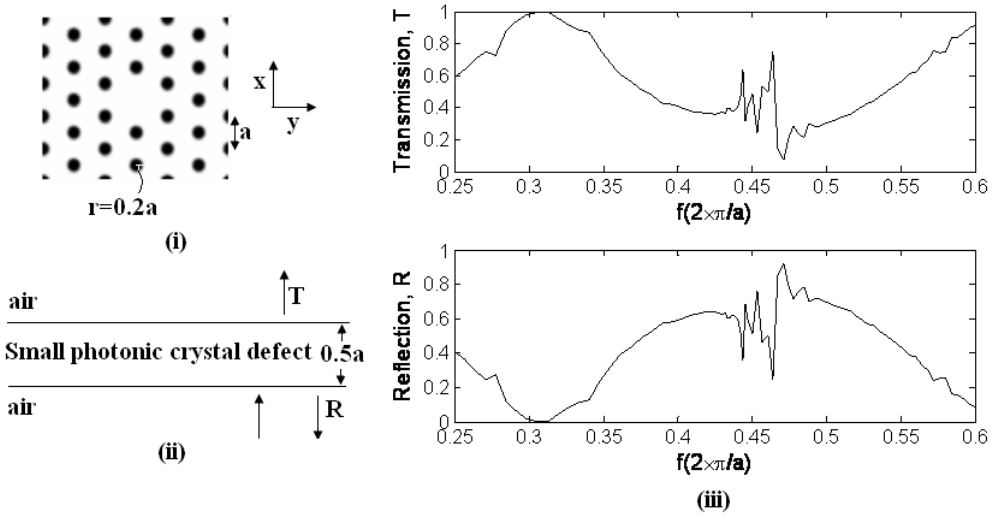

Figure 31: Scattering of normally incident s-polarized light by a single-point small photonic crystal defect slab with a relative permittivity of 12 with periodic air-holes arranged in triangle lattice. The periodicity of holes is a, thickness of the slab is $0.5a$ and the radius of the air holes is $0.2a$.

For these simulations, all structural properties are same as that of the triangular lattice photonic crystal used in previous subsection, and also the normally incident light is s-polarized. The number of planewaves, $N = 36 \times 72$ and number of modes, $n = 226$ modes were used.

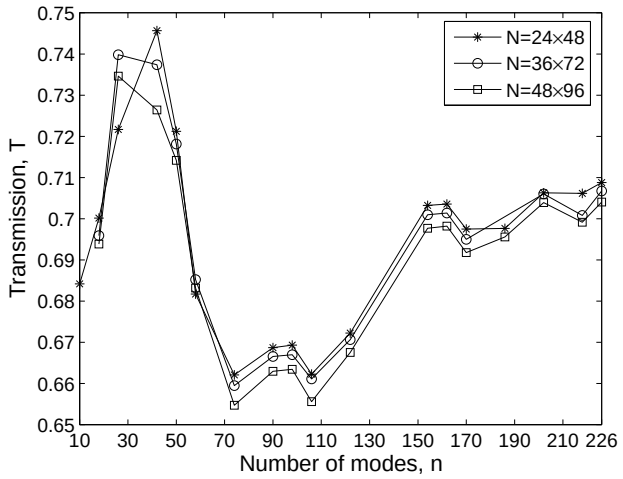

Figure 32: Convergence analysis of transmission of a small photonic crystal defect slab for for normally incident s-polarized field at a normalized frequency, 0.35. Though the convergence is not very stable, it oscillates around a relatively small error.

The missing hole did not greatly alter the transmission spectrum as compared to Fig. 29, except around the guided mode frequency point, where multiple modes associated with the defect appear. The simulation cell size was three times greater on a side than that used for photonic crystal slab. So the number of modes required was also greatly increased to observe the guided mode resonance. The convergence analysis, shown in Fig. 32 is not very stable, though the error indicated by the oscillations is relatively small.

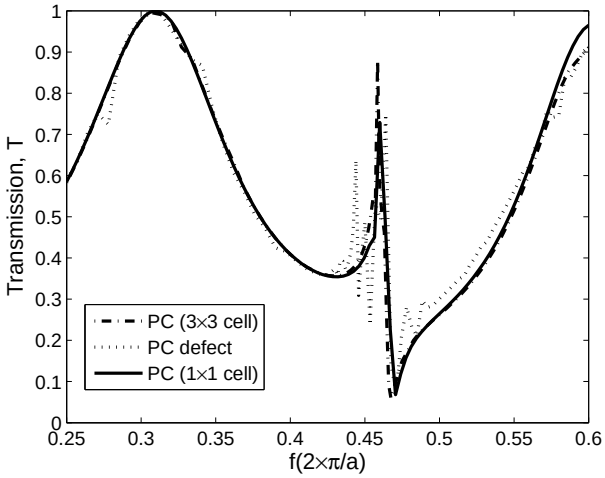

Figure 33: Comparison of transmission of a photonic crystal slab and photonic crystal defect slab with cell size equal to 3×3 periods, when 36×72 planewaves and 236 modes were used.

Since the convergence was not stable, another numerical experiment was performed in order to confirm the results. The defect was removed and a photonic crystal slab with the larger unit cell (but physically identical to the photonic crystal slab from previous section) was simulated using $N = 36 \times 72$ planewaves and $n = 236$ modes. The transmission spectrum with defect, without defect, and without defect, but with the larger unit cell are compared in Fig. 33. The transmission spectrum of the large and single cell photonic crystal slab are in good agreement, as expected. Although the number of modes is greatly increased, note that the number of modes used is much less than the number of planewaves.

3.4.3 Large photonic crystal defect slab

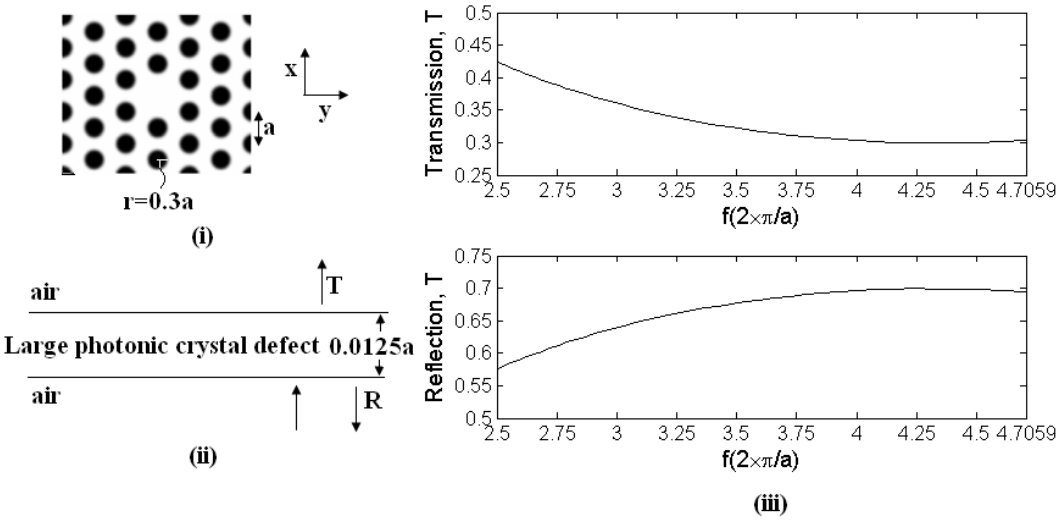

Figure 34: Scattering of s-polarized light by a single-point large photonic crystal defect slab with a relative permittivity of 12, and with periodic air-holes arranged in triangle lattice. The periodicity of holes is a, thickness of the slab is $0.0125a$, and the radius of the air holes is $0.3a$.

A large photonic crystal defect is typically used in photonic crystal defect-based VCSELs [150, 28, 38] and photonic crystal fibers [16, 69]. The size of the structure is large compared to the wavelength of light, due to which all basis modes used for mode-matching analysis are guided. So the structure approximately behaves as a uniform medium. The smooth scattering properties as shown in Fig. 34 confirm the approximate uniform medium behavior of the structure.

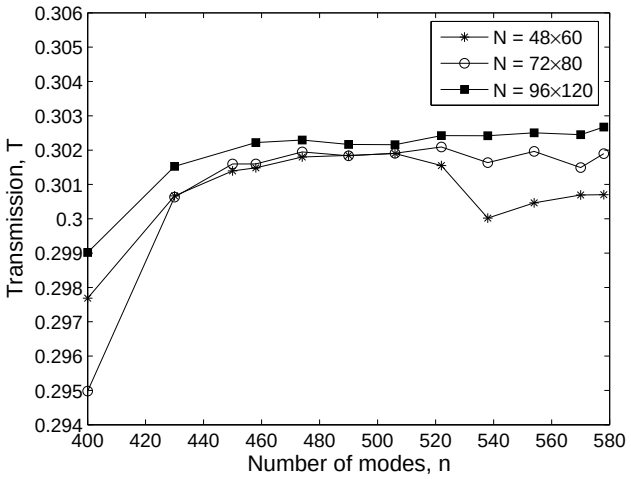

Figure 35: Convergence analysis of transmission of a large photonic crystal defect slab for normally incident s-polarized field at a normalized frequency, 4.0816. The large size of the structure compared to the wavelength of operation yields good convergence property.

Two structural differences compared to the small photonic crystal defect slab are the radius of airholes, $r = 0.3a$ and the thickness of the structure is $0.0125a$ [150, 28, 38]. The incident light is s-polarized, and the direction of incidence is normal to the structure. The calculations were done using, $N = 48 \times 60$ planewaves and $n = 450$ modes. The convergence properties of the structure are good, as shown in Fig. 35. For small number of planewaves ($N = 48 \times 60$), permittivity of the medium is discritized at small number of points (equal to the number of planewaves). So Gibbs phenomenon prevents from achieving stability in the convergence, as the number of modes is increased. However, for large number of planewaves ($N = 96 \times 120$), better stibility in convergence is achieved with the increase in the number of modes.

3.5 Discussion on efficiency

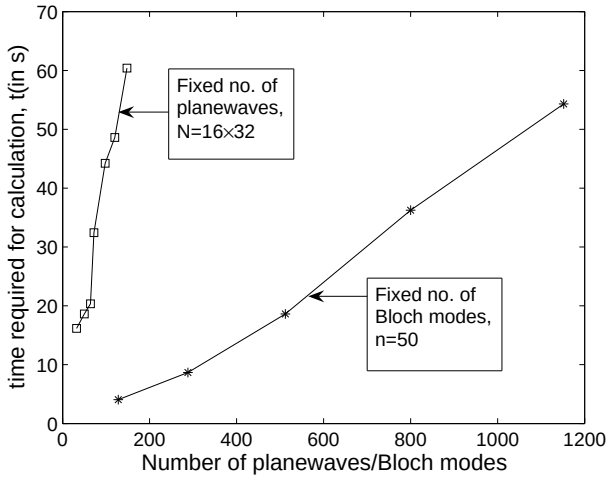

Figure 36: Time scaling as a function of planewaves for fixed number of Bloch modes, and as a function of Bloch modes for a fixed number of planewaves, for the calculation of scattering through a photonic crystal slab.

Two tests are performed to see the time-scaling and memory-scaling of planewave-based eigenmode matching method. In the first test, number of Bloch modes were fixed, and number of planewaves were increased to calculate the transmission through the photonic crystal slab. In the second test, the number of planewaves were fixed, and the number of Bloch modes were increased. Clearly the rate of time scaling is much higher as the number of Bloch modes are increased, as shown in Fig. 36.

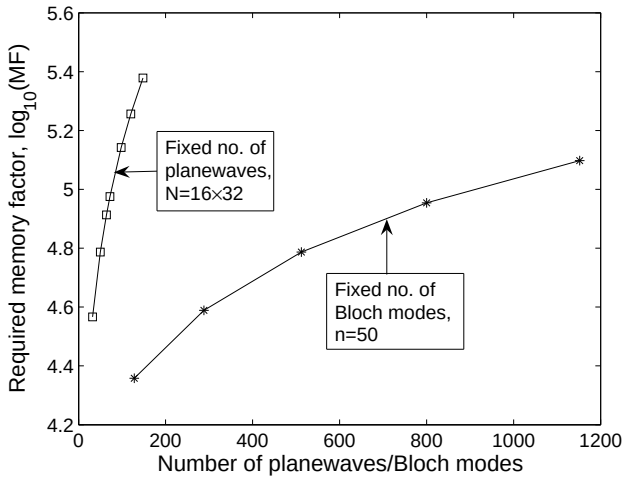

Figure 37: Memory scaling as a function of planewaves for fixed number of Bloch modes, and as a function of Bloch modes for a fixed number of planewaves, for the calculation of scattering through a photonic crystal slab.

To assess the memory scaling, if N represents the number of planewaves and n represents the number of Bloch modes used, then the matrix-free eigenvalue problem requires storage for atleast $2N \times n$ elements and the modal matrix, M in each layer requires storage for atleast, $2n \times 2n$ elements. So a memory factor, $MF = 2N \times n + 2n \times 2n$, which is the minimum storage space required, can be defined. The rate of memory scaling is also much higher as the number of Bloch modes are increased as shown in Fig. 37.

3.6 Conclusions

In this chapter, a complete theory of planewave expansion method for arbitrary photonic structures is reviewed and presented in a memory and speed efficient manner. The theory presented utilizes two main advantages of planewave expansion. They are:

1. The operator can be made matrix-free and uses a Fourier operator directly for the calculation of $2D$ slice modes. Hence the memory requirement is $O(N)$ and

speed achieved is $O(N\log(N))$.

2. Most of the power is concentrated in a few lower order planewaves. So, only a few lower order modes and planewaves are enough for mode-matching analysis unlike in real-space based mode-matching analysis [152, 11], in which entire mode spread is required for inner product calculation in mode-matching analysis.

To show the balance between the number of modes (number of eigensolutions) and the total number of planewaves (total number of grids) used in the calculation, convergence analysis is carried for various example problems. The photonic crystal slab resulted in the expected guided mode resonances. The small photonic crystal defect with sub-micron-scale, that typically has applications in photonic crystal-based components, showed a strong oscillation of transmission spectrum around guided resonance point because of the defect. The large photonic crystal defect layer, that typically has application in photonic crystal fibers, photonic crystal defect-based VCSELs etc., behaved as an uniform medium. So, a smooth transmission spectrum was obtained. Finally, through the convergence analysis, it is shown that compared to the total number of planewaves, the number of modes required for mode-matching analysis is much smaller and hence the method is efficient for many photonic structures.

CHAPTER IV

ROBUST AND OPTIMUM DESIGNS OF NON-LINEARLY TAPERED SLOW LIGHT COUPLERS

This chapter and the next chapter present two applications of the Fourier modal method. In this chapter, extrinsic losses due to fabrication errors in photonic crystal-based waveguides are evaluated and robust design concepts for photonic crystal-based devices are introduced. The chapter closely follows our accepted paper [75].

4.1 Introduction

Slow light waveguides offer superior optical processing capability because they enhance light-material interaction. However, direct coupling of light from a conventional waveguide to a slow light waveguide is known to result in a large impedance mismatch [59, 117]. Various researchers have addressed the problem of coupling of light into slow light waveguides in the form of both, butt coupling [13, 19, 59, 62, 77] and evanescent coupling [6]. Slow light occurs in the flat-band regime of the dispersion of the periodic waveguide, making the scattering losses higher [54]. So a coupler is required to efficiently match the impedance between a conventional waveguide and a periodic waveguide. The most important functionality of the coupler is to ensure that the light enters the coupler in the linear dispersion regime, and as the light propagates, the linear dispersion regime adiabatically transforms into the flat dispersion regime [5] at the periodic waveguide end. The adiabatic variation [59, 62, 117] of the dispersion properties of light in the coupler can either be linear or non-linear.

Various types of coupler are investigated theoretically in both, time-domain [19] and frequency-domain [13, 59, 62, 87] approaches by various research groups. For

example in [59, 54], a simple linear taper is designed and in [62], a non-linearly tapered photonic crystal coupler is designed by varying the profile parameter and searching for an optimum profile. There are many more coupler designs explored in the literature [6, 19, 31, 45, 46, 87, 92, 116, 118, 135, 153]. In all the referred works, the optimal set of parameters that result in best coupling are obtained. However, optimal solutions are often sensitive to fabrication errors [121, 93, 49, 105, 42, 61, 67]. The designed couplers are fabricated using e-beam lithography, since their features have sub-micron dimension, and hence are not free of fabrication errors. The optimum coupling, then may be impossible to achieve in practice.

It is clearly demonstrated in [49] that, extrinsic losses due to fabrication errors are equally important as intrinsic losses in the design of nano-scale devices. So in recent years, the extrinsic losses due to fabrication uncertainties are addressed for photonic crystals. For example in [105] and [42], extrinsic losses in photonic crystal waveguides due to positional and structural uncertainties are compared, between experimental and theoretical results. It is found that near the band edge, reflection losses increases because of random and local shifts of band edges [105]. Below light line, extrinsic losses increases quadratically with disorder parameter [42]. The effect of surface roughness in photonic crystal waveguides is studied in [61]. In [67], both structural and positional uncertainties are considered to model extinction lengths as a function of magnitude of variations. The predicted extinction lengths are matched with experimental results. In [35], the effect of disorder induced radiation losses are investigated. In summary, the design of wavelength-scale devices based on photonic crystals requires accounting for fabrication disorders for real-world applications.

In this work, a planewave-based modal approach [72, 73, 126, 52] is used to assess the coupling properties of the coupler in presence of structural fabrication uncertainties. In addition to finding an optimum solution that results in the best possible coupling, we search for more robust solutions that result in a combination of good

coupling and low transmission uncertainty, in presence of fabrication uncertainties. The robust design, then, meets two criteria. They are:

1. The designed parameters result in good device performance.

2. The variation in the response of the device is minimal with respect to manufacturing/fabrication uncertainties.

Two example structures are considered for the purposes of this paper. They are, a tapered grated coupler and a photonic crystal coupler. Two coupler parameters are considered for the design of periodic couplers: the coupler profile parameter and the length of the coupler. The transmission through the coupler is considered to be the design response. An optimum design of the coupler is first obtained by varying the profile parameter and length of the coupler. The set of parameters for which the transmission is maximized gives the optimum solution for the coupler. To obtain a more robust design of the coupler, a statistical analysis of the device is performed. It is accomplished by introducing random variations with fixed standard deviation to both design variables in each period of the coupler. Different structures are then randomly generated, and tested. After repeating this process many times, the mean and standard deviation of transmission are calculated. The set of design parameters that result in small standard deviation, and simultaneously a large average transmission yields a more robust solution [122, 93] for the coupler.

The simulations presented in this paper are carried out using a 2D planewave-based modal method [72, 73, 126, 52]. In this approach, the device is sliced into layers along the propagation (z) direction. Each layer is uniform along the z direction. Using the planewave expansion technique, the propagating and evanescent modes of each layer are obtained numerically, assuming a periodic supercell in the direction perpendicular to the direction of propagation (x). Following this, a scattering matrix method is used to match modes at the interfaces between the layers, and obtain the

reflection and transmission. More details can be found elsewhere [72, 73, 126, 52]. The simulation domain in each case is terminated with a semi-infinite slow-light waveguide, which is achieved numerically by projecting the fields in the last layer onto the basis set of outgoing Bloch waves. This is done to avoid resonances associated with the finite length of the slow-light waveguide. The boundary condition was tested to verify that adding additional layers to the semi-infinite slow-light waveguide does not affect the transmission.

4.2 Tapered grated coupler

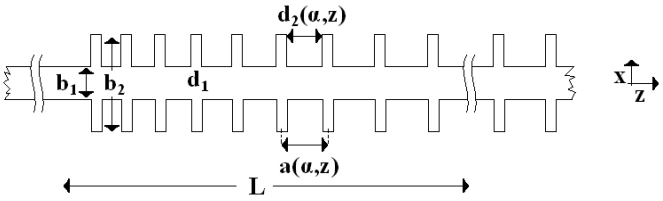

Figure 38: Tapered grated coupler that couples light from a conventional waveguide to a grated waveguide.

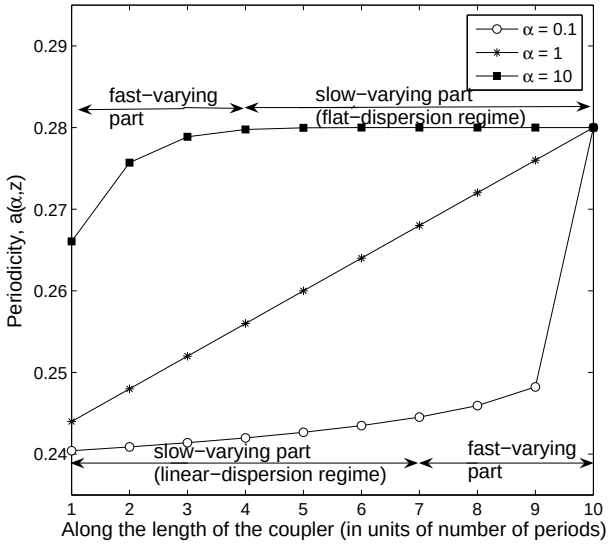

Figure 39: The variation of periodicity as a function of α and number of periods.

Periodic double-grated waveguides may be used for slow light applications [117]. A tapered grated coupler matches the impedances of a grated waveguide and a conventional waveguide adiabatically. The tapered grated coupler is shown in Fig. 38. The parameter $a(\alpha, z) = (d_1 + d_2(\alpha, z))$ represents the periodicity, where d_1 is a constant and $d_2(\alpha, z)$ depends on the profile parameter, α. The periodicity, $a(\alpha, z)$ is a non-linear function given in [62],

$$a(\alpha, z) = a_i + (a_i - a_o)((1 - (z/L))^{\alpha} - 1) \tag{54}$$

where a_i and a_o are periodicities at two ends of the coupler, the parameter α introduces non-linearity in the profile, so that $\alpha = 1$ gives a linear taper, L is the length of the taper in units of integer total number of periods and z is a variable along the length of coupler in integer number of periods. The variation of the periodicity, $a(\alpha, z)$ along the length of coupler for different profile parameters is as shown in Fig. 39.

4.2.1 Dispersion diagram

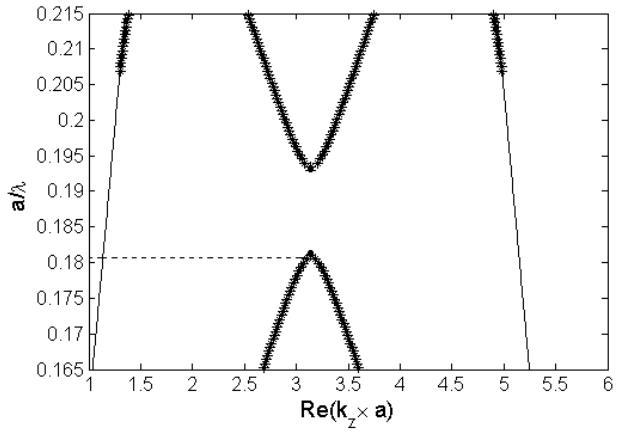

Figure 40: Band diagram of the grated waveguide when $d_1 = 0.07\mu m$, $d_2 = 0.21\mu m$, $b_1 = 0.15\mu m$ and $b_2 = 0.3\mu m$ for TE polarization.

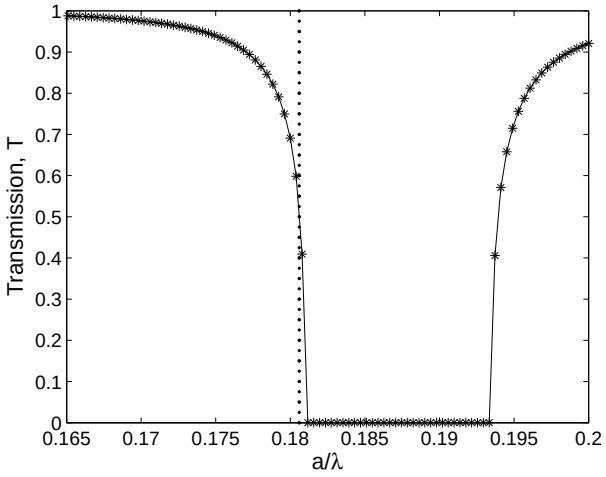

Figure 41: Transmission at the conventional waveguide-grated waveguide interface. The vertical dashed line indicates our chosen slow-light operational frequency.

The dispersion diagram of the double-grated waveguide with a fixed periodicity, a into which the light is transmitted is shown in Fig. 40. It should be noted from Fig. 40 that at the frequency indicated by the dashed line, the grated waveguide exhibits single-mode operation. Transmission goes to zero at the band edge, and for slow waveguide operation, the frequency of interest should be as close as possible to the band edge. However the closer the frequency is to the band edge, the worse the transmission becomes. So a coupler that can match the impedance of the conventional and periodic waveguides is essential. In the absence of a coupler, the transmission into the double grated waveguide from a conventional waveguide is shown in Fig. 41. The vertical dashed line indicates our chosen slow-light operational frequency.

4.2.2 Optimum coupler design

First, it is noted that the wavelength of interest lies in the linear dispersion regime when periodicity, $a = 0.24\mu m$ and it falls in the flat dispersion regime when periodicity, $a = 0.28\mu m$. So the coupler periodicity is varied from $0.24\mu m$ to $0.28\mu m$ non-linearly based on the value of the parameter, α.

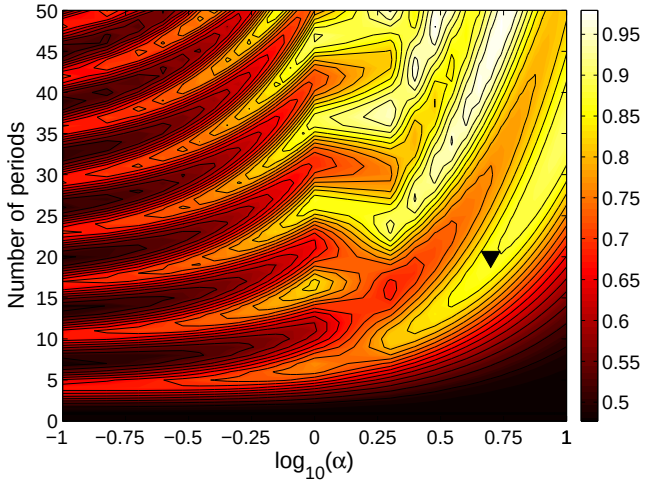

Figure 42: Transmission as a function of the profile parameter α and the length of the coupler L at slow light wavelength. The triangular dot in the plot indicates the optimum design point in the design space for the tapered grated coupler.

One straight forward way of designing a coupler is to search throughout the space of design variables for the best transmission. In this work, the profile parameter, α and the length of the coupler, L in the form of number of periods were considered as design variables. From the dispersion diagram, a normalized frequency of 0.1806 was assumed to be the slow light frequency. The 2D contour plot of transmission at the slow light frequency as function of both variables is plotted in Fig. 42.

It can be seen from Fig. 39 that as the value of α becomes either much larger or much smaller than $\alpha = 1$, the coupler can be split into a fast-varying part and a slow-varying part. When $\alpha << 1$, the slow-varying part is in the linear dispersion regime. Effectively it is a non-adiabatic coupler between a periodic waveguide in the linear dispersion regime and a periodic waveguide in the flat dispersion regime. The result of this is a strongly oscillating variation of transmission as a function of number of periods due to longitudinal resonances in the coupler.

When $\alpha >> 1$, the slow-varying part is in flat dispersion regime, and hence the longitudinal resonances are widely separated. For a large number of periods,

the coupler is adiabatically coupling the conventional waveguide mode to the grated waveguide mode.

The maximum transmission point is then searched for throughout the design space to obtain the optimum solution. The length of the coupler is constained to less than or equal to 20 periods. The optimum design yielded a transmission, $T = 0.8742$ when $\alpha = 5$ with length of the coupler equal to 20 periods.

4.2.3 Robust coupler design

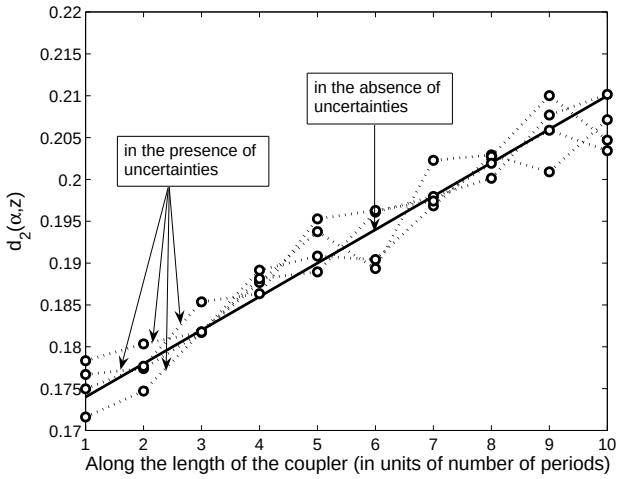

Figure 43: Randomly generated $d_2(\alpha, z)$ is used to generate different structures from which average transmission and standard deviation of transmission are extracted.

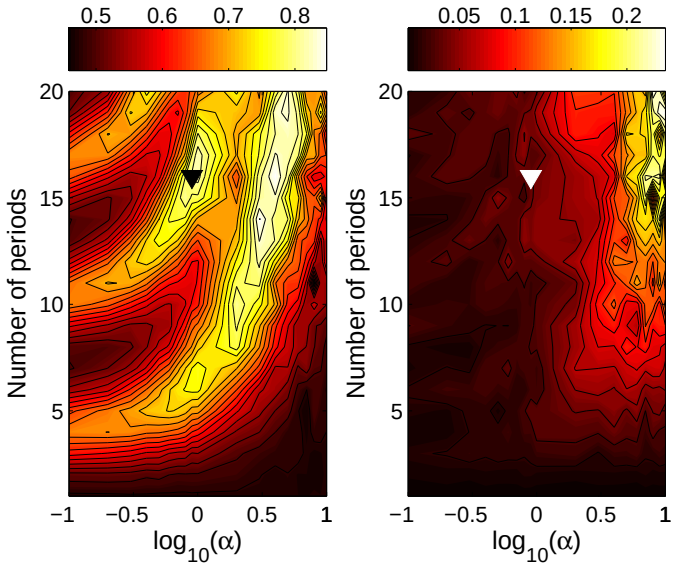

Figure 44: Average transmission (left plot) and standard deviation of transmission as a function of the profile parameter, α and the length of the coupler, L. The triangular dot in the plot indicates a more robust design point in the design space for the tapered grated coupler.

Based on [145], a uniformly distributed uncertainty of 4% ($+/-2\%$) is introduced to both d_1 and $d_2(\alpha, z)$ in each period of the coupler. Transmission through the coupler is calculated as a function of α and L many times for randomly generated $d_2(\alpha, z)$ functions as shown in Fig. 43. The distribution of transmission for each value of α and L gave an average and standard deviation of the transmission. They are shown in Fig. 44 for up to 20 periods of coupler length. The calculations are done using 20 sample structures. Fig. 42 and the average transmission plot in Fig. 44 share certain features. Note that the standard deviation increases with an increase in the number of periods (or length of the coupler) and especially for $\alpha >> 1$, when the coupler has a long slow varying part in the flat dispersion regime. Clearly, uncertainties in the slowly varying part in the flat dispersion regime randomizes the longitudinal resonances causing a high standard deviation. For $\alpha << 1$, the slowly varying part is in the linear dispersion regime, and hence does not lead to much fluctuation in

the transmission, leading to a relatively small increase in the standard deviation with the number of periods. An overall increase in length gradually increases the standard deviation. So adiabatic couplers [59, 117] may not be good for coupling to grated waveguides if the design is prone to manufacturing uncertainties, instead non-adiabatic couplers [87] might be more robust.

To calculate a more robust solution relative to the optimum solution obtained above, the following criteria are used: the standard deviation is constrained to be less than 0.05, the taper length is constrained to be less than or equal to 20 periods, and the maximum average transmission satisfying these constraints is found. A robust design is then obtained to be, $\alpha = 0.8$ with 15 periods. This design has a standard deviation of 0.0208 in the transmission, and an average transmission of 0.8083. For the optimum design solution, the standard deviation is 0.1367, roughly six times that of robust design solution.

Table 2: Robust solutions for tapered grated coupler.

Constraint	Design space		Standard deviation	Average Transmission
	No. of periods	α	σ	T_{avg}
$\sigma < 0.01$	4	0.1	0.0072	0.6800
$\sigma < 0.03$	15	0.8	0.0208	0.8083
$\sigma < 0.05$	17	1	0.0302	0.8225
$\sigma < 0.07$	14	3	0.0577	0.8507

Several solutions corresponding to varying constraints on the standard deviation are given in Table. 2.

4.3 Photonic crystal coupler

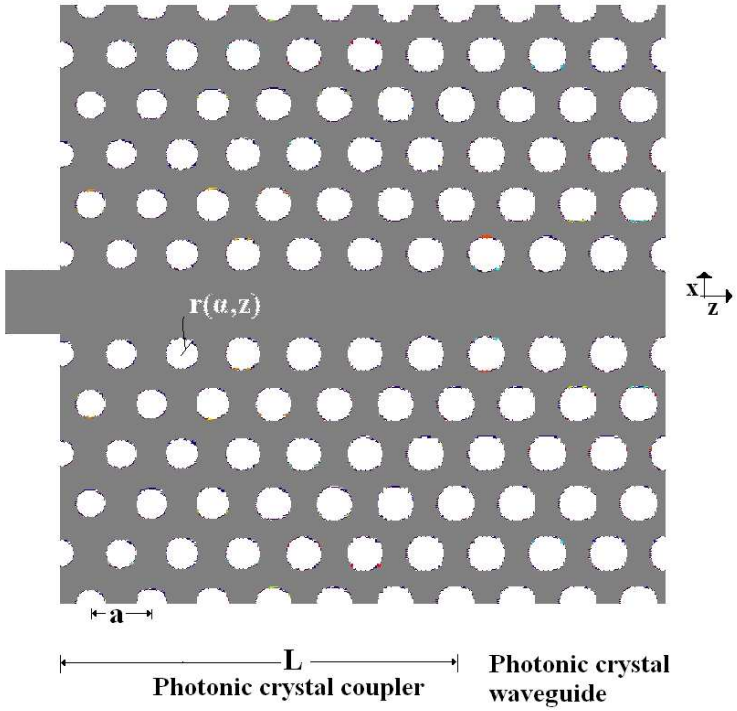

Figure 45: Photonic crystal coupler that couples light from a conventional waveguide to a photonic crystal waveguide.

It is well known that the periodically etched holes in photonic crystal waveguides can be designed to obtain slow light. Again, a tapered photonic crystal coupler is necessary in order to match the impedance of conventional index-guided waveguide modes to band-gap guided photonic crystal defect modes [4]. The photonic crystal considered is a high refractive index medium with air holes in it as shown in Fig. 45. An effective index of the medium is considered to be 2.811 to reduce the problem from 3D to 2D similar to that in [4]. The air hole radius, $r(\alpha, z)$ varies along the length of the coupler, and L is the length of the coupler. The periodicity of the coupler, a is kept constant along the length.

4.3.1 Dispersion diagram

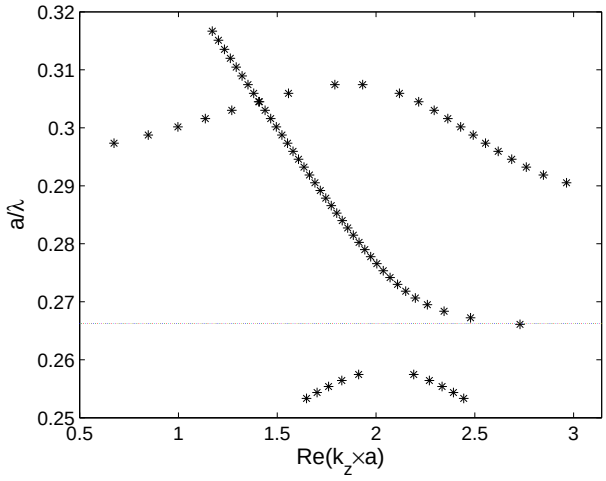

Figure 46: Dispersion diagram of the photonic crystal waveguide with periodicity, a, radius of air-holes, $r = 0.3a$ for TM polarization.

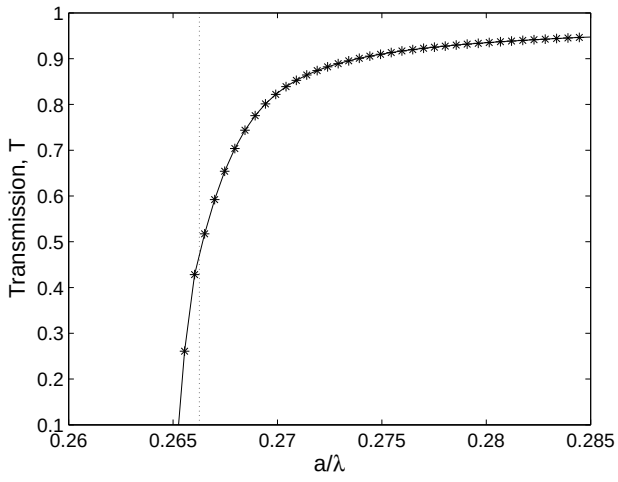

Figure 47: Transmission at the conventional waveguide - photonic crystal waveguide interface.

A defect etched in the crystal gives rise to odd and even band gap guided modes [1]. Photonic crystals can be designed such that within the band gap region, just a single-mode exists [1]. Fig. 46 gives the dispersion relation of the waveguide with a

fixed periodicity, a into which the light is transmitted. Note that at the band edge, the dispersion relation becomes flat indicating the slow light region. The transmission spectrum from a slab waveguide to the photonic crystal waveguide without using a coupler is shown in Fig. 47. A normalized frequency, 0.2663 is considered to be the slow light frequency.

4.3.2 Optimum coupler design

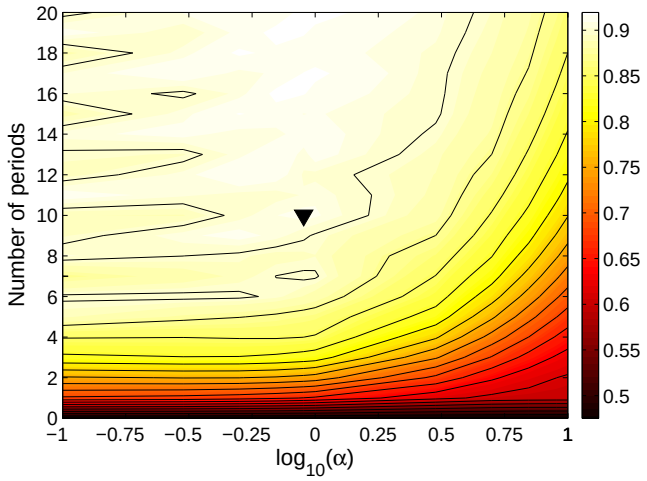

Figure 48: Transmission as a function of the profile parameter α and the length of the photonic crystal coupler L. The triangular dot in the plot indicates the optimum solution in the design space for the photonic crystal coupler.

Similar to the tapered grated coupler design, an optimal parameter search for the best coupling is performed for photonic crystal couplers. It is first found that the slow light frequency lies in the flat band regime for air hole radius of $r = 0.3a$, and the same operating frequency is in the linear dispersion regime for air hole radius of $r = 0.22a$. So in the design of the photonic crystal coupler, the radius of air holes is varied from $0.22a$ to $0.3a$ depending on the profile parameter, α, with the same functional dependence as used for the grated waveguide coupler given above.

The contour plot of transmission at slow light frequency is as shown in Fig. 48.

Unlike the tapered grated waveguide, for all values of α as the number of periods in the periodic coupler is increased, the transmission spectrum around the slow light frequency became sharper, and hence the coupler yielded good transmission properties. When $\alpha << 1$, the slowly varying part in the linear dispersion regime provides a means to match the impedance of the index guided waveguide mode to band guided modes, even with a small number of periods. Since the modes have no escape route laterally due to the photonic bandgap surrounding the waveguide, the transmission becomes larger with an increase in the number of periods. However for $\alpha >> 1$, the required length of the coupler for high transmission will be longer compared to that for $\alpha << 1$, since it has a long slowly varying flat dispersion region.

In general, the photonic crystal coupler showed better transmission characteristics than tapered grated coupler probably because of reduced lateral scattering. For the optimum solution, the length of the coupler is constrained to 10 periods; the maximum transmission point, $T = 0.9121$ occured for $\alpha = 0.9$ and 10 periods.

4.3.3 Robust coupler design

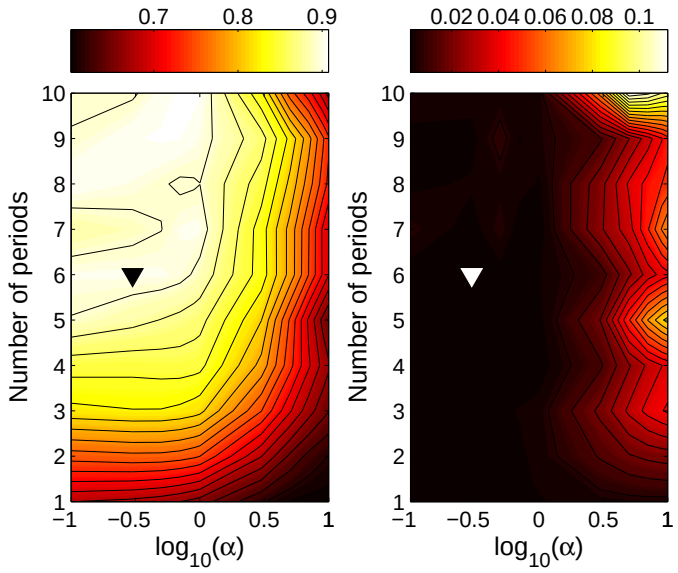

Figure 49: Average transmission (left plot) and standard deviation of transmission as a function of profile parameter α and the length of the photonic crystal coupler L. The trianglular dot in the plot indicates a robust design solution in the design space for the photonic crystal coupler.

Again an uniformly distributed uncertainty of 4% in air hole radius [145] in each period is introduced. The average and standard deviation plots of transmission at the slow light frequency are shown in Fig. 49. For $\alpha << 1$, the effect of uncertainty is negligible, but for $\alpha >> 1$, the uncertainty in the slowly varying flat dispersion region randomizes the mode pattern in the coupler, and hence increases the standard deviation similarly to the tapered grated waveguide. So in order for structure to be more robust to uncertainties, design variables should be again chosen from $\alpha <= 1$.

Also it is noted that photonic crystal couplers are more robust to uncertainties than the tapered grated coupler as demonstrated by the standard deviation plots. With the constraint on the number of periods to be less than or equal to 10, and a constraint on the standard deviation of less than 0.002, a robust design is obtained

to be $\alpha = 0.3$ with 6 periods, and it gives an average transmission of $T = 0.9027$ and a standard deviation of 0.0015. The optimum design had a standard deviation of 0.0036.

Table 3: Robust design solutions for photonic crystal coupler.

Constraint	Design space		Standard deviation	Average Transmission
	No. of periods	α	σ	T_{avg}
$\sigma < 0.002$	6	0.3	0.0015	0.9027
$\sigma < 0.004$	8	0.1	0.0029	0.9071
$\sigma < 0.006$	10	0.7	0.0053	0.9086

Several solutions corresponding to varying constraints on the standard deviation are given in Table. 3.

4.4 Conclusion

In this work, two design methodologies for periodic couplers are presented. The optimum design methodology is to search for parameters in the design space, that yield the best performance of the coupler. This design methodology is commonly used, and assumes that the designed structure is free of any fabrication errors. On the other hand, a robust design is a point in the design space that yields coupler parameters which perform well even in presence of uncertainties. For both couplers studied, the impact of uncertainty on the transmission increases with an increase in length of the slowly-varying region in the flat dispersion regime. So both couplers performed well for $\alpha <= 1$. The optimum design of tapered grated coupler required 20 periods and showed a standard deviation of 0.1357 and a transmission, $T = 0.8742$ for $\alpha = 5$, but the robust design required 15 periods and showed a standard deviation of 0.0208 and an average transmission, $T = 0.8083$ for $\alpha = 0.8$. On the other hand, the optimum design of photonic crystal coupler required 10 periods and had a standard deviation,

0.0036 and transmission, $T = 0.9121$ for $\alpha = 0.8$, but the robust design required 6 periods and had a standard deviation, 0.0015 with an average transmission, 0.9027 for $\alpha = 0.3$. In summary, a short coupler with long slowly-varying region in the linear dispersion regime is more robust to uncertainties. Any photonic crystal-based device can be considered to have a flat dispersion regime and a linear dispersion regime. So the design concept may be extended to any photonic crystal based device.

CHAPTER V

MODAL DISCRIMINATION PROPERTIES OF PHOTONIC CRYSTAL DEFECT DBRS

5.1 Introduction

VCSELs are attractive light sources for many applications, due to their circular output beam and their ease of integration. It is common for VCSELs to incorporate a current aperture in order to keep the current flow away from the surface of the device, and sometimes an optical aperture in order to confine the optical mode in the in-plane direction. Multi-mode VCSELs have a large aperture and therefore can produce high output power, as the current density is low even for high injection levels, thus reducing ohmic heating and thermal rollover. Multi-mode VCSELs also have a broad spectral output and wide beam divergence, which can result in significant pulse broadening in optical networks. One solution is to use single-mode VCSELs. Single-mode VCSELs require a small aperture, which increases the electrical resistance [150] of the device. In order to achieve single-mode operation, modal discrimination in VCSELs can be increased by increasing the losses of higher order modes [89, 154]. Modal discrimination can be accomplished either by using an etched surface relief on the top mirror [89] such that the reflectivity of higher order modes is reduced, or through the use of antiguided VCSELs [154] in which the fundamental leaky mode lases while other higher order modes experience higher radiative losses. The disadvantage of introducing a surface relief is that even the fundamental mode can experience increased scattering loss if the oxide aperture is not in careful alignment with the etched surface. On the other hand, antiguided VCSELs [154] require higher threshold currents, and exhibit poor side mode suppression ratio (SMSR).

Another proposed design for realizing single-mode high-power VCSELs is to etch photonic crystal patterning in the upper DBR mirror [150, 39, 80, 82, 26]. The photonic crystal hole size, placement and shape provide several degrees of freedom for tuning the transverse modal properties [97, 28, 104, 103, 25]. In ref. [39], a photonic crystal defect-based VCSEL was demonstrated to achieve 7mW of nearly single-mode output power with a threshold current of 5 mA and a SMSR of 40 dB. The referred works use either a photonic crystal holey defect or a triangular defect for transverse mode confinement. However, these two structures were not compared with each other or with conventional VCSELs to determine the impact of photonic crystal defect-based DBRs. Therefore, in this research work, the modal discrimination properties of various photonic crystal defect-based DBRs are studied and are compared with conventional DBRs. Rather than performing a full 3D simulation of a photonic crystal defect-based VCSEL [97, 28, 104, 103, 25], only photonic crystal defect-based DBRs are studied. This approach avoids considerable numerical effort and isolates the modal discrimination properties of the photonic crystal-based DBRs. The Fourier modal method analysis of the DBR yields the resonant wavelength at which the DBR is tuned to minimize the phase shift upon reflection from the DBR, as well as the magnitude of the reflection of both the fundamental and the first order modes.

Three kinds of photonic crystal patterning are simulated for modal discrimination analysis. They are:

1. Holey photonic crystal defect: this structure has exhibited endlessly single-mode operation [16].

2. Quadrilateral holey defect: this structure provides high index contrast confinement for modes.

3. Bragg waveguide type defect: this structure provides a weak band gap effect for confinement of modes.

5.2 Numerical experiment set-up

For complete $3D$ simulation of photonic crystal defect-based VCSELs, the Fourier modal method (planewave expansion-based scattering matrix analysis) approach demands a large number of modes and planewaves, since the structure is large compared to the wavelength of light. As it is shown in [74, 73], the mode-matching analysis requires an expansion of the modes of one layer on the basis set of modes of the adjacent layer, and vice-versa. If we classify the layers as 'uniform layers' (where the refractive index doesn't vary in the in-plane directions) and 'non-uniform layers' (where the refractive index varies in the in-plane directions), it proves to be numerically easy to use the uniform layer modes as a basis set to expand the non-uniform layer modes (because uniform layer modes are planewaves), but difficult to use the non-uniform layer modes to expand the uniform medium layer modes, unless a large number of non-uniform layer modes are considered. This is because the uniform layer modes are infinitely extended planewaves and the non-uniform layer modes (in the structures that we consider) are spatially confined modes. One way to mitigate this problem may be to use lateral perfectly matched layer (PML) boundaries so that the modes in all of the layers appear confined [11, 28], but this has not been implemented here. Therefore, a complete $3D$ simulation of a photonic crystal defect-based VCSEL using the Fourier modal method would be computationally intensive and slow.

However, since our interest is to study the modal discrimination properties of various photonic crystal defect structures, we set up the problem such that the approximate first and second photonic crystal defect VCSEL modes are launched at the photonic crystal defect DBR from the bottom layer, and the scattering properties of the multi-layered photonic crystal defect DBR are then analyzed. The experiment requires a comparatively small number of modes, since all of the internal layers are photonic crystal defect layers (non-uniform layers) with similar modal patterns, and only the last layer is air representing the open boundary. Note that even though the

last layer is uniform, there is only an outgoing field in that layer, and therefore the confined modes in the adjacent non-uniform layer do not have to be used to expand the uniform (air) layer modes. So, instead of full $3D$ simulation of a photonic crystal defect-based VCSEL structure, we isolate the modal discrimination properties of the photonic crystal defect DBR with greatly reduced numerical effort.

Two properties are of interest: the fundamental and first order modal resonant wavelengths of the photonic crystal DBR, and the magnitude of the reflection of the fundamental and first order modes at their respective resonant wavelengths. The latter property represents the out-of-plane losses of the fundamental and first order modes in a VCSEL, and the former property is related to the VCSEL resonant wavelength separation. The resonant wavelength of the entire VCSEL cavity will not precisely match the resonant wavelength of the photonic crystal DBR alone, but we expect the difference between the two to be relatively small in a well-designed cavity.

If t represents the vector containing the planewave amplitudes of the incident modal field in the bottom layer, and r represents the vector containing the planewave amplitudes of the reflected modal fields, then a factor referred to as the reflected-incident inner product κ is defined to calculate the amplitude and phase of the reflected field from the photonic crystal defect-based DBR which returns in the incident mode pattern.

$$\kappa = Real\{\frac{< r|t >}{< t|t >}\} \tag{55}$$

The parameter $\frac{<r|t>}{<t|t>}$ is a complex number with absolute value less than or equal to 1. After launching either the fundamental or the first order mode as the incident field from beneath the DBR , the wavelength is tuned using a root-finding algorithm to find the wavelength for which the reflected field is in phase with the incident field. When this is achieved, the imaginary part of the parameter $\frac{<r|t>}{<t|t>}$ goes to 0. This wavelength is considered to be the resonant wavelength of the corresponding mode of the DBR. Resonant wavelengths for both fundamental and first order modes are

calculated using this technique.

In a VCSEL, the total optical losses from the cavity may be split into two types of optical loss: the in-plane modal losses and the out-of-plane diffraction losses. One disadvantage of the Fourier modal method is that it does not account for in-plane losses, because a periodic boundary condition [74, 73] is imposed in the in-plane directions. It has already been demonstrated in ref. [142], that higher-order modes have higher in-plane losses compared to the fundamental mode, although the difference is small. Because it neglects in-plane losses, the Fourier modal method will certainly underestimate the modal discrimination of photonic crystal defect-based DBRs. In this research work, with the assumption that in-plane modal losses are very small [142] and are not changing the modal shape, only the effect of out-of-plane diffraction losses are calculated, and are compared with the oxide-DBR combination used in conventional VCSELs.

5.3 Results

5.3.1 Oxide layer and DBR

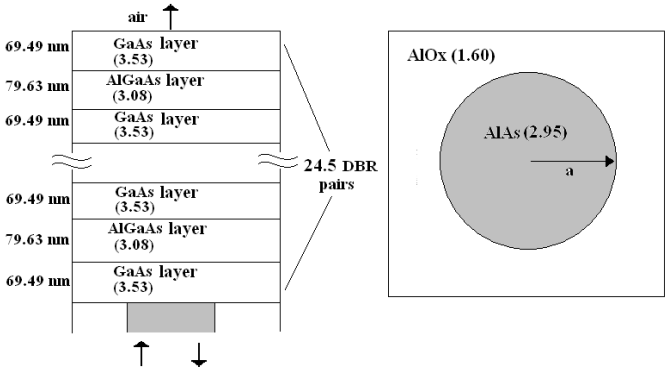

Figure 50: The oxide layer and DBR with 24.5 pairs of alternating layers of GaAs (with refractive index 3.53) and AlGaAs (with refractive index 3.08) with air holes. The right plot shows the cross section of the oxide layer.

A freely available electromagnetics modeling software, CAvity Modeling FRamework (CAMFR) [14] is used to calculate the reflection, transmission, and diffraction caused by a conventional DBR and oxide aperture combination. The structure is shown in Fig. 50.

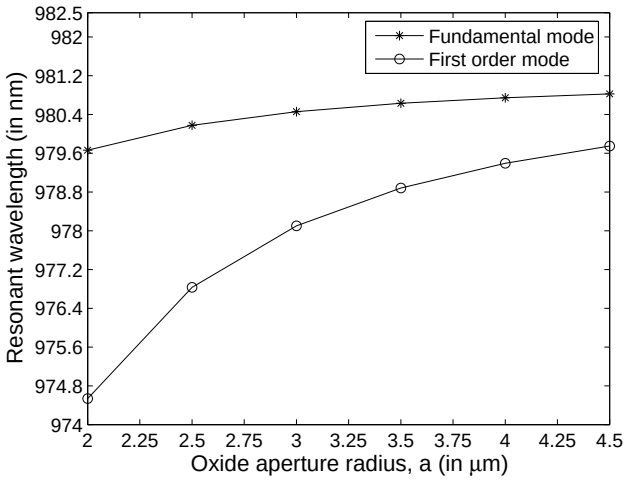

Figure 51: The variation of the resonant wavelengths of the fundamental and first order modes as a function of the radius of oxide aperture.

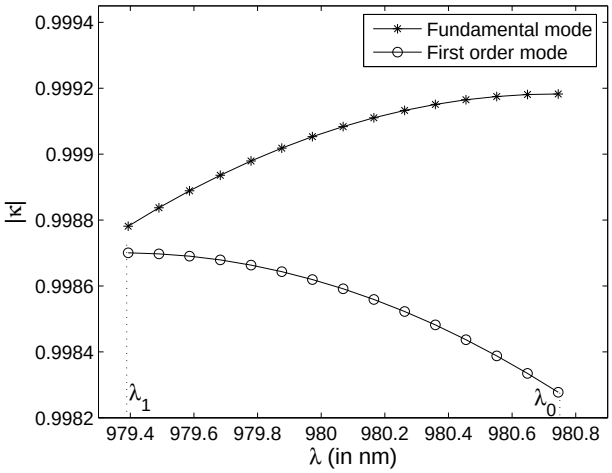

Figure 52: The variation of the magnitude of the reflected-incident inner product $|\kappa|$ for fundamental and first order modes of an oxide aperture/DBR combination as a function of wavelength, for the oxide aperture diameter of $8\mu m$. The endpoints are the resonant wavelengths of the two modes.

The resonant wavelength is shown in Fig. 51 for varying oxide aperture radius. The reflected-incident inner product parameter $|\kappa|$ is shown in Fig. 52 for a fixed oxide aperture diameter of $8\mu m$. The figures clearly show higher separation of resonant wavelengths for smaller aperture radius, and higher diffraction losses for the first order mode compared to the fundamental mode.

5.3.2 Holey photonic crystal defect-based DBRs

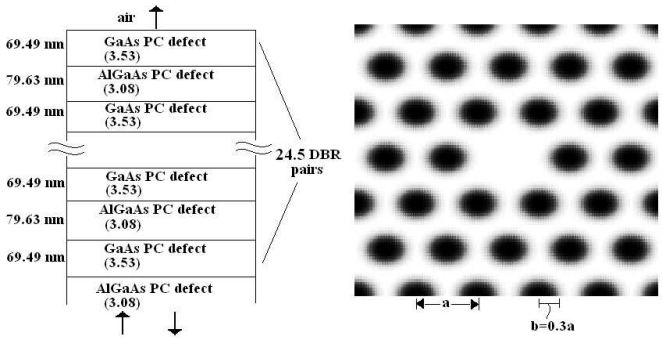

Figure 53: The photonic crystal defect-based DBR has 25 pairs of alternating layers of AlGaAs (with refractive index 3.08) and GaAs (with refractive index 3.53) with air holes. The right plot shows the photonic crystal defect pattern.

The multi-layered circular holey photonic crystal defect structure shown in Fig. 53, which has already been investigated in VCSELs [150, 80, 28, 103] is the first photonic crystal structure simulated. It is simulated using the Fourier modal code described in this thesis.

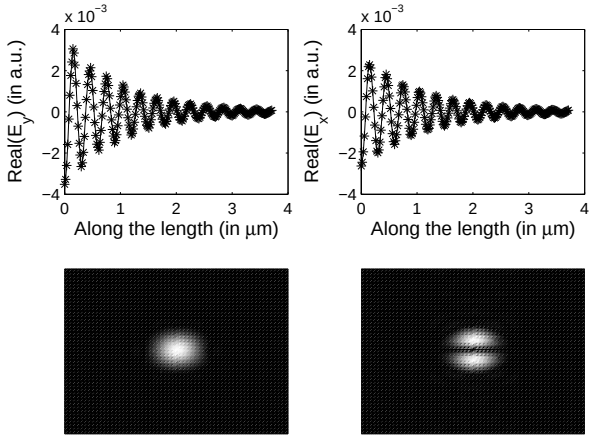

Figure 54: The real part of electric field pattern along the out-of-plane direction, and the in-plane intensity patterns of the fundamental and first-order modes of the holey photonic crystal defect-based DBR.

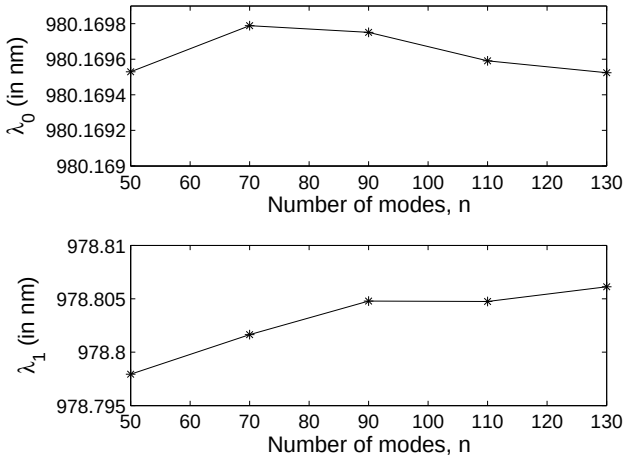

Figure 55: The convergence analysis of the resonant wavelengths of the fundamental (λ_0) and first order (λ_1) modes in the holey photonic crystal defect-based DBR.

Fig. 54 confirms the continuity of fields at layer interfaces and the intensity patterns of the fundamental and first-order modes. An inner product of reflected fields with the incident fields (reflected-incident field vectors inner product) κ is calculated, and simultaneously the wavelength is tuned using a root-finding algorithm to obtain the resonant wavelengths. A convergence analysis of the resonant wavelength calculations is carried out in order to confirm the results, and is shown in Fig. 55.

The resonant wavelength shows good convergence with as few as 50 modes, because there is little scattering into higher-order modes at the interfaces between adjacent layers, as the index contrast between the adjacent layers is small. Next, the structural properties of the photonic crystal defect-based DBRs are varied and the variation of resonant wavelengths is shown in Fig. 56.

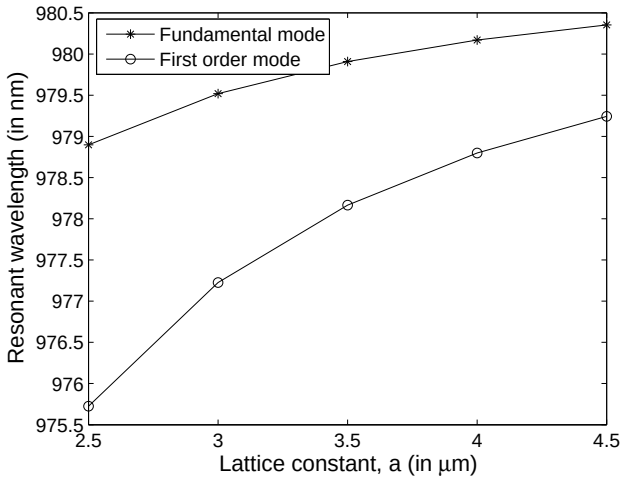

Figure 56: The variation of resonant wavelengths of the fundamental and first order modes as a function of lattice constant in the holey photonic crystal defect-based DBR.

The Fig. 56 shows the variation of resonant wavelengths as a function of lattice constant. A smaller lattice constant results in a smaller defect cavity, and the wavelength separation between the fundamental and first order modes will increase. The trend is similar to that observed in [25], and the modal wavelength separation values are comparable to that in [28].

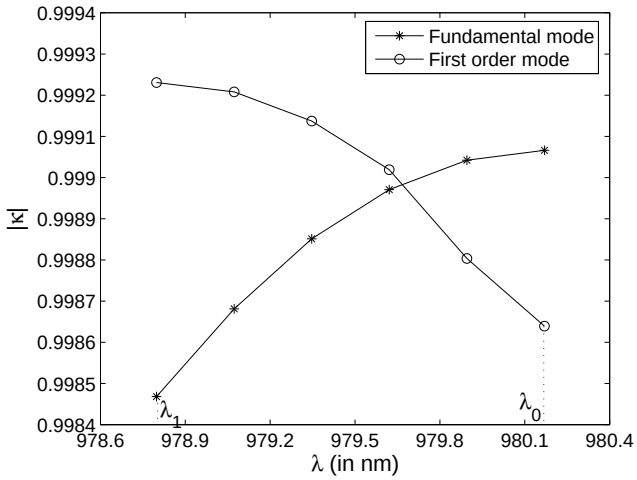

Figure 57: The variation of the magnitude of the reflected-incident inner product $|\kappa|$ for fundamental and first order modes of the holey photonic crystal defect-based DBR between their respective resonant wavelengths for a fixed lattice constant, $a = 4\mu m$.

Next, the magnitude of the reflected-incident fields inner product, $|\kappa|$ is plotted for fundamental and first order modes versus wavelength to calculate the amount of useful reflected fields in the relevant wavelength range for a fixed lattice constant, $a = 4\mu m$. The result is shown in Fig. 57. Interestingly, the reflected-incident fields inner products of the fundamental and first order modes cross in this case, so that the first order mode will have a higher effective reflection at its resonant wavelength. This indicates that diffraction of the first order mode is inhibited by the in-plane confinement offered by holes around the defect. Based on this information, the higher threshold gain requirement for higher order modes in [28] may stem from the higher in-plane modal losses (which are not considered in this work).

5.3.3 Quadrilateral holey photonic crystal defect-based DBR

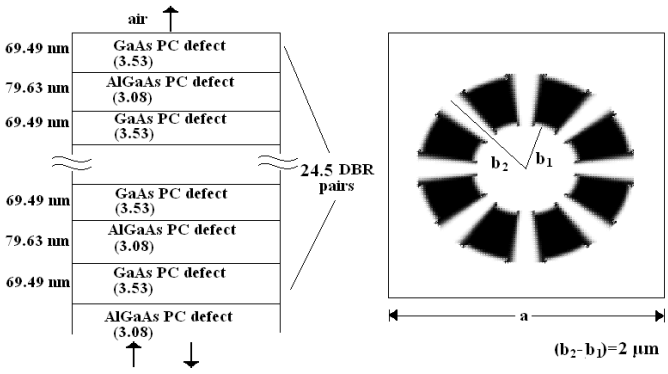

Figure 58: The photonic crystal defect based-DBR shown here has 24.5 pairs of alternating layers of GaAs (with refractive index 3.53) and AlGaAs (with refractive index 3.08) with quadrilateral air holes. The right plot shows the in-plane photonic crystal defect pattern.

In conventional oxide confined VCSELs, an oxide aperture in one or more layers provides modal confinement. The quadrilateral air holes as shown in Fig. 58 should similarly provide a high index contrast confinement of modes. We expect the performance to be similar to that of the triangular hole defects in [39].

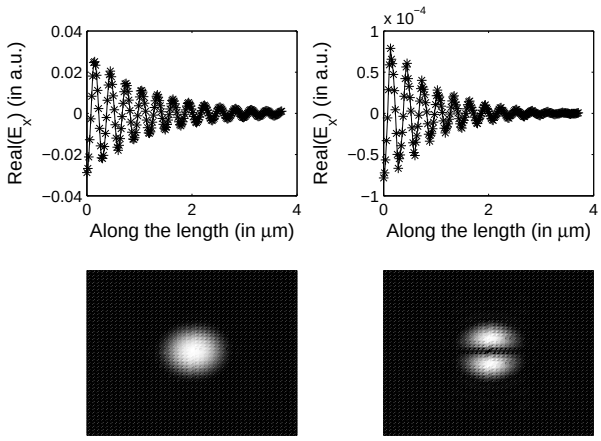

Figure 59: The real part of electric field pattern along the longitudinal direction and the in-plane intensity pattern of the fundamental and first-order modes of the quadrilateral holey defect-based DBR.

The electric field along the longitudinal direction and the in-plane intensity pattern of both fundamental and first order modes are shown in Fig. 59.

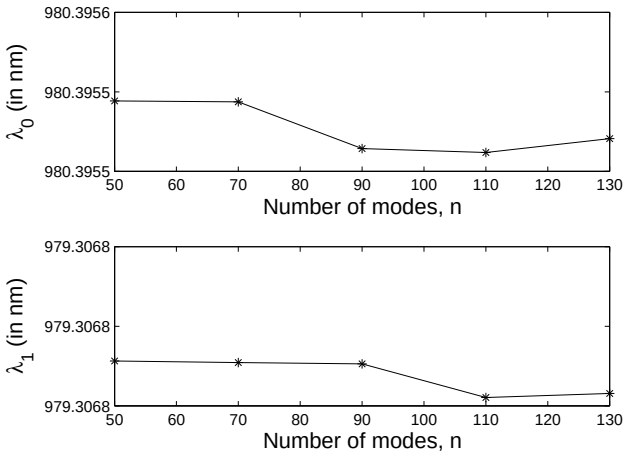

Figure 60: The convergence analysis of the resonant wavelengths of the fundamental (λ_0) and first order (λ_1) modes in the quadrilateral holey defect-based DBR.

The convergence analysis of the resonant wavelengths of the fundamental and first

order modes are shown in Fig. 60.

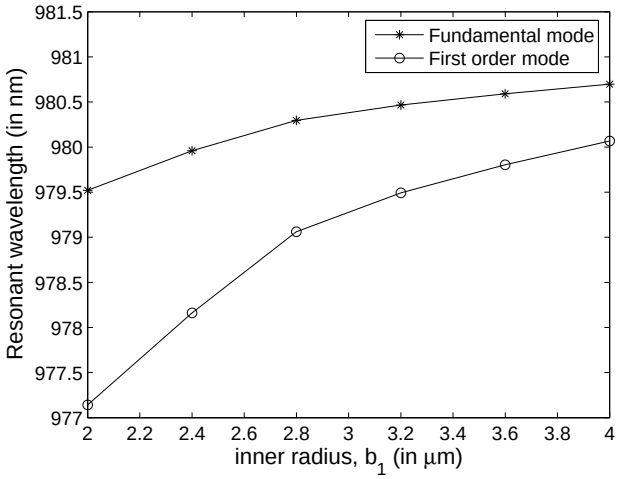

Figure 61: The variation of the resonant wavelengths of the fundamental and first order modes of the quadrilateral holey defect-based DBR as a function of the inner defect radius.

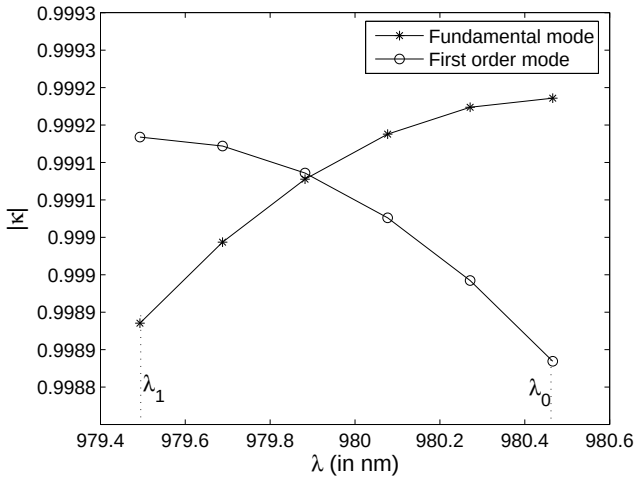

Figure 62: The variation of the magnitude of the reflected-incident field inner product parameter, $|\kappa|$ versus wavelength in the wavelength range between the resonant wavelength of the fundamental mode and the first order mode of the quadrilateral holey defect-based DBR for a fixed inner radius of $b_1 = 3.5\mu m$.

The inner radius b_1 of the central defect of the photonic crystal is varied and the resonant wavelengths are plotted in Fig. 61. The strong modal confinement offered by the holes results in higher out-of-plane diffraction losses for higher order modes as shown in Fig. 62 for a fixed inner radius of $b_1 = 3.5\mu m$.

5.3.4 Bragg waveguide type photonic crystal defect-based DBR

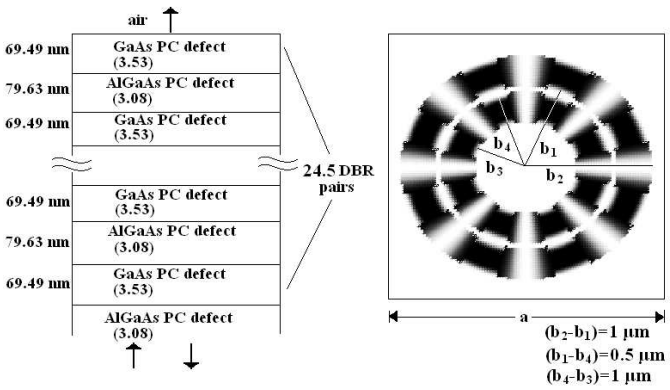

Figure 63: The photonic crystal defect-based DBR shown here has 25 pairs of alternating layers of AlGaAs (with refractive index 3.08) and GaAs (with refractive index 3.53) with Bragg waveguide type holes. The right plot shows the in-plane photonic crystal defect pattern.

In the previous sub-section, the intention of quadrilateral holes is to provide a high index contrast for strong in-plane confinement of modes and simltaneously cause scattering into higher order modes. Now two such holes are placed as shown in Fig. 63 to provide a lateral Bragg mirror effect for the confinement of modes.

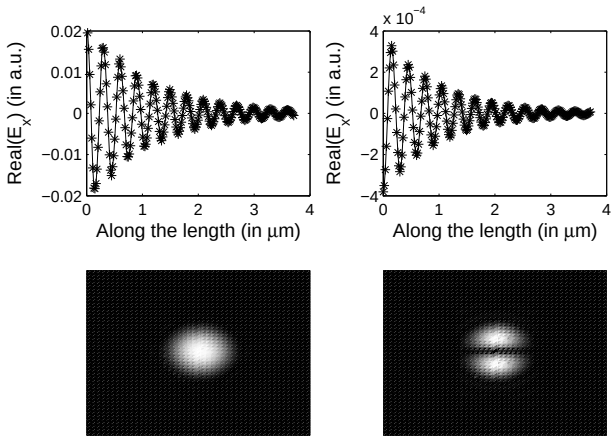

Figure 64: The real part of electric field pattern along the longitudinal direction and the in-plane intensity patterns of the fundamental and first-order modes of the Bragg type defect-based DBR.

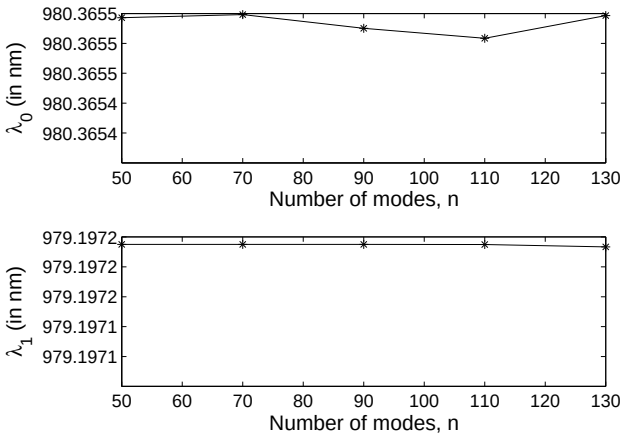

Figure 65: The convergence analysis of the resonant wavelengths of the fundamental (λ_0) and first order (λ_1) modes of the Bragg type defect-based DBR.

The field plots and the convergence analysis of the fundamental and first order modes are shown in Figs. 64 and 65.

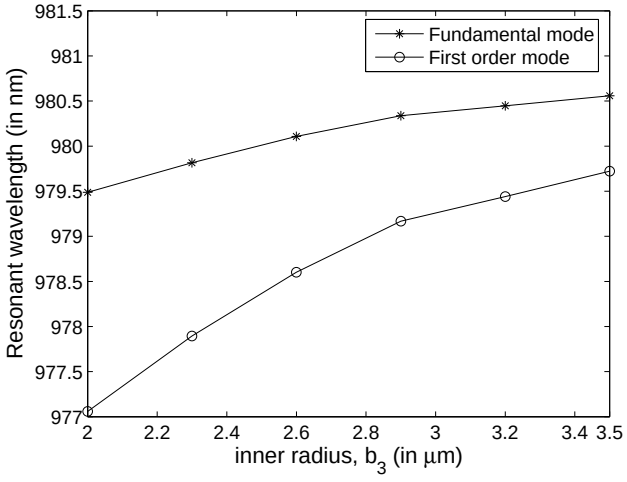

Figure 66: The variation of the resonant wavelengths of the fundamental and first order modes of the Bragg type defect-based DBR as a function of inner defect radius.

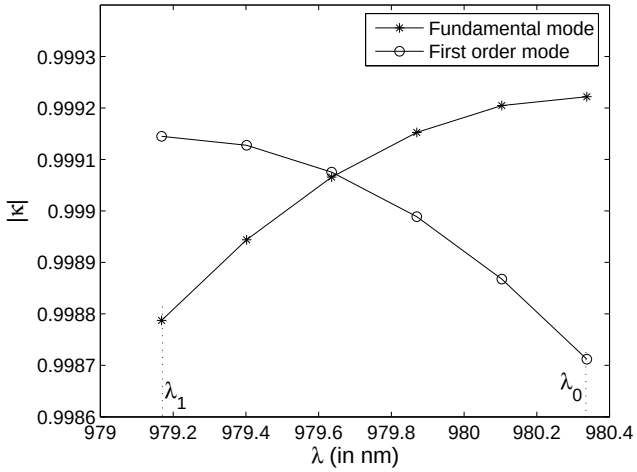

Figure 67: The variation of the magnitude of the reflected-incident fields inner product parameter $|\kappa|$ versus wavelength within the resonant wavelength range of the fundamental and first order modes of the Bragg type defect-based DBR for a fixed inner radius of $b_3 = 3\mu m$.

Finally, the resonant wavelength is plotted as a function of inner radius b_3 in Fig. 66, and $|\kappa|$ is plotted as a function of wavelength for a fixed inner radius of $b_3 = 3\mu m$

in Fig. 67.

5.4 Summary of modal discrimination properties

In VCSELs, there are two primary types of structural optical losses: modal in-plane losses and out-of-plane diffraction losses. Due to the inherent in-plane periodic boundary condition in the Fourier modal method, this method is unable to calculate the in-plane losses of the device. However, since in-plane losses in photonic crystal-based defects are small [142], the out-of-plane diffraction losses of the device are calculated using the Fourier modal method.

All structures showed increased diffraction losses for smaller inner (aperture) radius. The traditional oxide aperture showed large modal discrimination because the aperture was adjacent to uniform DBRs. The uniform DBR pairs didn't provide any lateral confinement to oxide aperture modes.

All of the photonic crystal-based DBRs considered here provided good lateral confinement to the defect modes. Even though the resonant wavelength separation between fundamental and first-order modes was significant, the modal discrimination due to diffraction losses was small. It appears that the main contribution to modal discrimination for photonic crystal-based single-mode lasers is the in-plane modal losses. Further investigation to analyze the results in this chapter is ongoing.

CHAPTER VI

SUMMARY AND FUTURE RESEARCH DIRECTIONS

Surface plasmon-based and periodic medium-based devices are attractive candidates for next-generation sub-micron-scale and ultra-fast optical devices, because of their light confinement, dispersion and extraction tailoring properties. In this research work, various periodic and surface plasmon-based devices were theoretically studied to determine their feasibility and performance as photonic devices.

6.1 Surface plasmon-based devices

Planar surface plasmon-based devices are easy to fabricate compared to cylindrical surface plasmon-based devices. Experimentalists have already demonstrated planar surface plasmon-based lasers by using an active region that has very high gain [124, 144], and by operating at long wavelengths, such that the light exhibits small loss in metals [138]. On the other hand, sub-micron cylindrical microcavities perform well in the absence of metal, which suggests that a cylindrical configuration may be desirable for surface plasmon-based lasers. For this reason, cylindrical surface plasmon-based lasers were studied using classical cylindrical waveguide theory. It was found that [72]

1. The metal cladding decreased the cutoff radius of TM and some hybrid modes, but gave rise to two classes of surface plasmon modes: the core-metal surface guided modes (short-range surface plasmon modes), and the air-metal surface guided modes (long-range surface plasmon modes).

2. The core-metal surface guided modes were well confined to the gain region but suffered large losses, and the air-metal surface guided modes suffered smaller

losses but were also less confined to the core region, due to which neither class of surface plasmon modes showed promise for lasing for the structure and the materials considered.

3. The lower order guided modes, such as the TE_{01} and HE_{11} modes, were less affected by the metal cladding, and were well confined to the core. Using an appropriate device design, higher order modes can be made to suffer significantly more losses than the lower order modes, and in this way modal discrimination can be improved.

6.2 Photonic crystal-based devices

6.2.1 Planewave expansion-based scattering matrix analysis

Presently, there exist various real space and reciprocal space methods for theoretically studying photonic crystal-based devices. Many previously developed planewave expansion-based schemes result in non-sparse and non-Hermitian matrices, and they are inefficient for larger structures [73]. In this thesis, an efficient planewave expansion scheme (Fourier modal method) was developed, and it satisfies the following conditions:

1. A numerical Fourier transform operator was directly introduced into the Helmholtz equation operator to make the problem matrix-free, and to achieve computation times that scale as $O(N \log(N))$ (where N is the number of planewaves) for calculating layer modes.

2. Only a limited number of planewaves were used for mode-matching analysis at layer interfaces.

The developed planewave expansion-based scattering matrix analysis was tested and then applied to two problems.

6.2.1.1 Robust design of photonic structures

The extrinsic losses due to fabrication errors in sub-micron structures are known to be just as important as intrinsic losses [49, 67]. A device design obtained by minimizing only intrinsic losses results in an optimum design, but a design obtained by minimizing both intrinsic and extrinsic losses, as well as constraining the sensitivity of the losses to random fabrication errors, is a robust design. A slow light coupler, which has both a linear dispersion regime region and a flat dispersion regime region, was considered as an example problem, and both optimum and robust designs were calculated. The following conclusions were drawn:

1. The fabrication errors within the linear dispersion regime region had little impact on light transmission, since the linear dispersion region allowed the passage of light with little interference.

2. The fabrication errors within the flat dispersion regime region affected the waveguide modal pattern to a great extent, and had a significant impact on light transmission.

Therefore, in the presence of fabrication defects, a design with a short flat dispersion regime region will be more robust than a design with a long flat dispersion regime region.

6.2.1.2 Modal discrimination in photonic crystal defect based VCSELs

VCSELs are micron-scale devices that are known to be versatile light sources for optical communication. However, achieving single-mode high-power operation requires large optical losses for higher order modes and large separation of resonant wavelengths. Photonic crystal patterning can be tailored to improve modal discrimination properties by ensuring that higher order modes suffer higher total optical losses than lower order modes, but our analysis of photonic crystal holey defect-based

DBRs considering only out-of-plane loss showed poorer modal discrimination properties compared to conventional VCSELs. So, our results indicate that the experimental observation of higher threshold gain [28] for the first order mode stems from higher in-plane losses [142]. The three different photonic crystal patternings had the following properties:

1. The circular holey defect structure exhibited the maximum separation of resonant wavelengths, but the fundamental mode suffered more out-of-plane losses than the first order modes.

2. The quadrilateral holey defect structure provided high contrast lateral confinement for modes, and the fundamental mode suffered less out-of-plane losses than the first order mode, and large resonant wavelength separation was observed.

3. The Bragg waveguide-type defect structure had a weak band gap effect because of the dimensionality of the structure, and therefore exhibited similar properties to the quadrilateral holey structure.

Therefore, the last two patternings had superior out-of-plane modal loss characteristics.

6.3 Future research directions

Sub-micron-scale structures have feature dimensions smaller than a micron. These devices can be integrated for all-optical signal processing on a chip. Presently, high index contrast-based devices are used for photonic integrated circuits [22], but their dimensions are on the order of a few millimeters and they are often not monolithic. Light in such structures can't be slowed significantly through structural dispersion. By contrast, sub-micron-scale structures offer the following advantages when compared to conventional photonic integrated circuits:

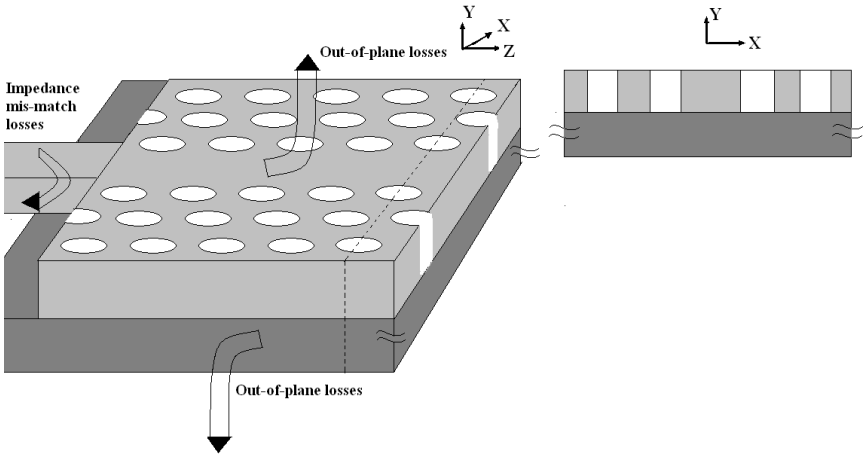

Figure 68: The sub-micron photonic crystal structure showing out-of-plane and impedance mismatch losses.

1. The non-linear, electrooptic, and absorption properties of these devices can be enhanced even for small optical pumping powers. For this reason, they are good candidates for high-speed ultra-compact switches, thresholdless lasers, and single photon detectors.

2. The structural dispersion properties can be used for slowing light.

3. The propagation, confinement, and extraction properties can be tailored.

6.3.1 Sub-micron-scale structures

There are a number of novel sub-micron-scale device concepts and issues that can be theoretically tested and improved using the Fourier modal method described in this thesis. They include:

1. Selective region pumping: for all-optical processing, slow light is essential. High-Q photonic crystal cavities have already achieved slow light. Unfortunately, in conventional photonic crystal microcavities [102], the slower the light, the smaller the operational bandwidth. Achieving simultaneously slow light and

large bandwidth is practically impossible using conventional photonic crystal-based microcavities. One solution is photonic bandgap engineering [5]. However, this solution would require a long waveguide structure. Another recently proposed solution is to use dynamic photonic crystals [33]. Through selective cavity pumping, the refractive index of an individual cavity can be varied in time. This method is theoretically predicted to overcome the fundamental delay-bandwidth constraint.

2. Out-of-plane losses: in many slow light waveguides, the slow light propagates primarily along the in-plane direction. However, there will be significant out-of-plane scattering in the flat-dispersion regime, as shown in Fig. 68. A slow light waveguide design can be significantly improved [132] by considering the important contribution of out-of-plane losses.

3. Electrical contacts: most photonic crystal-based sub-micron devices rely on optical pumping. For future applications, electrical pumping of these devices is desirable. Therefore, electrical contacts on the surface are required, and the impact of the elctrical contacts on the optical properties must be studied.

6.3.2 Micron-scale structures

Micron-scale photonic crystals have already been implemented in lasers [150, 39] for high-power single-mode operation, in LEDs for high extraction efficiency, and in fibers for endlessly single-mode operation [16]. More advanced structures in which the photonic crystal hole size is varied along the propagation direction provide another degree of freedom in design, and may improve performance. In photonic crystal-based VCSELs, if the hole size is increased along the vertical direction as shown in Fig. 69, the out-of-plane confinement of lower order modes may improve due to the decreasing effective refractive index along the z-direction. This structure may also achieve an increase in out-of-plane scattering of higher order modes, and thus improve

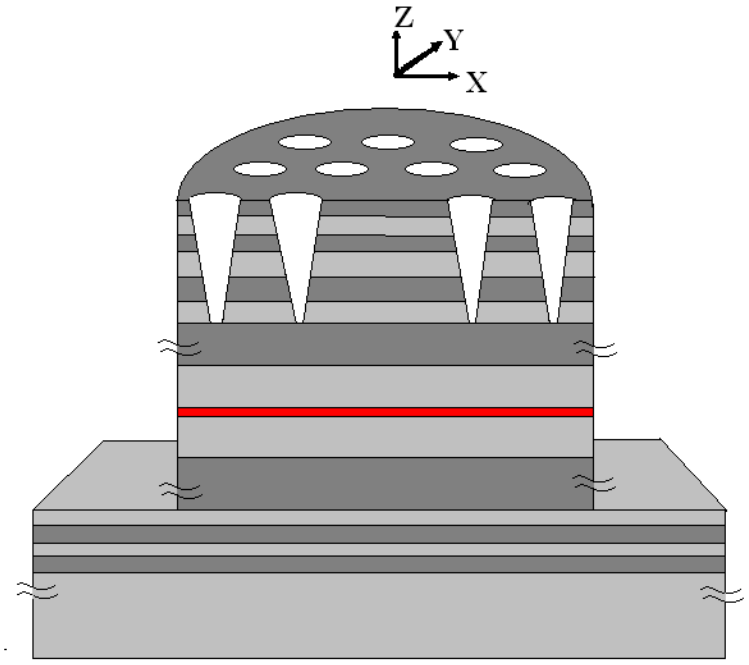

Figure 69: Novel design of photonic crystal-based VCSEL structure with conical holey defect.

modal discrimination. Conical holes have also been shown to improve the extraction efficiency of LEDs [37]. Optimization of the shape of photonic crystal holes along the vertical direction is an interesting problem that is well-suited for analysis using the Fourier modal method presented in this thesis.

6.3.3 Conclusion

The increase in demand for speed, bandwidth and efficiency of information processing and communication is driving the electronics industry towards saturation. It has already been predicted that in this century, photonics will play the role that electronics played in the last century. In the last century, the invention of the transistor and integrated circuits led to an exponential growth of electronic information processing power. Most of the electronic applications we see today were not even contemplated when the transistor was invented. A similar trend can be expected in the integration of photonic devices. Similar to a transistor or diode, photonic crystals and surface

plasmons offer 2D and 3D control of photons in micro and nano-scales, and have challenged the photonics community on both fundamental and application fronts. As photonic integrated circuits become a reality, all-optical processing power will eventually rival that of electronics. Development of this technology will require reliable and predictive photonics CAD tools, such as the Fourier modal method code described in this thesis.

APPENDIX A

CYLINDRICAL WAVEGUIDE THEORY FOR THREE LAYERED STRUCTURE

Analytically, the electric and magnetic fields in cylindrical waveguide are known to have Bessel and Neumann form along radial direction, since and cosine form along angular direction and exponential form along propagation direction as solution [17]. Assuming such form for z-field components, all other field components are calculated by matching boundary conditions using Maxwell's equations in cylindrical coordinates.

In layer I (the inner medium),

$$E_z = A^I \frac{I_\nu(k_t^I \rho)}{I_\nu(k_t^I a)} \cos\nu\phi e^{-ik_z z} \tag{56}$$

$$H_z = B^I \frac{I_\nu(k_t^I \rho)}{I_\nu(k_t^I a)} \sin\nu\phi e^{-ik_z z} \tag{57}$$

$$\begin{aligned} E_\phi &= -i\frac{\omega\mu}{(\omega^2\mu\epsilon - k_z^2)}\left(\frac{k_z}{\omega\mu}\frac{\partial E_z}{\rho\partial\phi} - \frac{\partial H_z}{\partial\rho}\right) && (58)\\ &= i\frac{k_z}{k_t^{II^2}}\left(-\frac{\nu}{\rho}\right)A^I\frac{I_\nu(k_t^I\rho)}{I_\nu(k_t^I a)}sin(\nu\phi) \\ &\quad -i\frac{k_0\eta}{k_t^I I_\nu(k_t^I a)}B^I\left(\frac{\nu}{k_t^I\rho}I_\nu(k_t^I\rho) + I_{\nu+1}(k_t^I\rho)\right)\sin(\nu\phi) && (59)\end{aligned}$$

$$\begin{aligned} H_\phi &= -i\frac{\omega\epsilon}{(\omega^2\mu\epsilon - k_z^2)}\left(\frac{k_z}{\omega\epsilon}\frac{\partial H_z}{\rho\partial\phi} + \frac{\partial E_z}{\partial\rho}\right) && (60)\\ &= i\frac{k_z}{k_t^{I^2}}\left(\frac{\nu}{\rho}\right)B^I\frac{I_\nu(k_t^I\rho)}{I_\nu(k_t^I a)}cos(\nu\phi) \\ &\quad +i\frac{k^{I^2}}{\eta k_0 k_t^I I_\nu(k_t^I a)}A^I\left(\frac{\nu}{k_t^I\rho}I_\nu(k_t^I\rho) + I_{\nu+1}(k_t^I\rho)\right)\cos(\nu\phi) && (61)\end{aligned}$$

In layer II (cladding medium),

$$E_z = (A_1^{II}\frac{I_\nu(k_t^{II}\rho)}{I_\nu(k_t^{II}a)} + A_2^{II}\frac{K_\nu(k_t^{II}\rho)}{K_\nu(k_t^{II}a)})\cos\nu\phi e^{-ik_z z} \tag{62}$$

$$H_z = (B_1^{II}\frac{I_\nu(k_t^{II}\rho)}{I_\nu(k_t^{II}a)} + B_2^{II}\frac{K_\nu(k_t^{II}\rho)}{K_\nu(k_t^{II}a)})\sin\nu\phi e^{-ik_z z} \tag{63}$$

$$\begin{aligned} E_\phi &= -i\frac{\omega\mu}{(\omega^2\mu\epsilon - k_z^2)}(\frac{k_z}{\omega\mu}\frac{\partial E_z}{\rho\partial\phi} - \frac{\partial H_z}{\partial\rho}) \\ &= i\frac{k_z}{k_t^{II^2}}(-\frac{\nu}{\rho})(A_1^{II}\frac{I_\nu(k_t^{II}\rho)}{I_\nu(k_t^{II}a)} + A_2^{II}\frac{K_\nu(k_t^{II}\rho)}{K_\nu(k_t^{II}a)})\sin(\nu\phi) \\ &\quad -i\frac{k_0\eta}{k_t^{II}}(\frac{B_1^{II}}{I_\nu(k_t^{II}a)}(\frac{\nu}{k_t^{II}\rho}I_\nu(k_t^{II}\rho) + I_{\nu+1}(k_t^{II}\rho)) \\ &\quad +\frac{B_2^{II}}{I_\nu(k_t^{II}a)}(\frac{\nu}{k_t^{II}\rho}K_\nu(k_t^{II}\rho) - K_{\nu+1}(k_t^{II}\rho)))\sin(\nu\phi) \end{aligned} \tag{64}$$

$$\begin{aligned} H_\phi &= -i\frac{\omega\epsilon}{(\omega^2\mu\epsilon - k_z^2)}(\frac{k_z}{\omega\epsilon}\frac{\partial H_z}{\rho\partial\phi} + \frac{\partial E_z}{\partial\rho}) \\ &= i\frac{k_z}{k_t^{II^2}}(\frac{\nu}{\rho})(B_1^{II}\frac{I_\nu(k_t^{II}\rho)}{I_\nu(k_t^{II}a)} + B_2^{II}\frac{I_\nu(k_t^{II}\rho)}{I_\nu(k_t^{II}a)})\cos(\nu\phi) \\ &\quad +i\frac{k^{II^2}}{\eta k_0 k_t^{II}}(\frac{A_1^{II}}{I_\nu(k_t^{II}a)}(\frac{\nu}{k_t^{II}\rho}I_\nu(k_t^{II}\rho) + I_{\nu+1}(k_t^{II}\rho)) \\ &\quad +\frac{A_2^{II}}{K_\nu(k_t^{II}a)}(\frac{\nu}{k_t^{II}\rho}K_\nu(k_t^{II}\rho) - K_{\nu+1}(k_t^{II}\rho)))\cos(\nu\phi) \end{aligned} \tag{65}$$

In layer III (outer medium),

$$E_z = A^{III}\frac{K_\nu(k_t^{III}\rho)}{K_\nu(k_t^{III}(a+t))}\cos\nu\phi e^{-ik_z z} \tag{66}$$

$$H_z = B^{III}\frac{K_\nu(k_t^{III}\rho)}{K_\nu(k_t^{III}(a+t))}\sin\nu\phi e^{-ik_z z} \tag{67}$$

$$\begin{aligned} E_\phi &= -i\frac{\omega\mu}{(\omega^2\mu\epsilon - k_z^2)}(\frac{k_z}{\omega\mu}\frac{\partial E_z}{\rho\partial\phi} - \frac{\partial H_z}{\partial\rho}) \\ &= i\frac{k_z}{k_t^{III^2}}(-\frac{\nu}{\rho})A^{III}\frac{K_\nu(k_t^{III}\rho)}{K_\nu(k_t^{III}(a+t))}\sin(\nu\phi) \\ &\quad -i\frac{k_0\eta}{k_t^{III}K_\nu(k_t^{III}(a+t))}B^{III}(\frac{\nu}{k_t^{III}\rho}K_\nu(k_t^{III}\rho) - K_{\nu+1}(k_t^{III}\rho))\sin(\nu\phi) \end{aligned} \tag{68}$$

$$
\begin{aligned}
H_\phi &= -i\frac{\omega\epsilon}{(\omega^2\mu\epsilon - k_z^2)}(\frac{k_z}{\omega\epsilon}\frac{\partial H_z}{\rho\partial\phi} + \frac{\partial E_z}{\partial\rho}) \\
&= i\frac{k_z}{k_t^{III^2}}(\frac{\nu}{\rho})B^{III}\frac{K_\nu(k_t^{III}\rho)}{K_\nu(k_t^{III}(a+t))}\cos(\nu\phi) \\
&\quad +i\frac{k^{III^2}}{\eta k_0 k_t^{III} K_\nu(k_t^I(a+t))}A^{III}(\frac{\nu}{k_t^{III}\rho}K_\nu(k_t^{III}\rho) - K_{\nu+1}(k_t^{III}\rho))\cos(\nu\phi) \quad (69)
\end{aligned}
$$

On matching field amplitudes E_z, H_z, E_ϕ and H_ϕ, at $\rho = a$,

$$
A^I = A_1^{II} + A_2^{II} \quad (70)
$$

$$
B^I = B_1^{II} + B_2^{II} \quad (71)
$$

$$
\begin{aligned}
\frac{k_z}{k_t^2}(-\frac{\nu}{a})A^I - \frac{k_0\eta}{k_t}B^I(\frac{\nu}{k_t^I a} + \frac{I_{\nu+1}(k_t^I a)}{I_\nu(k_t^I a)}) &= \frac{k_z}{k_t^2}(-\frac{\nu}{a})(A_1^{II} + A_2^{II}) \\
&\quad -\frac{k_0\eta}{k_t}(B_1^{II}(\frac{\nu}{k_t^{II}a} + \frac{I_{\nu+1}(k_t^{II}a)}{I_\nu(k_t^{II}a)}) \\
&\quad +B_2^{II}(\frac{\nu}{k_t^{II}} - \frac{K_{\nu+1}(k_t^{II}a)}{K_\nu(k_t^{II}a)})) \quad (72)
\end{aligned}
$$

$$
\begin{aligned}
\frac{k_z}{k_t^2}(\frac{\nu}{a})B_1^I + \frac{k_I^2}{k_0 k_t^I \eta}A^I(\frac{\nu}{k_t^I a} + \frac{I_{\nu+1}(k_t a)}{I_\nu(k_t^I a)}) &= \frac{k_z^2}{k_t^{II^2}}(\frac{\nu}{a})(B_1^{II} + B_2^{II}) \\
&\quad +\frac{k^{II^2}}{k_0 k_t^{II^2}\eta}(A_1^{II}(\frac{\nu}{k_t^{II}a} + \frac{I_{\nu+1}(k_t^{II}a)}{I_\nu(k_t^{II}a)}) \\
&\quad +A_2^{II}(\frac{\nu}{k_t^{II}a} - \frac{K_{\nu+1}(k_t^{II}a)}{K_\nu(k_t^{II}a)})) \quad (73)
\end{aligned}
$$

At $\rho = (a+t)$,

$$
A_1^{II}\frac{I_\nu(k_t^{II}(a+t))}{I_\nu(k_t^{II}a)} + A_2^{II}\frac{K_\nu(k_t^{II}(a+t))}{K_\nu(k_t^{II}a)} = A^{III} \quad (74)
$$

$$B_1^{II}\frac{I_\nu(k_t^{II}(a+t))}{I_\nu(k_t^{II}a)}+B_2^{II}\frac{K_\nu(k_t^{II}(a+t))}{K_\nu(k_t^{II}a)} = B^{III} \tag{75}$$

$$\begin{aligned}
&\frac{k_z^2}{k_t^2}(-\frac{\nu}{(a+t)})(A_1^{II}\frac{I_\nu(k_t^{II}(a+t))}{I_\nu(k_t^{II}a)}\\
&\qquad +A_2^{II}\frac{K_\nu(k_t^{II}(a+t))}{K_\nu(k_t^{II}a)})\\
&-\frac{k_0\nu}{k_t^{II}}(\frac{B_1^{II}}{I_\nu(k_t^{II}a)}(\frac{\nu}{k_t^{II}(a+t)}I_\nu(k_t^{II}(a+t))\\
&\qquad +I_{\nu+1}(k_t^{II}(a+t)))\\
&+\frac{B_2^{II}}{K_\nu(k_t^{II}(a+t))}(\frac{\nu}{k_t^{II}(a+t)}K_\nu(k_t^{II}(a+t))\\
&\qquad -K_{\nu+1}(k_t^{II}(a+t)))) = \frac{k_z}{k_t^{III^2}}(-\frac{\nu}{a+t})A^{III}\\
&\qquad -\frac{k_0\eta}{k_t^{III}}B^{III}(\frac{\nu}{k_t^{III}(a+t)}\\
&\qquad -\frac{K_{\nu+1}(k_t^{III}(a+t))}{K_\nu(k_t^{III}(a+t))})
\end{aligned} \tag{76}$$

$$\begin{aligned}
&\frac{k_z^2}{k_t^2}(\frac{\nu}{(a+t)})(B_1^{II}\frac{I_\nu(k_t^{II}(a+t))}{I_\nu(k_t^{II}a)}\\
&\qquad +B_2^{II}\frac{K_\nu(k_t^{II}(a+t))}{K_\nu(k_t^{II}a)})\\
&-\frac{k_0^2}{k_0k_t^{II}\eta}(\frac{A_1^{II}}{I_\nu(k_t^{II}a)}(\frac{\nu}{k_t^{II}(a+t)}I_\nu(k_t^{II}(a+t))\\
&\qquad +I_{\nu+1}(k_t^{II}(a+t)))\\
&+\frac{A_2^{II}}{K_\nu(k_t^{II}(a+t))}(\frac{\nu}{k_t^{II}(a+t)}K_\nu(k_t^{II}(a+t))\\
&\qquad -K_{\nu+1}(k_t^{II}(a+t)))) = \frac{k_z}{k_t^{III^2}}(-\frac{\nu}{a+t})B^{III}\\
&\qquad -\frac{k_0k_{III}}{k_t^{III}\eta}A^{III}(\frac{\nu}{k_t^{III}(a+t)}\\
&\qquad -\frac{K_{\nu+1}(k_t^{III}(a+t))}{K_\nu(k_t^{III}(a+t))})
\end{aligned} \tag{77}$$

Equations 70 through 77 results in the dispersion relation given in equation 7 of Chapter 2. For TE and TM mode calculation, the size of the matrix in equation 7 is reduced to 4×4 by setting $E_z = H_\phi = 0$ and $H_z = E_\phi = 0$ respectively.

APPENDIX B

MATRIX TO MATRIXFREE SOLUTION

The two Maxwell curl equations for time-harmonic fields in a source-free medium are,

$$\nabla \times H = i\omega\epsilon E, \quad \nabla \times E = -i\omega\mu H \tag{78}$$

The above equations can be written in the form,

$$\frac{\partial H_z}{\partial y} - \frac{\partial H_y}{\partial z} = i\omega\epsilon E_x, \quad \frac{\partial E_z}{\partial y} - \frac{\partial E_y}{\partial z} = -i\omega\mu H_x \tag{79}$$

$$-\frac{\partial H_z}{\partial x} + \frac{\partial H_x}{\partial z} = i\omega\epsilon E_y, \quad -\frac{\partial E_z}{\partial x} + \frac{\partial E_y}{\partial z} = -i\omega\mu H_x \tag{80}$$

$$\frac{\partial H_y}{\partial x} - \frac{\partial H_x}{\partial y} = i\omega\epsilon E_z, \quad \frac{\partial E_y}{\partial x} - \frac{\partial E_x}{\partial y} = -i\omega\mu H_z \tag{81}$$

From the above set of equations,

$$H_z = \frac{i}{\omega\mu} \begin{bmatrix} \frac{\partial}{\partial x} & -\frac{\partial}{\partial y} \end{bmatrix} \begin{bmatrix} E_y \\ E_x \end{bmatrix} \tag{82}$$

$$E_z = -\frac{i}{\omega\epsilon} \begin{bmatrix} \frac{\partial}{\partial x} & -\frac{\partial}{\partial y} \end{bmatrix} \begin{bmatrix} H_y \\ H_x \end{bmatrix} \tag{83}$$

Substituting the above equations 82 and 83 in 79 and 80 we get,

$$\frac{\partial}{\partial z} \begin{bmatrix} H_y \\ H_x \end{bmatrix} = \begin{bmatrix} \frac{\partial H_z}{\partial y} - i\omega\epsilon E_x \\ \frac{\partial H_z}{\partial x} + i\omega\epsilon E_y \end{bmatrix} \tag{84}$$

$$\frac{\partial}{\partial z} \begin{bmatrix} E_y \\ E_x \end{bmatrix} = \begin{bmatrix} \frac{\partial E_z}{\partial y} + i\omega\mu H_x \\ \frac{\partial E_z}{\partial x} - i\omega\mu H_y \end{bmatrix} \tag{85}$$

Using equations 82 and 83 in equations 84 and 85,

$$\frac{\partial}{\partial z}\begin{bmatrix} H_x \\ H_y \end{bmatrix} = \begin{bmatrix} \frac{\partial}{\partial x}\frac{i}{\omega\mu}\frac{\partial E_y}{\partial x} - \frac{\partial}{\partial x}\frac{i}{\omega\mu}\frac{\partial E_x}{\partial y} + i\omega\epsilon E_y \\ \frac{\partial}{\partial y}\frac{i}{\omega\mu}\frac{\partial E_y}{\partial x} - \frac{\partial}{\partial y}\frac{i}{\omega\mu}\frac{\partial E_x}{\partial y} - i\omega\epsilon E_x \end{bmatrix} \tag{86}$$

$$\frac{\partial}{\partial z}\begin{bmatrix} E_x \\ E_y \end{bmatrix} = \begin{bmatrix} -\frac{\partial}{\partial x}\frac{i}{\omega\epsilon}\frac{\partial H_y}{\partial x} + \frac{\partial}{\partial x}\frac{i}{\omega\epsilon}\frac{\partial H_x}{\partial y} - i\omega\mu H_y \\ -\frac{\partial}{\partial y}\frac{i}{\omega\epsilon}\frac{\partial H_y}{\partial x} + \frac{\partial}{\partial y}\frac{i}{\omega\epsilon}\frac{\partial H_x}{\partial y} + i\omega\mu H_x \end{bmatrix} \tag{87}$$

$\Rightarrow$

$$-ik_z\begin{bmatrix} H_x \\ H_y \end{bmatrix} = \begin{bmatrix} \frac{\partial}{\partial x}\frac{i}{\omega\mu}\frac{\partial}{\partial x} + i\omega\epsilon & -\frac{\partial}{\partial x}\frac{i}{\omega\mu}\frac{\partial}{\partial y} \\ \frac{\partial}{\partial y}\frac{i}{\omega\mu}\frac{\partial}{\partial x} & -\frac{\partial}{\partial y}\frac{i}{\omega\mu}\frac{\partial}{\partial y} - i\omega\epsilon \end{bmatrix}\begin{bmatrix} E_y \\ E_x \end{bmatrix} \tag{88}$$

$$-ik_z\begin{bmatrix} E_x \\ E_y \end{bmatrix} = \begin{bmatrix} -\frac{\partial}{\partial x}\frac{i}{\omega\epsilon}\frac{\partial}{\partial x} - i\omega\mu & -\frac{\partial}{\partial x}\frac{i}{\omega\epsilon}\frac{\partial}{\partial y} \\ -\frac{\partial}{\partial y}\frac{i}{\omega\epsilon}\frac{\partial}{\partial x} & \frac{\partial}{\partial y}\frac{i}{\omega\epsilon}\frac{\partial}{\partial y} + i\omega\mu \end{bmatrix}\begin{bmatrix} H_y \\ H_x \end{bmatrix} \tag{89}$$

$\Rightarrow$

$$\begin{bmatrix} \frac{\partial}{\partial x}\frac{i}{\omega\mu}\frac{\partial}{\partial x} + i\omega\epsilon & -\frac{\partial}{\partial x}\frac{i}{\omega\mu}\frac{\partial}{\partial y} \\ \frac{\partial}{\partial y}\frac{i}{\omega\mu}\frac{\partial}{\partial x} & -\frac{\partial}{\partial y}\frac{i}{\omega\mu}\frac{\partial}{\partial y} - i\omega\epsilon \end{bmatrix}\begin{bmatrix} \frac{\partial}{\partial y}\frac{i}{\omega\epsilon}\frac{\partial}{\partial y} + i\omega\mu & -\frac{\partial}{\partial y}\frac{i}{\omega\epsilon}\frac{\partial}{\partial x} \\ \frac{\partial}{\partial x}\frac{i}{\omega\epsilon}\frac{\partial}{\partial y} & -\frac{\partial}{\partial x}\frac{i}{\omega\epsilon}\frac{\partial}{\partial x} - i\omega\mu \end{bmatrix}\begin{bmatrix} H_x \\ H_y \end{bmatrix} = -k_z^2\begin{bmatrix} H_x \\ H_y \end{bmatrix} \tag{90}$$

On substituting equation 89 in 88 we get,

$$\begin{bmatrix} \left(\left(\frac{\partial}{\partial x}\frac{i}{\omega\mu}\frac{\partial}{\partial x} + i\omega\epsilon\right)\left(\frac{\partial}{\partial y}\frac{i}{\omega\epsilon}\frac{\partial}{\partial y} + i\omega\mu\right) - \left(\frac{\partial}{\partial x}\frac{i}{\omega\mu}\frac{\partial}{\partial y}\right)\left(\frac{\partial}{\partial x}\frac{i}{\omega\epsilon}\frac{\partial}{\partial y}\right)\right) & \left(-\left(\frac{\partial}{\partial x}\frac{i}{\omega\mu}\frac{\partial}{\partial x} + i\omega\epsilon\right)\left(\frac{\partial}{\partial y}\frac{i}{\omega\epsilon}\frac{\partial}{\partial x}\right) + \left(\frac{\partial}{\partial x}\frac{i}{\omega\mu}\frac{\partial}{\partial y}\right)\left(\frac{\partial}{\partial x}\frac{i}{\omega\epsilon}\frac{\partial}{\partial x} + i\omega\mu\right)\right) \\ \left(\left(\frac{\partial}{\partial y}\frac{i}{\omega\mu}\frac{\partial}{\partial x}\right)\left(\frac{\partial}{\partial y}\frac{i}{\omega\epsilon}\frac{\partial}{\partial y} + i\omega\mu\right) - \left(\frac{\partial}{\partial y}\frac{i}{\omega\mu}\frac{\partial}{\partial y} + i\omega\epsilon\right)\left(\frac{\partial}{\partial x}\frac{i}{\omega\epsilon}\frac{\partial}{\partial y}\right)\right) & \left(-\left(\frac{\partial}{\partial x}\frac{i}{\omega\epsilon}\frac{\partial}{\partial y}\right)\left(\frac{\partial}{\partial y}\frac{i}{\omega\epsilon}\frac{\partial}{\partial y} + i\omega\mu\right) + \left(\frac{\partial}{\partial y}\frac{i}{\omega\mu}\frac{\partial}{\partial y} + i\omega\epsilon\right)\left(\frac{\partial}{\partial x}\frac{i}{\omega\epsilon}\frac{\partial}{\partial x} + i\omega\mu\right)\right) \end{bmatrix}\begin{bmatrix} H_x \\ H_y \end{bmatrix} = -k_z^2\begin{bmatrix} H_x \\ H_y \end{bmatrix} \tag{91}$$

If the magnetic field,

$$\vec{H}(\vec{r}) = \sum_G (H_{Gx}\hat{x} + H_{Gy}\hat{y} + H_{Gz}\hat{z})\psi_{k+G}(x,y)\exp(-ik_z z)$$

where ψ_G is an exponential set of orthonormal functions representing a complete basis [29] set. Now by substituting the above equation for $\vec{H}(\vec{r})$ in (91) and multiplying by the conjugate of the basis function on both sides and integrating throughout the real space, (91) can be reduced to the following form,

$$\begin{bmatrix} A_{11} & A_{12} \\ A_{21} & A_{22} \end{bmatrix}\begin{bmatrix} H_{Gx} \\ H_{Gy} \end{bmatrix} = k_z^2 B\begin{bmatrix} H_{Gx} \\ H_{Gy} \end{bmatrix} \tag{92}$$

¿From equation. 91 in differential form, $A_{11}H_x(\vec{r})$ term is used to demonstrate the deduction of matrix-free implementation. In differential form,

$$\begin{aligned}
A_{11}H_x(\vec{r}) &= \int_\Omega \exp(i(\vec{k}+\vec{G'}).\vec{r})((\frac{\partial}{\partial x}\frac{i}{\omega\mu}\frac{\partial}{\partial x} \\
&\quad +i\omega\epsilon)(\frac{\partial}{\partial y}\frac{i}{\omega\epsilon}\frac{\partial}{\partial y}+i\omega\mu) \\
&\quad -(\frac{\partial}{\partial x}\frac{i}{\omega\mu}\frac{\partial}{\partial y}\frac{\partial}{\partial x}\frac{i}{\omega\epsilon}\frac{\partial}{\partial y}))H_x(\vec{r})d\Omega \qquad (93) \\
&= \int_\Omega \exp(i(\vec{k}+\vec{G'}).\vec{r})(\frac{\partial}{\partial x}\frac{i}{\omega\mu}\frac{\partial}{\partial x}i\omega\mu \\
&\quad +i\omega\epsilon\frac{\partial}{\partial y}\frac{i}{\omega\epsilon}\frac{\partial}{\partial y}-\omega^2\mu\epsilon)H_x(\vec{r})d\Omega \qquad (94) \\
&= \int_\Omega \exp(i(\vec{k}+\vec{G'}).\vec{r})(-\frac{\partial^2}{\partial x^2}-\omega\epsilon\frac{\partial}{\partial y}\frac{1}{\omega\epsilon}\frac{\partial}{\partial y}-\omega^2\mu\epsilon)H_x(\vec{r})d\Omega \qquad (95)
\end{aligned}$$

On substituting, $H_x(\vec{r}) = \sum_G H_{Gx}\exp(-i(\vec{k}+\vec{G}).\vec{r})$,

$$\begin{aligned}
A_{11}H_x(\vec{r}) &= (k_x+G_x)^2H_{Gx}\delta_{G',G} \\
&\quad -\int_\Omega \exp(i(\vec{k}+\vec{G'}).\vec{r})\omega\epsilon\frac{\partial}{\partial y}\frac{1}{\omega\epsilon}\frac{\partial}{\partial y}\sum_G H_{Gx}\exp(-i(\vec{k}+\vec{G}).\vec{r})d\Omega \\
&\quad -\int_\Omega \exp(i(\vec{k}+\vec{G'}).\vec{r})\omega^2\mu\epsilon\sum_G H_{Gx}\exp(-i(\vec{k}+\vec{G}).\vec{r})d\Omega \qquad (96) \\
&= (k_x+G_x)^2H_{Gx}\delta_{G',G} \\
&\quad -\int_\Omega \exp(i(\vec{k}+\vec{G'}).\vec{r})\omega\epsilon\frac{\partial}{\partial y}\frac{1}{\omega\epsilon} \\
&\quad \sum_G -i(k_y+G_y)H_{Gx}\exp(-i(\vec{k}+\vec{G}).\vec{r})d\Omega \\
&\quad -\int_\Omega \exp(i(\vec{k}+\vec{G'}).\vec{r})\omega^2\mu\epsilon\exp(-i\vec{k}.\vec{r})IFT\{H_{Gx}\}d\Omega \qquad (97) \\
&= (k_x+G_x)^2H_{Gx}\delta_{G',G} \\
&\quad +i\int_\Omega \exp(i(\vec{k}+\vec{G'}).\vec{r})\omega\epsilon\frac{\partial}{\partial y}\frac{1}{\omega\epsilon} \\
&\quad \exp(-i\vec{k}.\vec{r})IFT\{(k_y+G_y)H_{Gx}\}d\Omega \\
&\quad -\int_\Omega \exp(i\vec{G'}\vec{r})\omega^2\mu\epsilon IFT\{H_{Gx}\}d\Omega \qquad (98)
\end{aligned}$$

$$
\begin{aligned}
A_{11}H_x(\vec{r}) &= (k_x+G_x)^2 H_{Gx}\delta_{G',G} \\
&\quad +i\int_\Omega \exp(i(\vec{k}+\vec{G'}).\vec{r})\omega\epsilon\frac{\partial}{\partial y}\frac{1}{\omega} \\
&\quad \sum_G [FT\{\frac{1}{\epsilon}IFT\{(k_y+G_y)H_{Gx}\}\}]_G \exp(-i(\vec{k}+\vec{G}).\vec{r})d\Omega \\
&\quad -\omega^2\mu FT\{\epsilon IFT\{H_{Gx}\}\} \qquad (99) \\
&= (k_x+G_x)^2 H_{Gx}\delta_{G',G} \\
&\quad +i\int_\Omega \exp(i(\vec{k}+\vec{G'}).\vec{r})\epsilon \\
&\quad \sum_G -i(k_y+G_y)[FT\{\frac{1}{\epsilon}IFT\{(k_y+G_y)H_{Gx}\}\}]_G \\
&\quad \exp(-i(\vec{k}+\vec{G}).\vec{r})d\Omega \\
&\quad -\omega^2\mu FT\{\epsilon IFT\{H_{Gx}\}\} \qquad (100) \\
&= (k_x+G_x)^2 H_{Gx}\delta_{G',G} \\
&\quad +\int_\Omega \exp(i(\vec{k}+\vec{G'}).\vec{r})\epsilon\exp(-i\vec{k}.\vec{r}) \\
&\quad IFT\{(k_y+G_y)FT\{\frac{1}{\epsilon}IFT\{(k_y+G_y)H_{Gx}\}\}\}d\Omega \\
&\quad -\omega^2\mu FT\{\epsilon IFT\{H_{Gx}\}\} \qquad (101) \\
&= (k_x+G_x)^2 H_{Gx}\delta_{G',G} \\
&\quad +\int_\Omega \exp(i\vec{G'}.\vec{r})\epsilon \\
&\quad IFT\{(k_y+G_y)FT\{\frac{1}{\epsilon}IFT\{(k_y+G_y)H_{Gx}\}\}\}d\Omega \\
&\quad -\omega^2\mu FT\{\epsilon IFT\{H_{Gx}\}\} \qquad (102) \\
&= (k_x+G_x)^2 H_{Gx}\delta_{G',G} \\
&\quad +FT\{\epsilon IFT\{(k_y+G_y)FT\{\frac{1}{\epsilon}IFT\{(k_y+G_y)H_{Gx}\}\}\}\} \\
&\quad -\omega^2\mu FT\{\epsilon IFT\{H_{Gx}\}\} \qquad (103)
\end{aligned}
$$

Overall in the above equation set, note that only ϵ is in real space (assuming μ is not spatially varying) and all other entities are in reciprocal space. The term,

FT(real space term)IFT in reciprocal space is a matrix representing convolution of the real space term with other terms. Through the use of FT and IFT operators and by keeping ϵ in real space, the matrix construction and matrix multiplication which is $O(N^2)$ is avoided. Similarly other matrix-free equations are derived.

REFERENCES

[1] Adibi, A., Lee, R. K., Xu, Y., Yariv, A., and Scherer, A., "Properties of the slab modes in photonic crystal optical waveguides," *Electron lett.*, vol. 36, p. 1376, 2000.

[2] Akahane, Y., Asano, T., Song, B.-S., and Noda, S., "High-q nanocavity in a two-dimensional photonic crystal," *Nature*, vol. 425, p. 944, 2003.

[3] Al-Bader, S. J. and Imtaar, M., "Azhimuthally uniform surface-plasma modes in thin metallic cylindrical shells," *IEEE J. Quant. Elect.*, vol. 27, no. 6, 1991.

[4] Askari, M., Momeni, B., Yegnanarayanan, S., Eftekhar, A., and Adibi, A., "Efficient coupling of light into the planar photonic crystal waveguides in the slow group velocity regime," *Proc. of SPIE*, vol. 6901, p. 69011A, 2008.

[5] Baba, T. and Mori, D., "Slow light engineering in photonic crystals," *Phys. Rev. D*, vol. 40, p. 2659, 2007.

[6] Barclay, P., Srinivasan, K., Borselli, M., and Painter, O., "Efficient input and output fiber coupling to a photonic crystal waveguide," *Opt. lett.*, vol. 29, p. 697, 2004.

[7] Barnes, W. L., Dereux, A., and Ebbesen, T. W., "Surface plasmon subwavelength optics," *Nature*, vol. 424, p. 824, 2003.

[8] Bava, G. P., Debernardi, P., and Fratta, L., "Three-dimensional model for vectorial fields in vertical-cavity surface-emitting lasers," *Phy. Rev. A*, vol. 63, pp. 023816/1–023816/13, 2001.

[9] Bayindir, M., Temelkuran, B., and Ozbar, E., "Photonic-crystal based beam splitter," *Appl. Phys. Lett.*, vol. 77, pp. 3902–3904, 2000.

[10] Bergman, D. J. and Stockman, M. I., "Surface plasmon amplification by stimulated emission of radiation: Quantum generation of coherent surface plasmons in nanosystems," *Phys. Rev. Lett.*, vol. 90, pp. 027402/1–027402/4, 2003.

[11] Bienstman, P., "Rigorous and efficient modelling of wavelength scale photonic components," tech. rep., Department of Information Technology, University of Gent, Gent, Belgium, 2001.

[12] Bienstman, P., "Two-stage mode finder for waveguides with a 2d cross section," *Opt. Quant. Electron.*, vol. 36, pp. 5–14, 2004.

[13] Bienstman, P., Assefa, S., Johnson, S. G., Joannapoulos, J. D., Petrich, G., and Kolodziejski, L., "Taper structures for coupling into photonic crystal slab waveguides," *Opt. Phys.*, vol. 20, p. 1817, 2003.

[14] Bienstman, P. and Baets, R., "Rigorous and efficient optical vcsel model based on vectorial eigenmode expansion and perfectly matched layers," *IEE-Optoelecron. Proc.*, vol. 149, pp. 161–165, 2002.

[15] Bienstman, P., Baets, R., Vukusic, J., Larsson, A., Noble, M. J., Brunner, M., Gulden, K., Debernardi, P., Fratta, L., Bava, G. P., Wenzel, H., Klein, B., Conradi, O., Pregla, R., Riyopoulos, S. A., Seurin, J. P., and Chuang, S. L., "Comparison of optical vcsel models on the simulation of oxide-confined devices," *IEEE J. Quant. Electron.*, vol. 37, pp. 1618–1631, 2001.

[16] Birks, T. A., Knight, J. C., and Russell, P. S. J., "Endlessly single-mode photonic crystal fiber," *Opt. lett.*, vol. 22, pp. 855–869, 1997.

[17] Buck, J. A., *Fundamentals Of Optical Fibers.* Hoboken, NJ: Wiley-Interscience, 2004.

[18] Burke, J. J., Stegeman, G. I., and Tamir, T., "Surface-polariton-like waves guided by thin, lossy metal films," *Phys. Rev. B.*, vol. 33, 1986.

[19] Chietera, G., Bouk, A., Poletti, F., Poli, F., Selleri, S., and Cucinotta, A., "Numerical design for efficiently coupling conventional and photonic-crystal waveguides," *Microwave and Opt. Tech. lett*, vol. 42, p. 196, 2004.

[20] Choi, H., Austin, R., Allen, J. K., McDowell, D. L., Mistree, F., and Benson, D. J., "An approach for robust design of reactive powder metal mixtures based on non-deterministic micro-scale shock simulation," *Journ. of Computer-aided materials design*, vol. 12, p. 57, 2005.

[21] Choquette, K. D., Ritchie, D. A., and Leibenguth, R. E., "Temperature dependence of gain-guided vertical-cavity surface-emitting lasers," *Appl. Phys. Lett.*, vol. 64, pp. 2062–2064, 1994.

[22] Coldren, L. A., "Inp-based photonic integrated circuits," *CLEO/QELS '08*, no. CTuBB1, 2008.

[23] Conradi, O., Helfert, S., and Pregla, R., "Comprehensive modeling of vertical-cavity laser-diodes by the method of lines," *IEEE J. of Quant. Electron.*, vol. 37, pp. 928–935, 2001.

[24] Constantinou, C. and Jones, R., "Path-integral analysis of an arbitrarily tapered, multimode, graded-index waveguide: The inverse-square law and parabolic tapers," *IEE Proc. of Optoelectronics*, vol. 139, p. 365, 1992.

[25] Czyszanowski, T., Dems, M., Thienpont, H., and Panajotov, K., "Modal behavior of photonic-crystal vertical-cavity surface-emitting diode laser analyzed with plane wave admittance method," *Opt. Quant. Electron.*, vol. 39, pp. 427–433, 2007.

[26] Danner, A. J., J. J. Raftery, J., Leisher, P. O., and Choquette, K. D., "Single mode photonic crystal vertical cavity lasers," *Appl. Phys. lett.*, vol. 88, p. 091114, 2006.

[27] Delbeke, D., Bienstman, P., Bockstaele, R., and Baets, R., "Rigorous electromagnetic analysis of dipole emission in periodically corrugated layers: the grating-assisted resonant-cavity light-emitting diode," *J. Opt. Soc. Am. A.*, vol. 19, pp. 871–880, 2002.

[28] Dems, M., Czyszanowski, T., and Panajotov, K., "Numerical analysis of high q-factor photonic-crystal vcsels with plane-wave admittance method," *Opt. Quant. Electron.*, vol. 39, pp. 419–426, 2007.

[29] Dems, M., Kotynskiand, R., and Panajotov, K., "Planewave admittance method - a novel approach for determining the electromagnetic modes in photonic structures," *Opt. Express.*, vol. 13, pp. 3196–3207, 2005.

[30] Deppe, D. G. and Huffaker, D. L., "High spatial coherence vertical-cavity surface-emitting laser using a long monolithic cavity," *IEEE Photon. Technol. Lett.*, vol. 33, pp. 211–213, 1997.

[31] Dossou, K., Botten, L. C., de Sterke, C., McPhedran, R. C., Astryan, M. A., Chen, S., and Brnovic, J., "Efficient couplers for photonic crystal waveguides," *Opt. Comm.*, vol. 265, p. 207, 2006.

[32] Fan, S. and Joannopoulos, J. D., "Analysis of guided resonances in photonic crystal slabs," *Phys. Rev. B.*, vol. 65, pp. 235112/1–235112/8, 2002.

[33] Fan, S., Yanik, M. F., Wang, Z., Sandhu, S., and Povinelli, M. L., "Advances in theory of photonic crystals," *J. of Lightwave Tech.*, vol. 24, pp. 4493–4501, 2006.

[34] Felici, T. and Engl, H., "On shape optimization of optical waveguides using inverse problem techniques," *Inverse problems*, vol. 17, p. 1141, 2006.

[35] Ferrini, R., Leuenberger, D., Houdr, R., Benisty, H., Kamp, M., and Forchel, A., "Disorder induced losses in planar photonic crystals," *Opt. lett.*, vol. 31, p. 1426, 2006.

[36] Fokkema, D. R. and G. L. G. Sleijpen, H. A. v. d. V., "Jacobi-davidson style qr and qz algorithms for the reduction of matrix pencils," *SIAM J. Sci. Comp.*, vol. 20, pp. 94–125, 1998.

[37] Fujii, T., David, A., Gao, Y., Iza, M., DenBaars, S. P., Hu, E. L., and Weisbuch, C., "Cone-shaped surface gan-based light-emitting diodes," *phys. stat. sol.*, vol. 2, pp. 2636–2840, 2005.

[38] Furukawa, A., Hoshi, M., Sasaki, S., Matsuzono, A., Moritoh, K., and Baba, T., "High-power single-transverse-mode holey vcsels," *Proc. of SPIE.*, vol. 5722, no. 7, pp. 183–190, 2005.

[39] Furukawa, A., Sasaki, S., Hoshi, M., Matsuzono, A., Moritoh, K., and Baba, T., "High-power single-mode vertical-cavity surface-emitting lasers with triangular holey structure," *Appl. Phys. Lett.*, vol. 85, pp. 5161–5163, 2004.

[40] Gaylord, T. K. and Moharam, M. G., "Analysis and applications of optical diffraction by gratings," *Proc. of IEEE*, vol. 73, pp. 894–937, 1985.

[41] Geels, R. S., Corzine, S. W., and Coldren, L. A., "Ingaas vertical-cavity surface-emitting lasers," *IEEE J. of Quant. Electron.*, vol. 27, pp. 1359–1367, 1991.

[42] Gerace, D. and Andreani, L. C., "Disorder-induced losses in photonic crystal waveguides with line defects," *Opt. lett.*, vol. 29, p. 1987, 2004.

[43] Gershen, H., Karle, T. J., Engelen, R. J. P., Bogaerts, W., Korterik, J. P., van Hulst, N. F., Krauss, T. F., and Kuipers, L., "Real-space observation of ultraslow light in photonic crystal waveguides," *Phys. Rev. Lett.*, vol. 94, pp. 073903/1–073903/4, 2005.

[44] Guo, S. and Albin, S., "Simple plane wave implementation for photonic crystal calculations," *Opt. Express.*, vol. 11, pp. 167–175, 2003.

[45] Hakansson, A., Sanchez-Dehesa, J., and Sanchis, L., "Inverse design of photonic crystal devices," *IEEE J. on sel. areas in Comm.*, vol. 23, p. 1365, 2005.

[46] Happ, T., Kamp, M., and Forchel, A., "Photonic crystal taperes for ultra-compact mode conversion," *Opt. lett.*, vol. 26, p. 1102, 2001.

[47] Helfert, S. F. and Pregla, R., "Efficient analysis of periodic structures," *J. Lightwave Technol.*, vol. 16, pp. 1694–1702, 1998.

[48] Ho, K. M., Chan, C. T., and Soukoulis, C. M., "Existence of a photonic gap in periodic dielectric structures," *Phys. Rev. Lett.*, vol. 65, pp. 3152–3155, 1990.

[49] Hughes, S., Ramunno, L., Young, J. F., and Sipe, J. E., "Extrinsic optical scattering loss in photonic crystal waveguides: Role of fabrication disorder and photon group velocity," *Phys. Rev. lett.*, vol. 26, p. 1102, 2005.

[50] Hugonin, J. P. and Lalanne, P., "Perfectly matched layers as nonlinear coordinate transforms: a generalized formalization," *J. Opt. Soc. Am. A*, vol. 22, pp. 1844–1849, 2005.

[51] Iga, K., Koyama, F., and Kinoshita, S., "Surface emitting semiconductor laser," *IEEE J. Quant. Electron.*, vol. 24, pp. 1845–1855, 1988.

[52] Istrate, E., Green, A. A., and Sargent, E. H., "Behavior of light at photonic crystal interfaces," *Phys. Rev. B.*, vol. 71, pp. 195122/1–195122/7, 2005.

[53] Jacobsen, R. S., Lavrinenko, A. V., Frandsen, L. H., Peucheret, C., Zsigri, B., Moulin, G., Fage-Pedersen, J., and Borel, P. I., "Direct experimental and numerical determination of extremely high group indices in photonic crystal waveguides," *Opt. Express*, vol. 13, pp. 7861–7871, 2005.

[54] Jafarpour, A., Reinke, C. M., Adibi, A., Xu, Y., and Lee, R. K., "A new method for the calculation of the dispersion of nonperiodic photonic crystal waveguides," *IEEE J. of Quant. Electron.*, vol. 40, p. 1060, 2004.

[55] Jamid, H. A. and Al-Bader, S. J., "*tm*-pass polariser using metal-clad waveguide with high index buffer," *Electron. Lett.*, vol. 24, p. 229, 1987.

[56] Jewell, J. L., Harbison, J. P., Scherer, A., Lee, Y. H., and Florez, L. T., "Vertical-cavity surface-emitting lasers: design, growth, fabrication, characterization," *IEEE J. of Quant. Electron.*, vol. 27, pp. 1332–1345, 1991.

[57] Jin, J., *The Finite Element Method in Electromagnetics*. John Wiley and Sons, Inc., 2002.

[58] John, S., "Strong localization of photons in certain disordered dielectric superlattices," *Phys. Rev. Lett.*, vol. 58, pp. 2486–2489, 1987.

[59] Johnson, S. G., Bienstman, P., Skorobogatiy, M. A., Ibanescu, M., Lidorikis, E., and Joannopoulos, J. D., "Adiabatic theorem and continuous couple-mode theory for efficient taper transition," *Phys. Rev. E*, vol. 66, p. 066608, 2002.

[60] Johnson, S. G. and Joannopoulos, J. D., "Block-iterative frequency-domain methods for maxwell's equations in a planewave basis," *Opt. Express.*, vol. 8, pp. 173–190, 2001.

[61] Johnson, S. G., Povinelli, M. L., Soljačić, M., Karalis, A., Jacobs, S., and Joannopoulos, J. D., "Roughness losses and volume current methods in photonic crystal waveguide," *Appl. Phys. B.*, vol. 81, p. 283, 2006.

[62] Khoo, E. H., Liu, A. Q., and Wu, J. H., "Nonuniform photonic crystal taper for high-efficiency mode coupling," *Opt. Express.*, vol. 13, pp. 7748–7759, 2005.

[63] Khoo, E. H., Liu, A. Q., Wu, J. H., Li, J., and Pinjala, D., "Modified step-theory for investigating mode coupling mechanism in photonic crystal waveguide taper," *Opt. Express.*, vol. 14, pp. 6035–6054, 2006.

[64] Khurgin, J. B., "Optical buffers based on slow light in electromagnetically induced transparent media and coupled resonator structures: comparative analysis," *J. of Opt. Soc. of Amer. B*, vol. 22, pp. 1062–1074, 2005.

[65] Kim, Y., Joyce, H. J., Gao, Q., Tan, H. H., Jagadish, C., Paladugu, M., Zou, J., and Suvorova, A. A., "Influence of nanowire density on the shape and optical properties of ternary ingaas nanowires," *Nanoletters*, vol. 6, 2006.

[66] Klein, B., Register, L. F., Grupen, M., and Hess, K., "Numerical simulation of vertical cavity surface emitting lasers," *Opt. Express.*, vol. 2, pp. 163–168, 1998.

[67] Koenderink, A. F., Lagendijk, A., and Vos, W. L., "Optical extinction due to intrinsic structural variations of photonic crystals," *Phys. Rev. B*, vol. 72, p. 153102, 2005.

[68] Kosaka, H., Kawashima, T., Tomita, A., Notomi, M., Tamamura, T., Sato, T., and Kawakami, S., "Superprism phenomena in photonic crystals," *Phy. Rev. B.*, vol. 58, pp. R10096–R10099, 1998.

[69] Kotynski, R., Dems, M., and Panajotov, K., "Waveguiding losses of micro-structured fibres - plane wave method revisited," *Opt. Quant. Electron.*, vol. 39, pp. 469–479, 2007.

[70] Krishnamurthy, V. and Klein, B., "Round trip transfer matrix technique for multilayer photonic crystal crystal confined laser," *Optics in South East., Charlotte, NC.*, Sept. 6-8 2006.

[71] Krishnamurthy, V. and Klein, B., "Optical simulation of photonic crystal patterned layer lasers," *Photonics West., San Jose, CA.*, Jan 20-25 2007.

[72] Krishnamurthy, V. and Klein, B., "Theoretical investigation of metal cladding for nanowire and micropost lasers," *IEEE J. Quant. Elect.*, vol. 44, pp. 67–74, 2008.

[73] Krishnamurthy, V. and Klein, B., "Comprehensive theory of planewave expansion based eigenmode method for scattering matrix analysis of photonic structures," *J. of Opt. Soc. of Amer. B*, (submitted).

[74] Krishnamurthy, V., Messer, M., Allen, J., and Klein, B., "Matrix-free planewave modal expansion approach for robust design of photonic structures," *CLEO/QELS '08*, no. JThA95, 2008.

[75] Krishnamurthy, V., Messer, M., Wang, C., Allen, J. K., and Klein, B., "Robust design of non-linearly tapered slow light couplers," *J. of Opt. A*, (accepted).

[76] Kuang, W., Kim, C. S., Stapleton, A., and O'Brien, J., "Grating assisted coupling of optical fibers and photonic crystal waveguides," *Opt. lett.*, vol. 27, p. 1604, 2002.

[77] Lalanne, P., "Electromagnetic analysis of photonic crystal waveguides operating above the light cone," *IEEE J. Quantum Elec.*, vol. 38, pp. 800–804, 2002.

[78] Lalanne, P. and Morris, G. M., "Highly improved convergence of the coupled-wave method for tm polarization," *J. Opt. Soc. Am. A*, vol. 13, pp. 779–784, 1996.

[79] Lalanne, P. and Silberstein, E., "Fourier-modal methods applied to waveguide computational problems," *Opt. Letters.*, vol. 25, pp. 1092–1094, 2000.

[80] Lee, K.-H., Baek, J.-H., Hwang, I.-K., Lee, Y.-H., Lee, G.-H., Ser, J.-H., Kim, H.-D., and Shin, H.-E., "Square-lattice photonic-crystal vertical-cavity surface-emitting lasers," *Opt. Exp.*, vol. 12, pp. 4136–4143, 2004.

[81] Lehoucq, R. B., Sorenson, D. C., and Yang, C., *ARPACK Users' Guide: Solution of Large-Scale Eigenvalue Problems with Implicitly Restarted Arnoldi Methods*. Philadelphia: SIAM Publications, 1998.

[82] Leisher, P. O., Danner, A. J., and Choquette, K. D., "Single-mode 1.3-μm photonic crystal vertical-cavity surface-emitting laser," *IEEE Photon. Tech. Lett.*, vol. 18, pp. 2156–2158, 2006.

[83] Li, L., "Bremmer series, r-matrix propagation algorithm, and numerical modeling of diffraction gratings," *J. Opt. Soc. Am. A*, vol. 11, pp. 2829–2836, 1994.

[84] Li, L., "Use of fourier-series in the analysis of discontinuous periodic structures," *J. Opt. Soc. Am. A*, vol. 13, pp. 1870–1876, 1998.

[85] Luo, C., Johnson, S. G., and Joannopoulos, J. D., "All-angle negative refraction in a three-dimensionally periodic photonic crystal," *App. Phy. Lett.*, vol. 81, pp. 2352–2354, 2002.

[86] Luo, C., Johnson, S. G., Joannopoulos, J. D., and Pendry, J. B., "All-angle negative refraction without negative effective index," *Phy. Rev. B.*, vol. 65, pp. 201104/1–201104/4, 2002.

[87] Luyssaert, B., Bienstman, P., Vandersteegen, P., Dumon, P., and Baets, R., "Efficient nonadiabatic planar waveguide tapers," *J. of Lightwave Tech.*, vol. 23, p. 2462, 2005.

[88] Marhic, M. E. and Garmire, E., "Low order te_{0q} operation of a co_2 laser for transmission through circular metallic waveguides," *Appl. Phys. Lett.*, vol. 38, no. 10, 1981.

[89] Martinsson, H., Vukusic, J. A., Grabherr, M., Michalzik, R., Jager, R., Ebeling, K. J., and Larsson, A., "Transverse mode selection in large-area oxide-confined vertical-cavity surface-emitting lasers using a shallow surface relief," *IEEE Photon. Technol. Lett.*, vol. 11, pp. 1536–1538, 1999.

[90] Maslov, A. V. and Ning, C. Z., "Modal gain in a semiconductor nanowire laser with anisotropic bandstructure," *IEEE J. Quant. Elect.*, vol. 40, no. 10, 2004.

[91] Maslov, A. V. and Ning, C. Z., "Size reduction of a semiconductor nanowire laser," *Proc. of SPIE.*, vol. 6468, pp. 6480I/1–6480I/7, 2007.

[92] Mekis, A. and Joannopoulos, J. D., "Tapered couplers for efficient interfacing between dielectric and photonic crystal waveguides," *J. of Lightwave Tech.*, vol. 19, p. 861, 2001.

[93] Messer, M., Panchal, J. H., Allen, J. K., Krishnamurthy, V., Klein, B., and Mistree, F., "Designing embodiment design-processes using a value-of-information-based approach with applications for integrated product and materials design such as photonic crystal waveguides," *ASME Design Automation Conf.*, vol. DETC2008/DAC-49395, 2008.

[94] Milton, A. F. and Burns, W. K., "Mode coupling in optical waveguide horns," *IEEE J. of Quant. Electron.*, vol. 13, p. 828, 1977.

[95] Miyagi, M. and Kawakami, S., "Design theory of dielectric-coated circular metallic waveguides for infrared transmission," *J. Light. Tech.*, vol. 2, p. 116, 1984.

[96] Mori, D. and Baba, T., "Dispersion-controlled optical group delay device by chirped photonic crystal waveguides," *Appl. Phys. Lett.*, vol. 85, no. 7, pp. 1101–1103, 2004.

[97] Morito, K., Mori, D., Mizuta, E., and Baba, T., "Full 3d fdtd analysis of modal characteristics in vcsels with holey structure," *Proc. of SPIE.*, vol. 5722, no. 7, pp. 191–200, 2005.

[98] Nezhad, M. P., Tetz, K., and Fainman, Y., "Gain assisted propagation of surface plasmons polaritons on planar metallic waveguides," *Opt. lett.*, vol. 12, p. 4072, 2004.

[99] Nicoleta, A., Guenneaub, S., Geuzainec, C., and Zollaa, F., "Modelling of electromagnetic waves in periodic media with finite elements," *J. of Comp. and Appl. Math.*, vol. 168, pp. 321–329, 2004.

[100] Noborosika, J., Motohisa, J., Takeda, J., Inari, M., Miyoshi, Y., Ooike, N., and Fukui, T., "Growth of gaas and ingaas nanowires by utilizing selective area movpe," *Int. Conf. on Ind. Phosp. and rel. matls.*, pp. 647–650, May-June 2004.

[101] Noda, S., Chutinan, A., and Imada, M., "Trapping and emission of photons by a single defect in a photonic bandgap structure," *Appl. Phys. Lett.*, vol. 407, pp. 608–610, 2000.

[102] Notomi, M., Shinya, A., Mitsugi, S., Kuramochi, E., and Ryu, H.-Y., "Waveguides, resonators and their coupled elements in photonic crystal slabs," *Opt. Exp.*, vol. 12, p. 1551, 2004.

[103] Nyakas, P., "Full-vectorial three-dimensional finite element optical simulation of vertical-cavity surface-emitting lasers," *IEEE J. of Lightwave Tech.*, vol. 25, pp. 2427–2434, 2007.

[104] Nyakas, P., Varga, G., Pusks, Z., Hashizume, N., Krpti, T., Veszprmi, T., and Zsombok, G., "Self-consistent real three-dimensional simulation of vertical-cavity surface-emitting lasers," *J. Opt. Soc. Am. B*, vol. 23, pp. 1761–1769, 2006.

[105] O'Faolin, L., White, T. P., O'Brien, D., Yuan, X., Settle, M. D., and Krauss, T. F., "Dependence of extrinsic loss on group velocity in photonic crystal waveguides," *Opt. exp.*, vol. 15, p. 13129, 2007.

[106] Oliner, A. A., Peng, S.-T., Hsu, T.-I., and Sanchez, A., "Guidance and leakage properties of a class of open dielectric waveguides: Part ii - new physical effects," *IEEE Trans. Microwave Theory Tech.*, vol. 29, pp. 855–869, 1981.

[107] Omar, A. S. and Schunenmann, K. F., "Complex and backward-wave modes in in-homogeneously and anisotropically filled waveguides," *IEEE Trans. Microwave Theory Tech.*, vol. 35, pp. 268–275, 1987.

[108] Ordal, M. A., Long, L. L., Bell, R. J., Bell, S. E., Bell, R. R., Jr., R. W. A., and Ward, C. A., "Optical properties of metals al, co, cu, au, fe, pb, ni, pd, pt, ag, ti and w in infrared and far infrared," *Appl. Opt.*, vol. 22, no. 7, 1983.

[109] Palamaru, M. and Lalanne, P., "Photonic crystal waveguides: Out-of-plane losses and adiabatic modal conversion," *Appl. Phy. Lett.*, vol. 78, pp. 1466–1468, 2001.

[110] Paschotta, R., Spühler, G. J., Sutter, D. H., Matuschek, N., Keller, U., Moser, M., Hövel, R., Scheuer, V., Angelow, G., and Tschudi, T., "Double-chirped semiconductor mirror for dispersion compensation in femtosecond lasers," *Appl. Phys. Lett.*, vol. 75, pp. 2166–2168, 1999.

[111] Pearce, G. J., Hedley, T. D., and Bird, D. M., "Adaptive curvilinear coordinates in a plane-wave solution of maxwell's equations in photonic crystals," *Phys. Rev. B.*, vol. 71, p. 195108, 2005.

[112] Pelton, M., Vučković, J., Solomon, G., Santori, C., Zhang, B., Plant, J., and Yamamoto, Y., "An efficient source photons: single quantum dot in a micropost microcavity," *Physica E.*, vol. 17, pp. 564–567, 2003.

[113] Peng, S. and Oliner, A., "Guidance and leakage properties of a class of open dielectric waveguides: Part i - mathematical formulations," *IEEE Trans. Microwave Theory Tech.*, vol. 29, pp. 843–855, 1981.

[114] Piprek, J., *Nitride semiconductor devices: principles and simulation.* Weinheim: Weinheim: WILEY-VCH Verlag GmbH & Co. KGaA, 2007.

[115] Pottage, J. M., Bird, D. M., Hedley, T. D., Birks, T. A., Knight, J. C., Russel, P. S. J., and Roberts, P. J., "Robust photonic band gaps for hollow core guidance in pcf made from high index glass," *Opt. Express*, vol. 11, pp. 2854–2861, 2003.

[116] Pottier, P., Ntakis, I., and La, R. D., "Photonic crystal continuous taper for low-loss direct coupling into 2d photonic crystal channel waveguides and further device functionality," *Opt. Commn.*, vol. 223, p. 339, 2003.

[117] Povinelli, M. L., Johnson, S. G., and Joannopoulos, J. D., "Slow-light, band-edge waveguides for tunable time delays," *Opt. Exp.*, vol. 13, pp. 7145–7159, 2005.

[118] Prather, D., Murakowski, J., Shi, S., Venkataraman, S., Sharkawy, A., Chen, C. H., and Pustai, D., "High-efficiency coupling structure for a single-line-defect photonic-crystal waveguide," *Opt. Lett.*, vol. 27, p. 1601, 2002.

[119] Rigneault, H., Lemarchand, F., Sentenac, A., and Giovannini, H., "Extraction of light from source located inside waveguide grating structures," *Opt. Lett.*, vol. 24, pp. 148–150, 1999.

[120] Sambles, J. R., Bradbery, G. W., and Yang, F., "Optical excitation of surface plasmons: An introduction," *Contem. Phy.*, vol. 32, no. 3, pp. 173–183, 1991.

[121] Seepersad, C. C., "A robust topological preliminary design exploration method with materials design applications," tech. rep., G. W. W School of Mech. Engg., Georgia Inst. of Tech., Atlanta, GA, 2004.

[122] Seepersad, C. C., Dempsey, B. M., Allen, J. K., Mistree, F., and McDowell, D. L., "Design of multifunctional honeycomb materials," *Am. Ins. Aero. and Astro. journ.*, vol. 42, pp. 1025–1033, 2004.

[123] Seepersad, C. C., Mistree, F., and Allen, J. K., "Designing evelving families of products using utility-based compromise decision support problem," *Int. journ. of Mass. Custom.*, vol. 1, pp. 37–64, 2005.

[124] Seidel, J., Grafström, S., and Eng, L., "Stimulated emission of surface plasmons at the interface between a silver film and an optically pumped dye solution," *Phys. Rev. Lett.*, vol. 94, pp. 117401/1–117401/4, 2005.

[125] Shi, S., Chen, C., and Prather, D. W., "Plane-wave expansion method for calculating band structure of photonic crystal slabs with perfectly matched layers," *J. Opt. Soc. Am. A*, vol. 21, pp. 1769–1775, 2004.

[126] Silberstein, E., Lalanne, P., Hugonin, J.-P., and Cao, Q., "Use of grating theories in integrated optics," *J. of Opt. Soc. Amer. A*, vol. 18, p. 2865, 2001.

[127] Sleijpen, G. L. G. and van der Vorst, H. A., "A jacobi-davidson iteration method for linear eigenvalue problems," *SIAM J. Matrix Anal. Appl. (SIMAX)*, vol. 17, pp. 401–425, 1996.

[128] Smith, D. R., Dalichaouch, R., Kroll, N., Schultz, S., McCall, S. L., and Platzman, P. M., "Photonic band structure and defects in one and two dimensions," *J. Opt. Soc. Am. B*, vol. 10, pp. 314–321, 1993.

[129] Snyder, A. W., "Coupling of modes on a tapered dielectric cylinder," *IEEE Trans. on Micro. Theory and Tech*, vol. 18, p. 383, 1970.

[130] Soda, H., Iga, K., Kitahara, C., and Suematsu, Y., "Gainasp/inp surface emitting injection lasers," *Jpn. J. Appl. Phys.*, vol. 18, pp. 2329–2330, 1979.

[131] Spuehler, M. M., Offrein, B. J., Bona, G. L., Germann, R., Masserek, I., and Erni, D., "A very short planar silica spot-size converter using a nonperiodic segmented waveguide," *IEEE J. of Lightwave Tech.*, vol. 16, p. 1680, 1998.

[132] Srinivasan, K. and Painter, O., "Momentum space design of high-q photonic crystal optical cavities," *Opt. Express*, vol. 10, pp. 670–684, 2002.

[133] Srinivasan, K. and Painter, O., "Fourier space design of high-q cavities in standard and compressed hexagonal lattice photonic crystals," *Opt. Express.*, vol. 11, pp. 579–593, 2003.

[134] Sudbo, A. S., "Film mode matching: a versatile numerical method for vector mode field calculations in dielectric waveguides," *Pure Appl. Opt.*, vol. 2, pp. 211–233, 1993.

[135] Talneau, A., Lalanne, P., Agio, M., and Soukoulis, C., "Low-reflection photonic crystal taper for efficient coupling between guided sections of arbitrary widths," *Opt. lett.*, vol. 27, p. 1522, 2002.

[136] Thorhauge, M., Frandsen, L. H., and Borel, P. I., "Efficient photonic crystal directional couplers," *Opt. lett.*, vol. 28, p. 1525, 2003.

[137] Tikhodeev, S. G., Yablonskii, A. L., Muljarov, E. A., Gippius, N. A., and Ishihara, T., "Quasiguided modes and optical properties of photonic crystal slabs," *Phys. Rev. B.*, vol. 66, p. 045102, 2002.

[138] Tredicucci, A., Gmachl, C., Capasso, F., Hutchinson, A. L., Sivco, D. L., and Cho, A. Y., "Single-mode surface-plasmon laser," *Appl. Phys. Lett.*, vol. 76, pp. 2164–2166, 2000.

[139] Visser, T. D., Blok, H., Demeulenaere, B., and Lenstra, D., "Confinement factors and gain in optical amplifiers," *IEEE J. Quant. Elect.*, vol. 33, no. 10, pp. 1763–1766, 1997.

[140] Vlasov, Y. A., Bo, X.-Z., Sturm, J. C., and Norris, D., "On-chip natural assembly of silicon photonic bandgap crystals," *Nature*, vol. 414, pp. 289–293, 2001.

[141] Wei, C., Groen, F., Smmit, M., Moerman, I., VanDaele, P., and Baets, R., "Integrated optical elliptic couplers: modeling, design, and applications," *IEEE J. of Lightwave Tech.*, vol. 15, p. 906, 1997.

[142] White, T. P., Kuhlmey, B. T., McPhedran, R. C., Maystre, D., Renversez, G., de Sterke, C. M., and Botten, L. C., "Multipole method for microstructured optical fibers. i. formulation," *J. Opt. Soc. Am. B*, vol. 19, pp. 2322–2330, 2002.

[143] Whittaker, D. M. and Culshaw, I. S., "Scattering-matrix treatment of patterned multilayer photonic structures," *Phys. Rev. B.*, vol. 60, pp. 2610–2618, 1999.

[144] Winter, G., Wedge, S., and Barnes, W. L., "Can lasing at visible wavelengths be achieved using low-loss long-range surface plasmon-polariton mode?," *New J. of Phys.*, vol. 8, pp. 1–14, 2006.

[145] Xing, A., Davanco, M., Blumenthal, D. J., and Hu, E. L., "Fabrication of inp-based two-dimensional photonic crystal membrane," *J. Vac. Sci. Technol. B*, vol. 22, p. 70, 2004.

[146] Xu, Y., Lee, R. K., and Yariv, A., "Adiabatic coupling between conventional dielectric waveguides and waveguides with discrete translational symmetry," *Opt. lett.*, vol. 25, p. 755, 2000.

[147] Yablonovitch, E., "Inhibited spontaneous emission in solid-state physics and electronics," *Phys. Rev. Lett.*, vol. 58, pp. 2059–2062, 1987.

[148] Yablonovitch, E. and Gmitter, T. J., "Photonic band structure: The face-centered-cubic case," *Phys. Rev. Lett.*, vol. 63, pp. 1950–1953, 1989.

[149] Yablonovitch, E. and Gmitter, T. J., "Donor and acceptor modes in photonic band structures," *Phys. Rev. Lett.*, vol. 67, pp. 3380–3383, 1991.

[150] Yokouchi, N., Danner, A. J., and Choquette, K. D., "Two-dimensional photonic crystal confined vertical-cavity surface-emitting lasers," *IEEE Sel. J. of Quant. Electron.*, vol. 9, pp. 1439–1445, 2003.

[151] Yu, C. and Chang, H., "Modal analysis of photonic crystal planar waveguides using a finite difference method," *CLEO - The 5th Pacific Rim Conference*, vol. 1, p. 349, 2003.

[152] Zaki, K. A., Chen, S., and Chen, C., "Modeling discontinuities in dielectric loaded waveguides," *IEEE Trans. MTT.*, vol. 36, no. 12, pp. 1804–1810, 1988.

[153] Zhang, B., "Horn waveguide couplers for interfacing between two-dimensional photonic crystal and single mode planar dielectric waveguides," *Acta Physica Sinica*, vol. 55, 2006.

[154] Zhou, D. and Mawst, L. J., "Simplified-antiresonant reflecting optical waveguide-type vertical-cavity surface-emitting lasers," *Appl. Phys. Lett.*, vol. 76, pp. 1659–1661, 2000.

VITA

Vivek Krishnamurthy received the Bachelor of Engineering (B.E) degree in Electronics and communications from Sri Jayachamarajendra College of Engineering, Mysore (Visvesvariah Technological University, India) in 2002, the Master of Science in Electrical Engineering (M.S.E.E) degree from the University of Texas at Arlington in 2004 and is currently working towards the Ph.D. in Electrical Engineering at the Georgia Institute of Technology Savannah campus. His advisor is Dr. Benjamin Klein.

He was advised by Dr. Kambiz Alavi for his Masters degree Thesis. The topic of his thesis was to design electroreflection modulator with high ON/OFF contrast ratio uisng asymmetric Fabry-Perot mirrors. His work also focused on the optical design of resonant cavity enhanced photodetector. For his Ph.D dissertation, he is developing various numerical methods for analyzing novel surface plasmon and photonic crystal-based structures.

His research interests include theoretical investigation of the dispersion and confinement properties of active photonic crystal and surface plasmon-based devices. He is also interested in theoretical investigation of exciton and chirping effects in electroabsorption modulators.

He has taken a variety of Optics courses for his major and Math courses for his minor. He has attended and published in various conferences, including CLEO/QELS 2008 in San Jose, CA, Photonics West 2007 in San Jose, CA, Optics in South East 2006 in Charlotte, NC. He is a student member of IEEE and OSA.

In January 2009, he will be starting his new responsibilities as a senior research fellow in the Nanophotonics and Nano-scale integration group at the Data Storage Institute, Singapore.